REACTION OF COPPER MATTE DROPLETS WITH AN OXIDIZING SLAG

REACTION OF COPPER MATTE DROPLETS WITH AN OXIDIZING SLAG

By

RASOOL TAHMASEBI, B.Sc., M.Sc.

A Thesis Submitted to the School of Graduate Studies in Partial Fulfilment of the Requirements for the Degree Master of Applied Science

McMaster University

MASTER OF APPLIED SCIENCE (2013) McMaster University

(Materials Science and Engineering) Hamilton, Ontario

TITLE: Reaction of Copper Matte Droplets with an Oxidizing Slag

AUTHOR: Rasool Tahmasebi, B.Sc., M.Sc. (Isfahan University of Technology)

SUPERVISOR: Professor Kenneth S. Coley

NUMBER OF PAGES: xviii, 179

Abstract

Reaction kinetics of copper sulphide matte (Cu_2S) with an oxidizing slag was investigated. Silica-saturated fayalite ($2FeO.SiO_2$) slag was synthesized by melting powder mixtures of iron, silica and hematite with respective ratios of 1:2:3.6 at high temperatures. Experiments were performed in an inert atmosphere using a high-temperature furnace equipped with X-ray fluoroscopy and pressure transducer. The effect of temperature (1400 – 1475 °C) and matte droplet size (0.5 – 2 g) on desulphurization rate was evaluated. Chemical titration was performed on quenched slag samples synthesized at different temperatures in order to determine the amounts of Fe^{2+} and Fe^{3+} in the slags. Slag/matte samples quenched from high temperatures were extensively analyzed by means of optical microscope as well as scanning electron microscope (SEM), the latter equipped with an energy dispersive X-ray spectrometer (EDS). EDS analysis of the quenched samples showed that some areas of pure Cu were formed inside the matte droplets. It indicated that desulphurization reaction indeed has taken place and copper was formed as the product. In addition, EDS showed that some Fe-rich areas were formed inside the matte droplets. Gas halo formation around the droplets was confirmed by X-ray fluoroscopy observations. Additionally, it was seen that dome-like bubbles formed during high-temperature experiments on top of the matte droplets with mass equal to 0.75-gram or larger. In contrast to Fe-C metal droplets in contact with oxidizing slags, no droplet swelling was detected in this study. Reaction kinetics investigations showed that initial desulphurization rate increased with increasing temperature and matte droplet size. In fact, it was shown that rate increased linearly with matte droplet surface area. Finally,

mass transfer in the slag phase and mass transfer in the gas halo formed around the droplet were found to be the rate-controlling mechanisms prior to and after gas halo formation, respectively.

Acknowledgements

I would like to extend my sincere gratitude and appreciation to my dear supervisor, Professor Ken Coley, for his continuous guidance and support throughout this research. I learned so much from him and I am thankful.

I wish to thank my examiners, Professors Joseph McDermid and Tony Petric for taking the time to read my thesis and for their thoughtful comments.

I would like to thank my fellow graduate students in Dr. Coley's group, particularly Michael Pomeroy for training me on the experimental apparatus.

I wish to thank all the faculty and staff in Materials Science and Engineering Department at McMaster University who helped me and supported me throughout these years. In particular, I would like to thank Doug Culley, Ed McCaffery and Owen Kelly for their invaluable technical assistance and training. I would also like to thank Chris Butcher at CCEM for his assistance in performing EDS analysis.

My sincere thanks to all my wonderful friends at McMaster University and in Hamilton for their true friendship and support.

Lastly, but most importantly, I would like to thank my family for their continued love and support throughout my life and particularly for their encouragement and support in pursuing graduate studies. I especially thank my dear sister, Taiebeh, for being my inspiration and for her never-ending support and encouragement. I certainly could not have accomplished this, without my family's support and patience.

Thank you!

Table of contents

List of figures

List of tables

List of abbreviations and symbols

a_i the activity of the species i with reference to a specified standard state

A droplet surface area or droplet-slag interfacial area in cm^2

D_{SO-SO_2} the intermolecular diffusion coefficient for SO-SO_2 gas mixture (cm^2/s)

Fe_B^{3+} Fe^{3+} concentration in the bulk of the slag (wt%)

Fe_i^{3+} Fe^{3+} concentration at the interface (wt%)

J_i the flux of i (moles/s)

k_s mass transport constant in the slag phase (cm/s)

K the equilibrium constant

MW_i molecular weight of species i (g/mole)

N_i the mole fraction of the species i

P pressure in atm

P_i the partial pressure of the gaseous species i in atm

$P_{SO_2}^{s/g}$ equilibrium partial pressure of SO_2 at the slag/gas interface

$P_{SO_2}^{m/g}$ equilibrium partial pressure of SO_2 at the matte/gas interface

Q activation energy (J/mole)

R the gas constant (J/mole.K)

R gas evolution rate (moles/s)

T temperature

X_i the mole fraction of the species i

$\Delta G°$ the standard Gibbs free energy change (joules)

γ_i the activity coefficient of the species i

δ the thickness of the gaseous layer (cm)

ρ density in g/cm^3

[i] the concentration of species i in melt (weight %)

(i) the concentration of species i in slag (weight %)

i species i dissolved

(g) gas

(l) liquid

Declaration of academic achievement

The present study seeks to expand the body of knowledge regarding the overall desulphurization reaction in copper pyrometallurgical extraction. The focus of this research is on the desulphurization reaction of matte droplets with fayalite slag and the interaction between matte droplet and slag at high temperatures. Experiments carried out by the author at different temperatures and using different droplet sizes generated kinetic data, which were used to propose a kinetic model. The present study should help advance the understanding of the overall desulphurization reaction in matte converting.

Chapter 1. Introduction

Since copper occurs naturally as native copper, it has been known to early man as far ago as 9000 B.C [1]. Copper and bronze production dates back to 4500 B.C., when man learned to conduct smelting on copper and tin ores in a charcoal fire. Over the past few millennia, copper and its alloys have been playing an important role in human's life. Nowadays, from wire, cable and electronic devices, to construction, industrial machinery and heat exchangers, high-purity copper is widely being used mainly due to its high electrical and thermal conductivity [2]. Copper alloys such as brass and bronze are also being used for a wide variety of applications. Total copper production in 2010 was reported to be about 20 million tonnes, most of which is achieved by smelting copper sulfide concentrates [3-5].

Copper is commonly present in the earth's crust as rocks of sulphide minerals containing iron and copper. Therefore, special metallurgical techniques are applied in order to extract copper from the ore. Since more than 90% [6,7] of copper originates from sulphide minerals, copper is mainly produced through pyrometallurgical techniques.

Pyrometallurgy of copper consists of two main stages: smelting and converting (as shown in Figure 1.1). In these operations, copper concentrate is subjected to blowing at high-temperature and flux (e.g. silica and lime) is added to the furnace. In smelting stage, sulfur is removed as SO_2 and iron oxide (FeO) is formed as a result of oxidation, which is slagged with silica and is then removed from the furnace. In converting stage, remaining iron sulphide is removed and oxidation of copper sulphide takes place. Blister copper

with approximate purity of 99% Cu is produced in converting furnace. It will then be subjected to electrorefining in order to produce highly pure Cu.

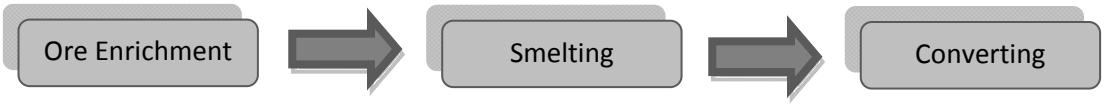

Figure 1.1 – Flowchart of different stages of pyrometallurgical extraction of copper.

In smelting and converting stages similar to oxygen steelmaking, a significant number of droplets form and enter the slag phase as a result of stirring caused by blowing oxygen/air to the molten metal/matte phase. However, in these operations, instead of CO, SO_2 gas is generated as a result of the desulphurization reactions taking place.

Generation of a huge number of matte droplets as well as the strongly oxidizing conditions in converter furnace, leads to copper and copper matte droplets being entrained in the slag phase. It is estimated that 4-8% copper is lost in the slag phase [3] either by entrainment or dissolved copper/copper matte in the slag. This loss has been reported to amount to more than 400 million dollars annually [4,5].

A voluminous literature is available on the topic of molten matte reaction with an oxygen/air jet [6-15]. However, reaction of matte droplets with an oxidizing slag and the phenomena involved has not been paid due attention to. Although there are papers in the literature discussing the matte-slag interaction in copper-making, however the research performed on this topic has been mostly limited to interfacial and surface tension studies [16-22].

Better knowledge and understanding of the matte droplet/slag interactions and the mechanisms involved in matte smelting and converting will help to improve the process, both financially and environmentally. Therefore, more research on this topic is needed.

By investigating the matte droplet behaviour in the slag phase in smelting and converting processes and by studying the effect of different parameters on the desulphurization reaction, it would be possible to propose the reaction mechanisms and eventually find effective ways to enhance the process.

Similar to steelmaking, in smelting also parameters such as chemical composition of the slag, chemical composition of the metal/matte droplet, temperature as well as metal/matte droplet size all seem to have an effect on the rate of the desulphurization reaction.

Another motivation for launching this study was to investigate whether droplet swelling would happen. In studies of the decarburization reaction of Fe-C metal droplets with FeO-bearing slags, droplet swelling has been reported when a droplet with low carbon content was exposed to a slag with high oxidizing capacity. In addition, some researchers have reported gas halo formation around the metal droplet in cases when a molten droplet with high carbon content (higher than 3 wt%) was decarburized by using a slag with lower oxygen potential. So, it was interesting to evaluate whether gas halo formation or droplet swelling would occur if a Cu_2S matte droplet was placed in contact with an oxidizing slag.

In this study, reaction of copper matte droplets with an oxidizing slag is investigated. Synthetic silica-saturated fayalite (Fe_2SiO_4), with similar chemical composition of slags in the industry, was employed. The effect of temperature as well as matte droplet size on

the desulphurization reaction was evaluated. In addition, the potential rate-controlling mechanisms were studied. Furthermore, using X-ray fluoroscopy technique, slag/matte droplet interactions at high temperatures were thoroughly analyzed.

This thesis consists of 5 chapters. In Chapter 1, the background and the motivation for this study is discussed. In Chapter 2, a brief literature review of the previous relevant studies is presented. Chapter 3 presents the materials and experimental procedure. Chapter 4 is dedicated to experimental results and discussion. In Chapter 5, a summary of conclusions is provided.

Chapter 2. Literature review

2.1. Fundamentals of copper pyrometallurgical extraction

Copper is available in the earth's crust, usually as minerals of copper-iron sulphides or copper sulphide, such as chalcopyrite ($CuFeS_2$), bornite (Cu_5FeS_4) and chalcocite (Cu_2S) [3,23]. In nature, copper sulphide minerals are generally associated with pyrite (FeS_2) [23]. Copper content of ores is typically very low, varied between 0.5 to 2%. Therefore, different processing techniques are applied in order to increase the copper content of the concentrate.

In smelting and converting operations, copper matte (i.e. mixed molten sulphides) is oxidized at high temperatures of about 1250 °C. This is achieved by injecting industrial oxygen or oxygen-enriched air to the furnace. During these two operations, iron, sulfur and the gangue materials are removed and eventually crude copper metal (blister copper, 99% Cu) is produced, which is later taken to fire refining and electrolytic refining for further processing and to eventually produce ultra pure copper.

In Figure 2.1, a typical flow sheet of the production of a low grade copper sulphide ore is presented.

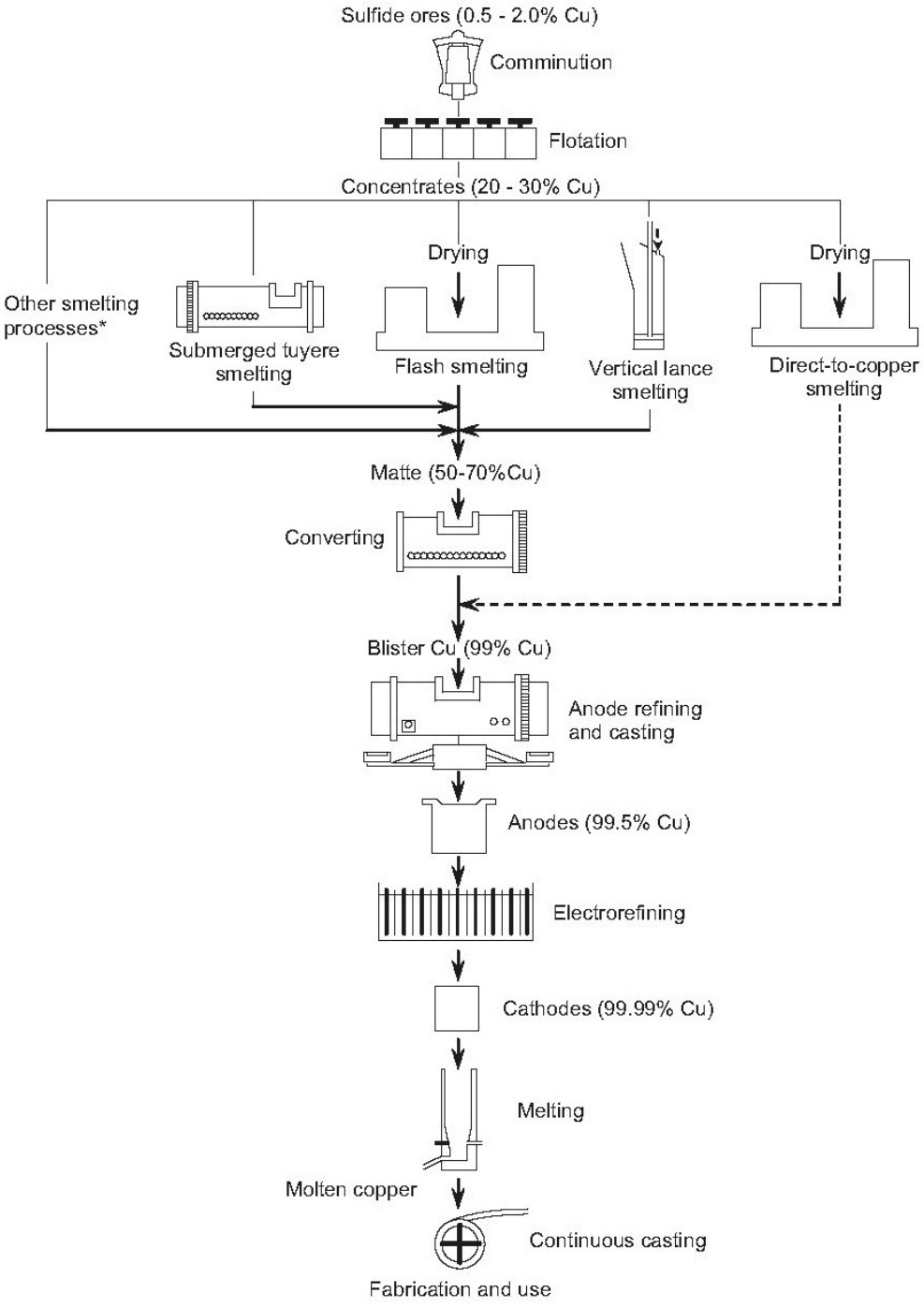

Figure 2.1 – Typical flow sheet for the production of a low grade copper sulphide ore [3].

Some of the reactions that may take place (depending on the type of the process) during smelting and converting operations include [3,23]:

$$2CuFeS_2 + \frac{6.5}{2} O_2 = Cu_2S + \frac{1}{2} FeS + \frac{3}{2} FeO + \frac{5}{2} SO_2 \quad (2.1)$$

$$CuFeS_2 + \frac{5}{2} O_2 = Cu + FeO + 2SO_2 \quad (2.2)$$

$$FeS_2 + \frac{5}{2} O_2 = FeO + 2SO_2 \quad (2.3)$$

$$2FeO + SO_2 = Fe_2SiO_4 \quad (2.4)$$

$$Cu_2S + O_2 = 2Cu + SO_2 \quad (2.5)$$

$$Cu_2S + \frac{3}{2} O_2 = Cu_2O + SO_2 \quad (2.6)$$

$$2Cu_2O + Cu_2S = 6Cu + SO_2 \quad (2.7)$$

As iron has a higher affinity to oxygen, it is removed in highly oxidizing conditions of pyrometallurgical extraction of copper. In fact, it is said that copper sulphide is not oxidized and copper-making is not occurred until Fe content of the matte is less than about 1% [3,23]. Therefore by introducing oxygen/air mixtures to iron-copper-sulphide matte at high temperatures, iron sulphide is oxidized and iron oxide (FeO) and SO_2 is produced. During converting, it has been argued that "significant oxidation of copper does not occur until the sulfur content of the copper falls below about 0.02%." [3]

Iron oxide produced during copper smelting and converting is slagged with silica (SiO_2), forming fayalite (Fe_2SiO_4). Silica is usually present in the ore but is also added to the

furnace as flux. Therefore, addition of silica as flux is essential for slag formation with iron oxide and as well as to maintain a good immiscibility between melt and slag. In fact, it has been reported that the best separation occurs when a silica-saturated slag is produced.

Immiscibility between slag and molten matte is significantly important in order to have an efficient process and to decrease loss of copper to the slag phase. Therefore, in some plants lime (CaO) or limestone is also added in order to decrease the melting point of the slag and increase its fluidity, which in turn leads to better phase separation [3].

Matte smelting is predominantly conducted worldwide in flash furnaces (e.g. Outokumpu, Inco, Outotec). It is also preformed in submerged tuyere furnaces (e.g. Noranda, El Teniente, and Vanyukov).

Copper matte converting is mostly conducted in the famous Peirce-Smith converter, which blows oxygen-enriched air into molten matte through submerged tuyeres.

Recently direct-to-copper smelting processes have been introduced in three plants in Australia, Poland and Zambia [3]. These processes combine smelting and converting stages and molten copper is directly produced from copper concentrate in only one flash furnace. Although these process have many advantages namely limiting SO_2 evolution to only one furnace, but their major disadvantage is that Cu losses in slag is high and therefore their employment is now only limited to low-Fe concentrates [3].

The application of continuous smelting/converting processes such as Mitsubishi, Outokumpu, Noranda and Isasmelt is still very advantageous even compared to producing molten copper from only one furnace. These continuous processes have energy, SO_2

collection, and cost advantages [3] and therefore are being increasingly employed for copper pyrometallurgical production worldwide.

2.2. Thermodynamic studies

Detail knowledge of phase equilibria and thermodynamics of any system under study is essential prior to performing any kinetic investigations, as it will enable us to determine feasibility or spontaneity of a chemical reaction or transformation and also to understand the conditions at which a reaction will take place.

In this section, thermodynamics of Cu-S-O system as well as iron-silicate slags, both of which are relevant to copper pyrometallurgical extraction, will be discussed.

2.2.1. Thermodynamics of Cu-S and Cu-S-O systems

Extensive knowledge of chemical behaviour and thermodynamic properties of the systems Cu-S and Cu-S-O is essential for better understanding and optimization of copper pyrometallurgical extraction. Consequently, numerous researchers have conducted studies on phase equilibria and thermochemical properties of these systems [4,5,24-41].

Chakrabarti et al. [25] comprehensively studied Cu-S binary phase diagram and different equilibrium phases in this system. This diagram is presented in Figure 2.2. One of the important regions in this diagram is the Cu-Cu_2S miscibility gap extending from 1.2% to 19.5 w%S at 1250 °C. In this region, two liquids co-exist. Liquid I, which is the copper

metal phase, has a sulfur solubility of limited to 0.95-1 wt% at 1105 °C. while liquid II (sulphide phase), which is often called Cu_2S, has a sulfur solubility of 20-22.19 wt%. This range of sulfur solubility in the second liquid is within the single Cu_2S phase, meaning that the composition of the second phase may deviate from the exact stoichiometry.

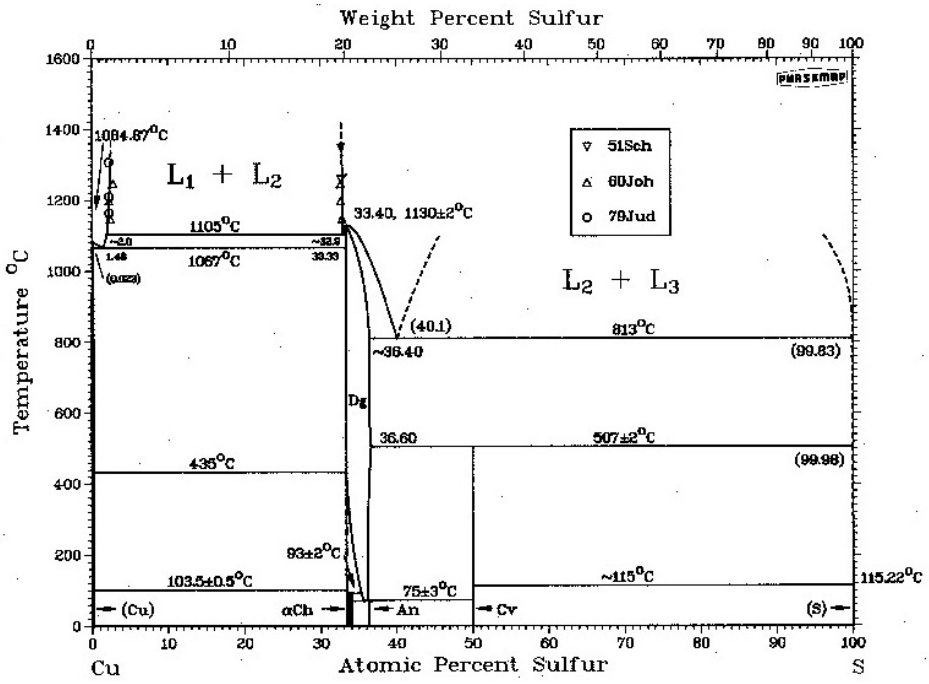

Figure 2.2 – Cu-S equilibrium phase diagram [25].

In two similar studies Schumann and Moles [37] and Bale [24] studied activities of Cu, S and Cu_2S in liquid Cu-S melts covering a wide compositional range from saturation with Cu to about 21.5 wt% S. To do that, they bubbled a controlled gas mixture of H_2 and H_2S

through the Cu-S melts in a closed furnace until an equilibrium was established for reaction (2.8) at different experimental temperatures of 1150 to 1350 °C.

$$Cu_2S\ (l) + H_2\ (g) = 2Cu\ (dissolved) + H_2S\ (g) \quad (2.8)$$

Then, by considering the experimental H_2S/H_2 ratios at equilibrium, performing chemical analysis for S and Cu content on the melts as well as combining the findings with Kelley's data [31] reported for dissociation of H_2S, Schumann and Moles [37] proposed the following empirical equation for the sulfur partial pressure (P_{S_2}) in the liquid Cu-S system at equilibrium:

$$\log P_{S_2} = \frac{-15505}{T} + 4.56 \quad (2.9)$$

Where P_{S_2} is the equilibrium partial pressure of S_2 gas and T is temperature in Kelvin.

In Figure 2.3, variations of sulfur partial pressure with mole fraction of sulfur in Cu-S liquids is demonstrated at different high temperatures. As it is seen in this figure, P_{S_2} increases with increasing temperature. P_{S_2} sharply increases from about 10^{-6} and 10^{-5} atm for copper sulphide liquids below Cu_2S in sulfur content to close to 1 atm for liquids saturated in S (excess of S over Cu_2S).

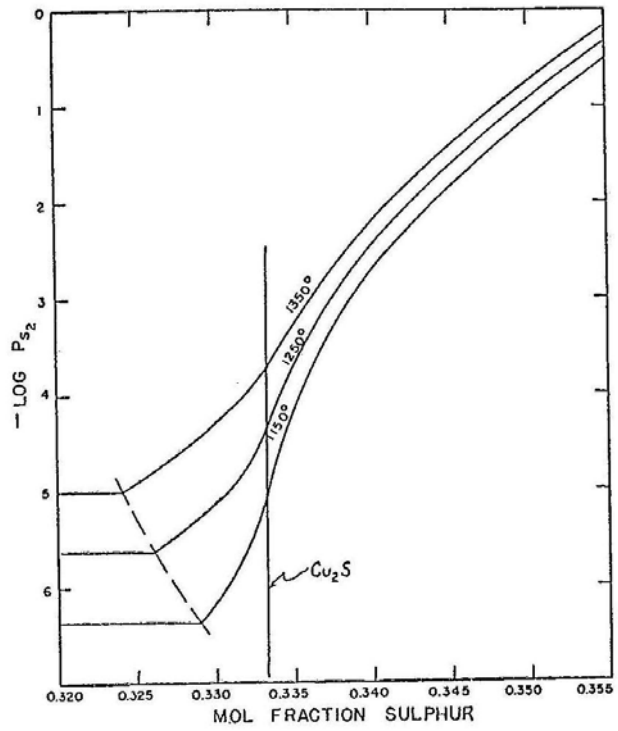

Figure 2.3 - Variations of sulfur partial pressure with mole fraction of sulfur in Cu-S liquids at different high temperatures of 1150 to 1350 °C [37].

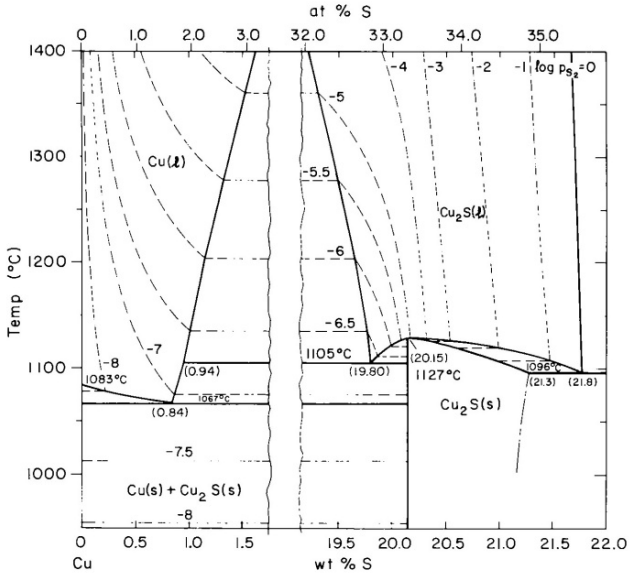

Figure 2.4 – Sulfur pressures (P_{S_2}) for liquid phases in the Cu-S system [28].

In Figure 2.4, obtained from the work conducted by Elliott [28], P_{S_2} values for liquid phases in the Cu-S system is illustrated for a wide range of compositions. In this figure, the miscibility gap is also clearly visible.

Using the Gibbs-Duhem integration, copper activities (a_{Cu}) can be calculated. Taking the components of the Cu-S system as Cu, Cu_2S and S, it can be written that:

$$X_{Cu_2S} \,.\, d\log a_{Cu_2S} + X_{Cu} \,.\, d\log a_{Cu} + X_S \,.\, d\log a_S = 0 \qquad (2.10)$$

For Cu-S liquids, $d\log a_{Cu_2S} = 0$. In addition, since a_S is proportional to (P_{H_2S}/P_{H_2}), therefore $d\log a_S = d\log P_{H_2S}/P_{H_2}$. Applying these relations [37]:

$$\log a_{Cu} = -\int \frac{X_S}{1-X_S} \,.\, d\log\left(\frac{P_{H_2S}}{P_{H_2}}\right) \qquad (2.11)$$

By having the equilibrium P_{H_2S}/P_{H_2} ratios and using the above integral, Schuhmann [37,42] and Bale [24] calculated a_{Cu} for Cu-S liquids with different content of sulfur at different temperatures.

Kellogg [32] critically reviewed the Cu-S binary system for the temperature range of 800-1600 K, in order to find an internally consistent set of selected values for the thermochemical properties of this system. His investigations covered a wide compositional range from near zero to more than 33.3 atom% sulfur (Cu_2S) in copper.

In Figure 2.5 provided by Kellogg [32], variations of activity coefficient of sulfur (γ_S) and copper (γ_{Cu}) as well as activity of stoichiometric copper sulphide (a_{Cu_2S}) with sulfur content of liquid Cu-S at two different temepratures of 1150 and 1350 °C is illustrated. It

is seen that as sulfur content of the liquid increases, γ_S increases and γ_{Cu} decreases. In this figure, $\gamma_S = P_{S_2}^{1/2}/X_S$, where X_S is the molar fraction of S in Cu_2S.

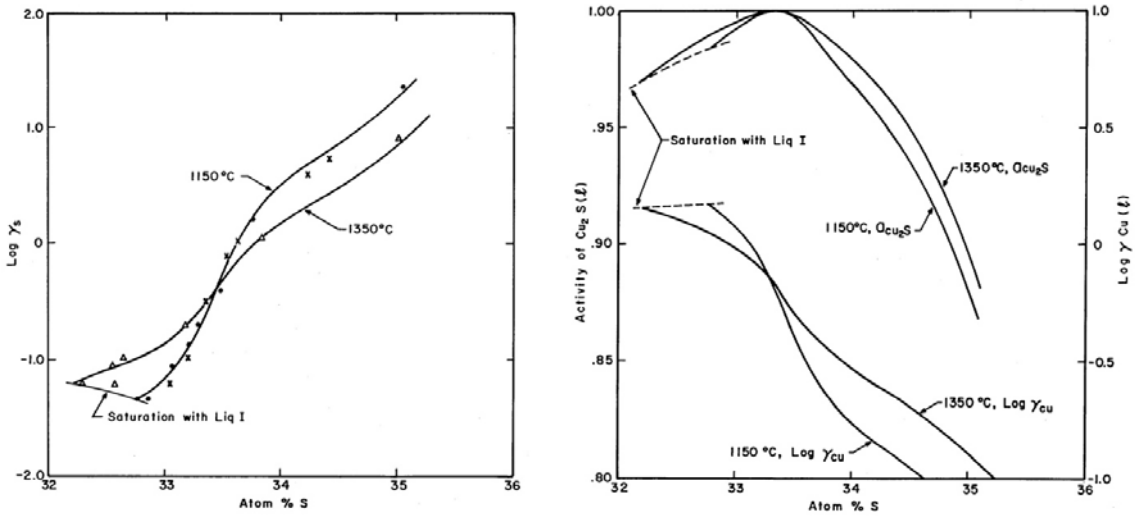

Figure 2.5 – Variations of activity coefficient of sulfur (γ_S) and copper (γ_{Cu}) as well as activity of stoichiometric copper sulphide (a_{Cu_2S}) with sulfur content of liquid Cu-S at two different temepratures of 1150 and 1350 °C [32].

Given the importance of Cu-S-O system in the copper converting process, phase equilibria and thermodynamics of this system has also received a considerable amount of attention from different researchers [17,28-30]. An isothermal section of the Cu-S-O ternary diagram at 1300 °C, given by Elliott [28], is shown in Figure 2.6. The difference between oxygen solubility between Cu_2S and sulfur saturated copper is illustrated in this Figure. By crossing the miscibility gap at 1300 °C, oxygen dissolved increases from 0.15 wt% in

the metal phase up to 1.35 wt% in the sulphide phase. As the sulphide phase becomes depleted of oxygen, oxygen content of the metal phase quickly rises.

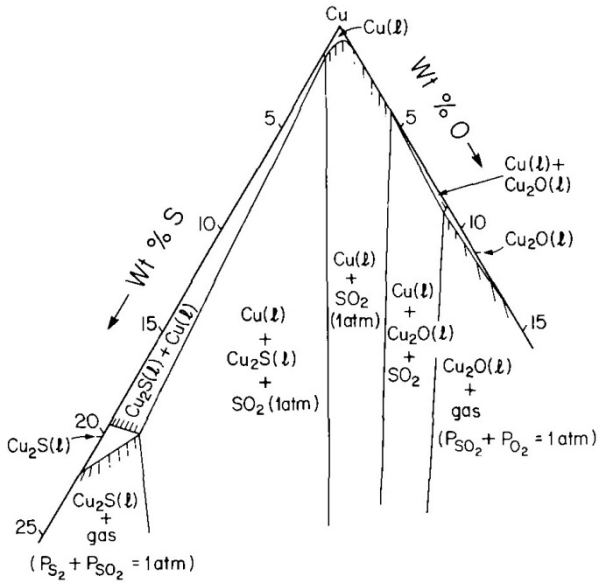

Figure 2.6 - The 1300 °C isotherm section of the Cu-O-S system (1 atm pressure). [28].

According to Alyaser [6,7], Cu-S-O system can be divided into two distinct sub-systems of ionic copper sulphide and the metallic copper melt. Copper sulphide sub-system has an ionic nature and due to the complexity associated with thermodynamic studies of ionic systems, its characteristics has not been fully evaluated yet.

Schmiedl [43] investigated Cu-S-O system and measured the oxygen and sulfur contents of the metal and sulphide phase in this system, as a function of SO_2 partial pressure and temperature. He expressed his measurements as the following mathematical forms:

For the metal phase:

$$wt\%O = 10^{(-1.38-(1278/T))} \times P_{SO_2}^{\frac{1}{2}} \quad (2.12)$$

$$wt\%Cu = 10^{(1.98+(24/T))} \quad (2.13)$$

$$\text{wt\%S} = 100 - \text{wt\%O} - \text{wt\%Cu} \quad (2.14)$$

For the sulphide phase:

$$wt\%O = 10^{(-1.96-(1013/T))} \times P_{SO_2}^{\frac{1}{2}} \quad (2.15)$$

$$wt\%Cu = 79.61 + (0.26 \times 10^{-12} \times T^4) \quad (2.16)$$

$$\text{wt\%S} = 100 - \text{wt\%O} - \text{wt\%Cu} \quad (2.17)$$

2.2.2. Thermodynamics of iron silicate slags

Slags containing high amounts of iron oxides are called "ferrous" slag. These slags are formed in various pyrometallurgical processes most importantly steelmaking and matte smelting [23]. If silica is also present, it is called "iron-silicate" slag. In acid steelmaking as well as copper matte smelting and converting, silica is added to the slag. In the latter case, it is done in order to remove iron along with slag from the process and thus increase the copper concentration in the matte. This happens through the formation of fayalite (Fe_2SiO_4) from FeO and SiO_2.

In order to have a good understanding of the phenomena which take place in copper matte smelting and converting, it is essential to have a detailed knowledge of the chemistry, properties and behaviour of iron-silicate slags in different compositional ranges and at various temperatures. In this regard, numerous researchers [44-55] have comprehensively studied the phase equilibria and thermodynamics of these important slags.

Bowen [56], Crook [44] and Darken [45] were among the first researchers who studied these slags. Bowen et al. [56] in 1932 presented a constitution diagram for the system FeO-SiO_2. Crook [44] in 1939 published his experimental results regarding general series FeO-Fe_2O_3-SiO_2-CaO (MgO) related to steelmaking slags. Their synthesized slags were prepared using two different crucibles made of iron and silica and at steelmaking temperatures up to 1600 °C. He subsequently performed chemical analysis on the quenched samples and analyzed their microstructure in order to identify the amount of available phases at different compositions and temperatures. He reported formation of two distinct

"eutectiferous" series of wüstite-fayalite and fayalite-tridymite when iron crucible was used. In contrast, it was reported that when iron oxide and silica were heated at 1600°C or higher in silica crucibles, no fayalite was detected and the synthesized slag consisted mainly of tridymite and magnetite. Crook argued that in these cases, the affinity of Fe_2O_3 for FeO was so strong that little or no FeO was allowed to form fayalite with SiO_2.

In 1950s, Schuhmann and co-workers [49,51,52] published a series of papers on phase equilibria and thermodynamics of iron-silicate slags, which covered a complete compositional range of slags saturated with wüstite, silica, magnetite as well as fayalite.

In the first of these studies, Schuhmann and Ensio [52] investigated thermodynamics of iron-silicate slags saturated with gamma iron (γ-Fe) by bubbling controlled gas mixtures of CO-CO_2 through the molten slags in iron crucibles at different temperatures of 1250-1400 °C. They carefully analyzed the composition of the outgoing gas and compared it to the ingoing gas mixture using gravimetric as well as thermal conductivity methods. Once the composition of the incoming and the outgoing gas mixtures became identical, the corresponding CO/CO_2 gas ratio was considered to be the required value to establish equilibrium for the following equation:

$$FeO\ (l) + CO = Fe\ (\gamma) + CO_2 \qquad (2.18)$$

After equilibrium was established, slag sampling was performed to determine the slag chemical composition namely for silica, total iron as well as ferric iron (Fe^{3+}). Subsequently, considering a_{Fe}=1 for slags saturated with γ-Fe, they determined activity of FeO in slags with known chemical compositions using the equilibrium CO/CO_2 ratio

obtained at various corresponding temperatures. The compositional range covered was equal to 61-93, 0-39 and 0.5-8.5 wt% for FeO, SiO_2 and Fe_2O_3, respectively and it included wüstite saturation as well as silica saturation.

In Figure 2.7 obtained from their paper, a diagram illustrating their results on the relation between log $\left(P_{CO_2}/P_{CO}\right)$ to 10^4/T is presented for the entire range of stability of iron-silicate slags in contact with solid iron.

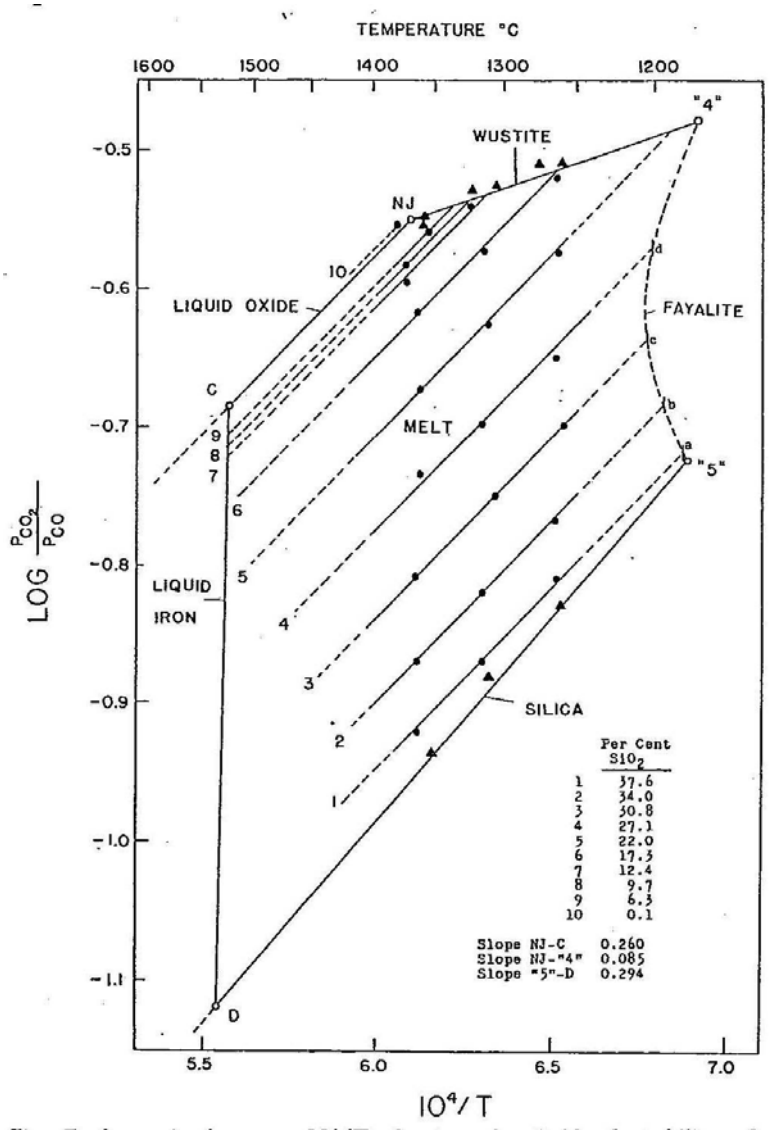

Figure 2.7 – Log $\left(P_{CO_2}/P_{CO}\right)$ vs. 10^4/T illustrating the field of stability of iron silicate slags in equilibrium with solid Fe [52].

In Figure 2.7, range of stability is shown by the closed area C-NJ-4-5-D and each curve corresponds to a specific case as follow: 5-D: silica saturation, 5-4: fayalite saturation, NJ-4: wüstite saturation, D-C: melting point of iron and C-NJ: slags of zero percent silica.

In addition, several curves corresponding to various molten slags with different content of silica is illustrated in the diagram.

Schuhmann and Ensio [52] suggested the following two important conclusions from the diagram presented in Figure 2.7:

1- At constant temperature, a_{FeO} decreases with increasing silica content of the slag as $\left(P_{CO_2}/P_{CO}\right)$ significantly decreases. This is because at constant temperature, K (equilibrium constant) of reaction (2.18) is constant and since K equals $\left(P_{CO_2}/P_{CO}\right).(a_{FeO})^{-1}$, then as partial pressure ratio of CO_2 over CO decreases, activity of FeO also decreases. In fact, they reported that a_{FeO} was lowest for the case of silica-saturated slags in contact with solid iron.
2- Same slopes is observed for slags saturated with iron with different content of silica. This means that for a slag with a given silica content, a_{FeO} does not vary significantly with temperature. In fact, they reported that variations of activity of FeO fell within the experimental error of less than 2 percent.

Combining Gibbs free energy data for reaction (2.18) at equilibrium with the experimental data obtained for $\left(P_{CO_2}/P_{CO}\right)$ at different temperatures, Schuhmann and Ensio [52] proposed the following relations for the variation of activity of FeO with temperature for slags saturated in iron with different silica content (equation 2.19) and for slags saturated in both iron and silica (equation 2.20).

$$\log a_{FeO} = \log\left(\frac{P_{CO_2}}{P_{CO}}\right) - \frac{2640}{T} + 2.157 \qquad (2.19)$$

$$\log a_{FeO} = \frac{300}{T} - 0.590 \quad (2.20)$$

In Figure 2.8, variations of activities of FeO and SiO_2 with silica content of iron-silicate slags saturated with iron is presented at two different temperatures. They determined the activities of SiO_2 by a Gibbs-Duhem integration presented as Equation (2.21) for iron-silicate slags saturated in iron (a_{FeO}=1). In fact, Schuhmann later in a separate paper [57] elaborated in more details how to apply Gibbs-Duhem equations to ternary systems. In Equation (2.21), N_O and N_{SiO_2} correspond to mole fraction of oxygen and silica in the slag, respectively.

$$\log a_{SiO_2} = -\int \frac{N_O}{N_{SiO_2}} . d \log a_{FeO} \quad (2.21)$$

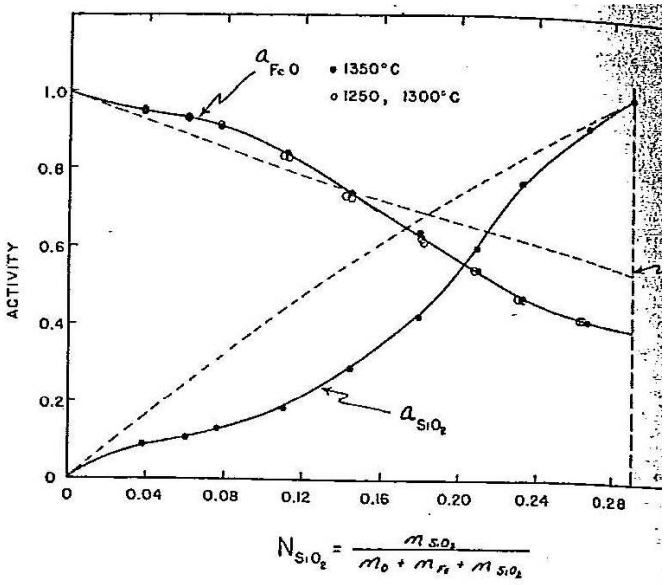

Figure 2.8 – Variations of activities of wüstite and silica (a_{FeO} and a_{SiO_2}) with molar fraction of silica (N_{SiO_2}) for iron-saturated iron-silicate slags at various temperatures [52].

As it is seen in Figure 2.8, by increasing mole fraction of silica in the slag, a_{SiO_2} increases, while in contrast, a_{FeO} decreases. However, activity-composition variations do not follow the behavior expected for an ideal binary solution of FeO and SiO_2 (i.e. shown as dashed lines). The vertical dashed line in the right-hand side of the figure corresponds to silica saturated slag at 1300 °C. It is seen that a_{FeO} is roughly equal to 0.4 in silica-saturated iron-saturated slags. Other researchers have reported similar results for a_{FeO} [34,41]. Yazawa [34,41] determined that a_{FeO} was equal to 0.30 in silica-saturated iron-saturated slags at 1200 °C.

In another paper in 1952, Michal and Schuhmann [49] studied thermodynamics of iron-silicate slags saturated with solid silica at high temperatures of 1250 to 1350 °C. They used controlled amounts of CO-CO_2 gas mixtures and the procedure employed was similar to what was explained before, with only one difference that in this study they used silica crucible in order to have slags saturated with silica. Their experimental measurements covered the entire composition range of silica-saturated iron-silicate slags including slags saturated with both silica and ɣ-iron as well as silica and magnetite.

In Figure 2.9 obtained from their paper, a diagram illustrating experimental results obtained on the relation between log $\left(P_{CO_2}/P_{CO}\right)$ to 10^4/T is presented for the entire range of stability of iron-silicate slags in contact with solid silica. Different ranges of stability are shown in the figure as an enclosed area made by three curves of saturation with ɣ-Fe, fayalite and magnetite.

According to Michal and Schuhmann [49], for cases which P_{CO_2}/P_{CO} and T fall anywhere outside the enclosed area, no stable slag saturated with silica can exist. In addition, experimental results obtained by previous researchers are shown in this figure, which are in good agreement with the results of Michal and Schuhmann [49]. Horizontal dashed lines in this figure correspond to silica-saturated iron-silicate slags with different values of N_O/N_{FeO}(molar fraction ratio of oxygen over FeO). The reason these lines are horizontal is that their experimental results showed that in silica-saturated slags with given N_O/N_{FeO}, variations of $P_{CO_2}/P_{CO}$with temperature was negligible and fell within the experimental error, although they admitted that this was a "coincidence".

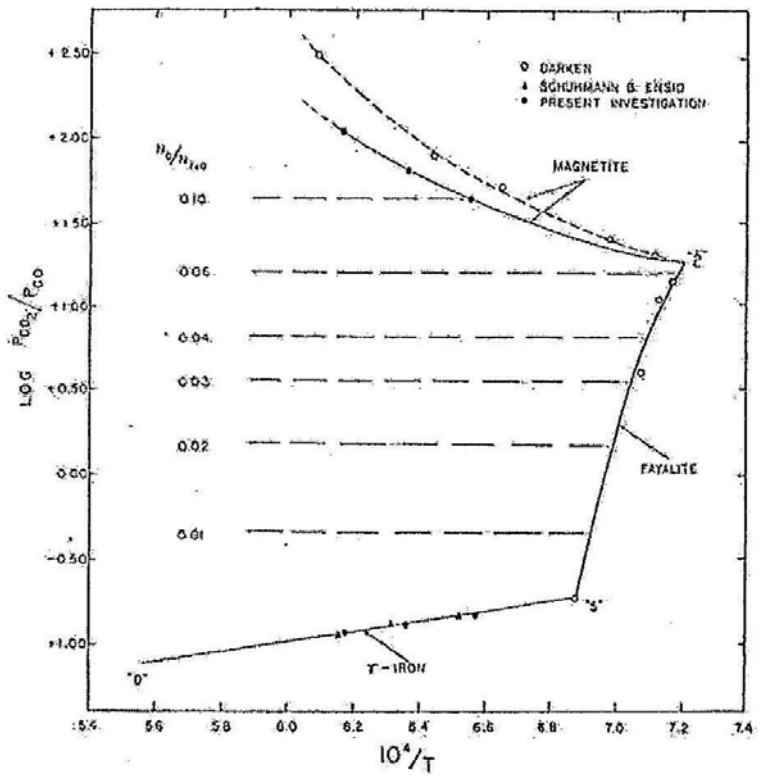

Figure 2.9 – Log $\left(P_{CO_2}/P_{CO}\right)$ vs. 10^4/T illustrating the field of stability of silica-saturated iron silicate slags [49].

Using Gibbs free energy data available for reaction (2.22) at equilibrium, a relation was subsequently reported for variations of oxygen pressure with P_{CO_2}/P_{CO} and temperature, which is shown as relation (2.23). Partial pressure of oxygen can then easily be related to activity of oxygen in the slag.

$$2CO\ (g) + O_2\ (g) = 2CO_2\ (g) \tag{2.22}$$

$$\log P_{O_2} = 2\log\left(\frac{P_{CO_2}}{P_{CO}}\right) - \frac{29270}{T} + 8.921 \tag{2.23}$$

Considering reaction (2.18) and equation (2.19), activity of Fe in different slags at equilibrium can be presented as:

$$\log a_{Fe} = \log a_{FeO} - \log\left(\frac{P_{CO_2}}{P_{CO}}\right) + \frac{2640}{T} - 2.157 \quad (2.24)$$

Activity of FeO in silica-saturated slags can be calculated by a Gibbs-Duhem integration, similar to what was explained previously for iron-saturated slags, but with a difference that here instead of Fe, activity of silica (a_{SiO_2}) is equal to 1. The following relation was obtained by Michal and Schuhmann [49]:

$$\int d.\log a_{FeO} = -\int \frac{N_O}{N_{FeO}}.d\log\left(\frac{P_{CO_2}}{P_{CO}}\right) \quad (2.25)$$

In Figure 2.10, the effect of slag composition on activity of different components of silica-saturated iron-silicate slags is demonstrated at a constant temperature of 1300 °C. It is seen that a_{FeO} is almost constant throughout the entire compositional range and is equal to approximately 0.4. This finding was also reported previously by Schuhmann and Ensio [52] and can be seen in Figure 2.8. On the other hand, a_{Fe} decreases from 1 (for iron-saturated slags) to about 0.0016 for magnetite-saturated slags as the slag becomes more oxidizing. Two vertical dashed lines in the figure correspond to iron-saturated and magnetite-saturated silica-saturated slags.

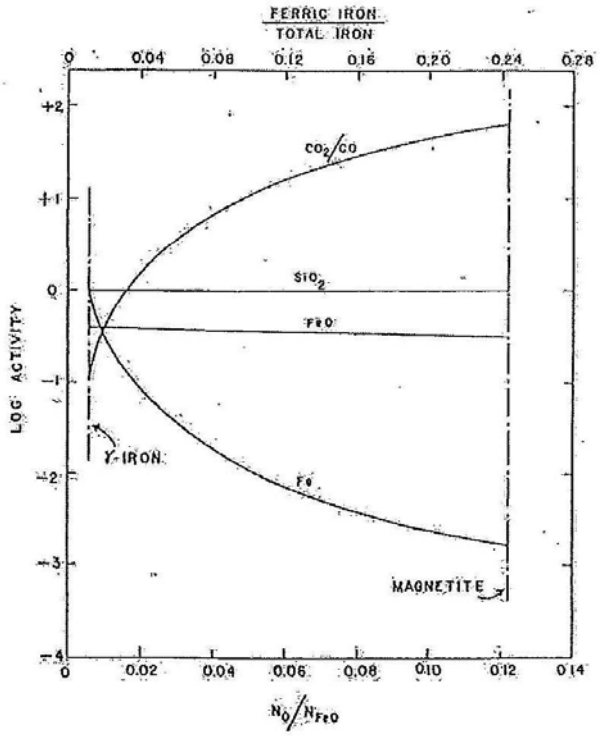

Figure 2.10 – Activity-composition relations in silica-saturated iron-silicate slags at 1300 °C [49].

Schumann et al. [51] later in 1953 published a paper on determination of the liquidus surfaces in the FeO-Fe_2O_3-SiO_2 system. They studied a wide range of compositions of iron-silicate slags at different temperatures relevant to copper pyrometallurgy from 1250 to 1450 °C. Their procedure consisted of equilibrating known samples of FeO, Fe_2O_3 and SiO_2 in platinum crucibles, quenching, and performing microscopic as well as chemical analysis on the quenched samples synthesized at different temperatures in order to determine the phases present. The phases present included liquid, wüstite, hematite, magnetite and silica (tridymite).

In Figure 2.11, two examples of the isothermal sections of ternary FeO-Fe_2O_3-SiO_2 phase diagram at 1350 and 1450 °C constructed by Schuhmann and co-workers, is presented [51]. Using these diagrams, it is possible to determine the stable phase at a given temperature for an iron-silicate slag with known initial composition.

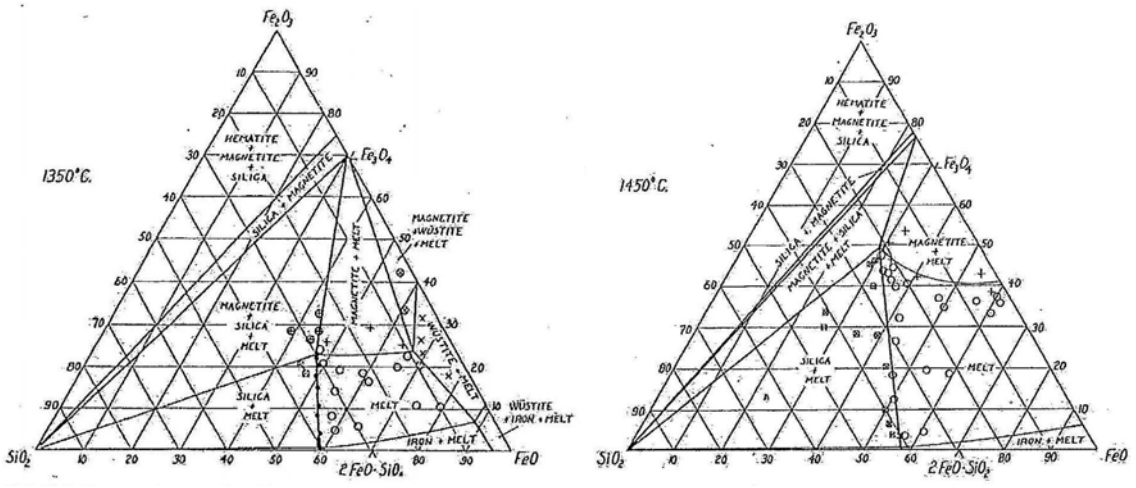

Figure 2.11 – Examples of isothermal sections of ternary FeO-Fe_2O_3-SiO_2 phase diagram at 1350 and 1450 °C constructed by Schuhmann and co-workers [51].

Subsequently by combining their results with the data available in the literature at the time, Schuhmann et al. [51] constructed a liquidus diagram for FeO-Fe_2O_3-SiO_2 system, which covered the entire temperature-composition field of stability of iron silicate slags at 1 atm. This diagram, which is of considerable interest for copper smelting and converting, is illustrated in Figure 2.12. Using this diagram, it is possible to know the stable phase as

well as the liquidus temperature for a known composition of iron silicate slag. Some of the important indications of this diagram are [51]:

- All the low melting iron-silicate slags have compositions close to that of fayalite ($2FeO.SiO_2$ or Fe_2SiO_4).
- Cooling down a slag high in ferric iron (Fe^{3+}), will result in formation of significant amount of magnetite by the time temperature reaches to 1200 °C and the remainder of ferric iron will eventually form as magnetite if it continued to cool down slowly to room temperature.
- Two aforementioned findings indicate that FeO is a good flux for silica. Whereas, magnetite and in particular hematite are not.
- The straight isotherm lines in silica liquidus indicate that SiO_2/FeO ratio is almost independent of the hematite content of the slag for silica-saturated iron silicate slags. It is because the extensions of these lines come close to the hematite corner of the diagram.
- For a typical converter slag with 10-15 wt% Fe_2O_3, 55-60 wt% FeO and 25-30 wt% SiO_2, magnetite is the stable phase as such a composition falls in the magnetite liquidus surface of the diagram.

A similar FeO-Fe_2O_3-SiO_2 ternary diagram with information about liquidus temperatures as well as equilibrium P_{O_2} values was also reported by Goel et al. [46] (Figure 2.13) who provided a detail mathematical description of the thermodynamic properties of Fe-O and Fe-O-SiO_2 systems.

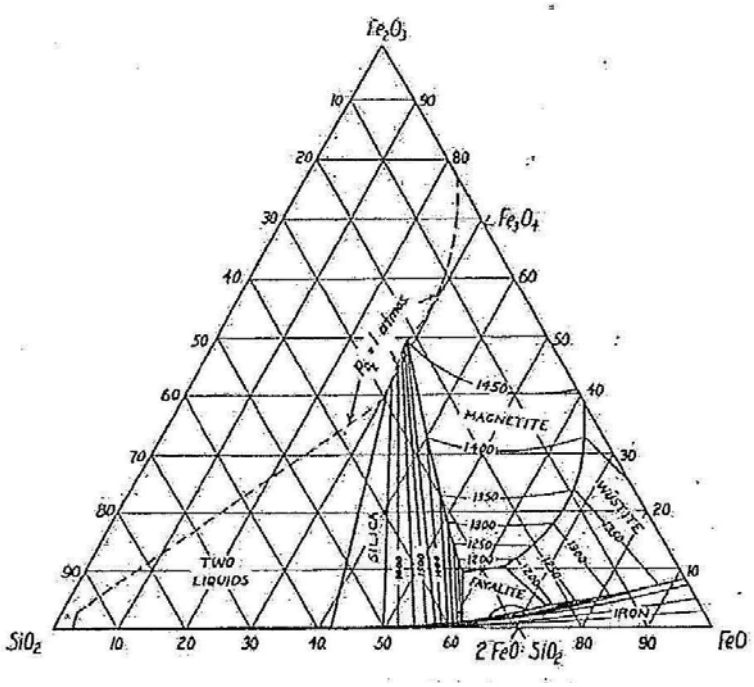

Figure 2.12 – Liquidus diagram for FeO-Fe_2O_3-SiO_2 system, covering the entire temperature-composition field of stability of iron silicate slags at 1 atm. [51].

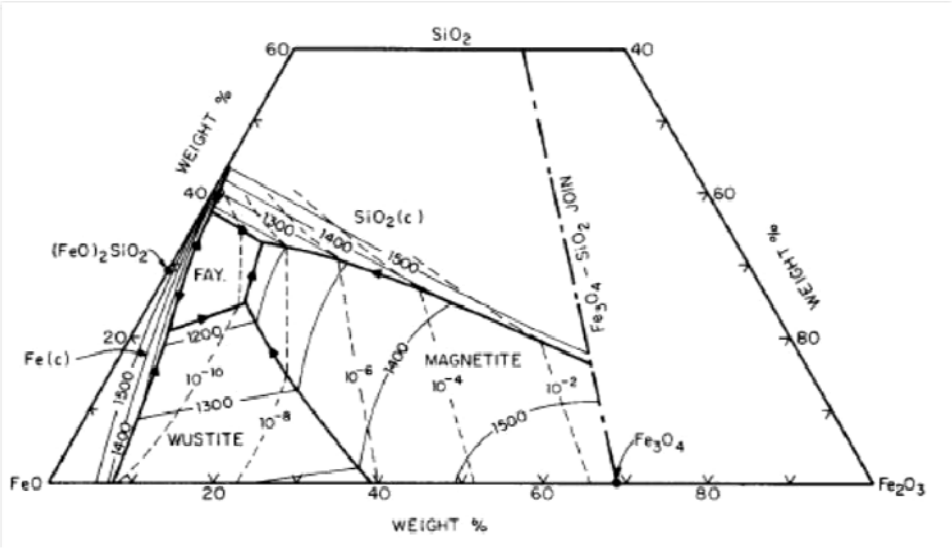

Figure 2.13 – System FeO-Fe_2O_3-SiO_2 projection of the liquidus surface. Heavy lines are phase boundaries; light lines are liquidus isotherms (°C); dashed lines are oxygen isobars (P_{O_2}, atm) [46].

The amount of oxygen solubility in fayalite slags was also determined by Schuhmann et al. [51]. Oxygen solubility at a given temperature was defined as "the maximum quantity of oxygen that can be dissolved without precipitating a new phase ". In Figure 2.14, it is seen that by increasing temperature, oxygen solubility in fayalite slags increases. According to this figure, the limit of oxygen solubility at any temperature below 1380 °C is the onset of magnetite precipitation. Whereas, precipitation of silica limits the oxygen solubility at temperatures above 1380 °C.

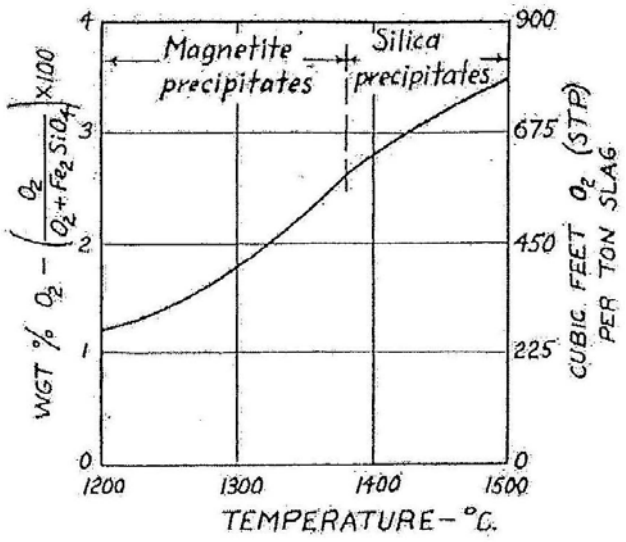

Figure 2.14 – Variations of oxygen solubility with temperature in fayalite slags [51].

According to Matousek [48], the oxidation state of slags (oxygen potential) in Fe-O-SiO_2 system is controlled by the redox reaction between ferrous (Fe^{2+}) and ferric iron (Fe^{3+}):

$FeO + ¼\ O_2 = FeO_{1.5}$ (2.26)

For this reaction [46]:

$$\log K = -2.83 + \frac{6630}{T} \quad (2.27)$$

where $K = \frac{a_{FeO_{1.5}}}{a_{FeO} \cdot P_{O_2}^{1/4}}$ (2.28)

Matousek [48] proposed Equation (2.29) for P_{O_2} in iron silicate slags where $\frac{Fe}{SiO_2} \cong 1.6\text{-}3.06$, $10^{-12} < P_{O_2} < 10^{-4}$ (atm) and 1162 < T < 1492 °C.

$$\log P_{O_2}(atm) = 16.1 + 3.92 \log\left(\frac{Fe^{3+}}{Fe^{2+}}\right) - 1.05 \frac{pct\ (Fe)}{pct\ (SiO_2)} - \frac{29500}{T} \quad (2.29)$$

2.3. Kinetic studies

There is little information available in the literature on the desulphurization of matte by the slag phase. However, plenty of studies have been conducted on the decarburization kinetics of Fe-C metal droplets with FeO bearing slags. Therefore, in this section, first a summary of the investigations and findings on metal droplet/slag interactions and corresponding reaction kinetics in steelmaking will be provided and then oxidation kinetics of molten copper sulphide when an oxidizing gas mixture is blown to the molten matte will be briefly discussed.

2.3.1. Decarburization kinetics of Fe-C metal droplets

Many reactions happen during steelmaking process, but the reaction of FeO in the slag with carbon in the metal (reaction [2.30]) enjoys a specific importance as it reduces the iron oxide present in the slag to molten iron and causes it to transfer from slag to metal. In addition, through the production of CO gas, it leads to foam formation, which is highly sought in this process.

$$(FeO) + \underline{C} = Fe\ (l) + CO\ (g) \qquad (2.30)$$

Using X-ray, Mulholland et al. [58] were the first who reported the formation of a gas halo around metal droplets of Fe-C-S (0.8 to 4.5 wt% C and 1 wt% S) while reacting with an oxidizing slag (47 wt% CaO, 38 wt% SiO_2, 15 wt% Al_2O_3 and 10-30 wt% Fe_2O_3) in temperature range of 1723-1873 K. In the presence of a gas halo, the effect of gas/metal

and gas/slag interfacial reactions on the decarburization reaction (reaction [2.30]) also needs to be considered.

Different researchers have studied the possible rate-determining steps in the decarburization reaction. In his study of the reaction kinetics of Fe-C-S metal droplets (2.3 to 4.2 wt% C and 0.001 to 0.08 wt% S) with $CaO-SiO_2-Al_2O_3-FeO$ slag (FeO content varies from 2 to 10 wt%) in temperature range of 1673 to 1723 K, Fruehan [59] proposed the following five potential rate controlling mechanisms:

(1) Gas-metal reaction (Boudouard reaction): $CO_2\ (g) + \underline{C} = 2CO\ (g)$ (2.31)

(2) Gas-slag reaction : $CO\ (g) + (FeO) = CO_2\ (g) + Fe\ (l)$ (2.32)

(3) Mass transfer of FeO as Fe^{2+} and O^{2-} ions through the slag

(4) Mass transfer of C through the metal droplet

(5) Mass transfer of CO and CO_2 through the gas halo.

The above mechanisms are schematically shown in Figure 2.15.

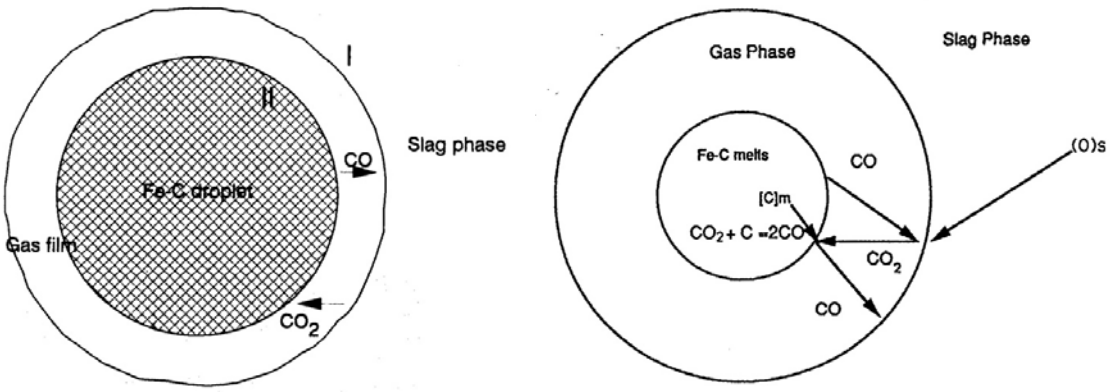

Figure 2.15 – Schematic diagram of the reaction of an Fe-C metal droplet with FeO in the slag. Left figure is from Krishna et al. [60] and the right figure is from Min et al. [61].

Min et al. [61] and Fruehan [59] believed that the reaction between FeO in the slag with Fe-C metal droplet occurs through a two-step reaction, with CO-CO_2 acting as gas intermediates. In Figure 2.15, it is seen that reaction (2.30) happens at the metal/slag interface. Once it is occurred, CO gas is generated and gas halo is formed and further decarburization is proceeded through the gaseous species. FeO continues to be reduced by CO now at the slag/gas interface as indicated by reaction (2.32). Reaction (2.31) also happens between CO_2 in the gas phase and carbon in the metal droplet at the gas/metal interface.

According to Fruehan [59], steps (2), (4) and (5) were fast and did not have an effect on the decarburization rate in the temperature range studied. He argued that step (1) (reaction [2.31]) was rate-limiting only if the sulfur content of the metal droplet was above 0.01 wt%. It could be due to behaviour of sulfur as a surface-active element and its poisoning

of the reaction sites. In addition, step (1) could be rate-limiting at lower than steelmaking temperatures as it is a very endothermic reaction. Finally step (3) is reported to contribute to the overall reaction rate.

Constant Volume Pressure Increase (CVPI) method is used for determining the rate of the reaction (2.30) in which 1 mole of CO gas produced is equal to 1 mole of FeO reduced. As Molloseau et al. [62] believed, a small amount of CO_2 can also form. Although the maximum possible amount of CO_2 that could be produced for the highest FeO contents was reported to be less than 9%, but the amount of CO_2 was negligible in their study.

The parameters influencing the rate of the decarburization by FeO-containing slags have been investigated thoroughly by many researchers during the past decades, using the aforementioned method. Here the effect of different parameters on the rate of the decarburization reaction will be discussed.

Effect of chemical composition of metal droplet and slag

Chemical composition of the metal droplet and slag could have a significant influence on the rate of the decarburization reaction. They have been considered in almost every study that has been done on the kinetics of the decarburization of metal droplets in oxidizing slags. Here the effect of different elements on the rate of the decarburization reaction is studied.

2.3.1.a. Effect of slag oxygen potential

From the literature, slag oxygen potential appears to be the most important factor affecting the decarburization rate for a given carbon content. Chen and Coley [63] reported an increase in CO evolution rate by an increase in FeO content of the slag, but they have stated that this relationship is neither linear nor exponential. Similar observations have also been reported by other researchers [61,62].

In Figure 2.16 obtained from the study conducted by Molloseau et al. [62], total moles of CO evolved as a function of time is plotted for 3 to 30 wt% FeO at 1713 K. CO evolution is the result of the decarburization reaction happening after placing Fe-C-S (2.91 wt% C and 0.011 wt% S) droplets in the CaO-SiO_2-MgO-FO slag. It is seen in the figure that FeO content of the slag largely influences the CO evolution rate. In addition, it is understood from the figure that for slags with more than 10 wt% FeO, two distinctive rates (defined by the slope of the linear portion of the data $\Delta n_{CO}/dt$) is observed. Whereas for slags below 10 wt% FeO, only one distinctive rate is seen.

CO evolution rate for the cases with less than 10 wt% FeO is estimated to be 3.0×10^{-6} moles/s, which is about two orders of magnitude slower than the initial rate measured for the samples with 20 and 30 wt% FeO present in the slag. Molloseau et al. [62] believed that the rapid decarburization rate observed in their study when dealing with a slag with FeO content of more than 10 wt% was due to droplet becoming emulsified. Surface area increases drastically once a droplet emulsifies and as a result the rate of the decarburization reaction increases. They argued that emulsification behaviour only

happened when slags with FeO content of more than 10 wt% were employed. Therefore, they have reported a small CO dependence to FeO content of the slag for slags having less than 10 wt% FeO and a high CO dependence when slags have more than 10 wt% FeO.

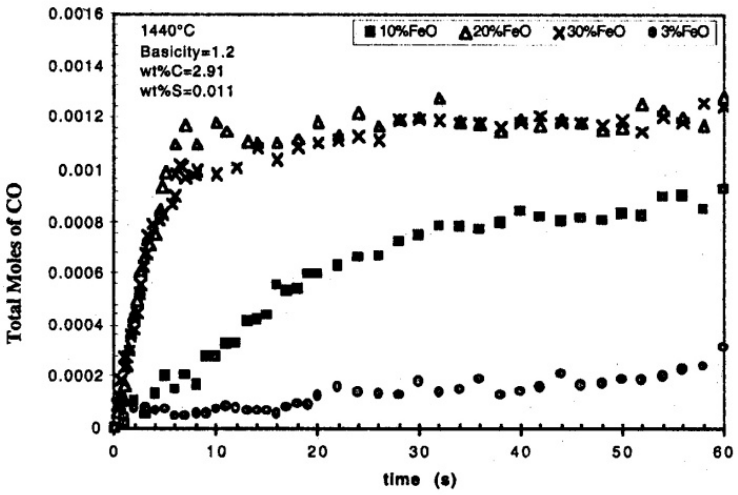

Figure 2.16 – Variations of the total moles of CO evolved with time (s) for 3 to 30 wt% FeO at 1713 K (weight of the metal droplet = 1.0 to 1.1 g) [62].

In their study Mulholland et al. [58] reported that while FeO-containing slags led to the formation of small bubbles and slow rise of the small amount of the foam produced, slags containing Fe_2O_3 however caused more violent and extensive decarburization reaction leading to rapid rise of foam. In addition, regarding the importance of oxygen in decarburization reaction, it has been reported that if a droplet was plunged into the foam

phase, decarburization reaction was proceeded much faster than in the dense slag layer, due to the higher oxygen content in the foam.

In contrast to many studies which have reported a non-linear increase in the decarburization rate by an increase in FeO content of the slag, Krishna Murthy et al. [64] believed that the relationship was linear (Figure 2.17). They had studied the decarburization of Fe-C droplets in contact with an FeO containing slag at 1823 K and reported a linear increase in the rate with increasing FeO content of the slag.

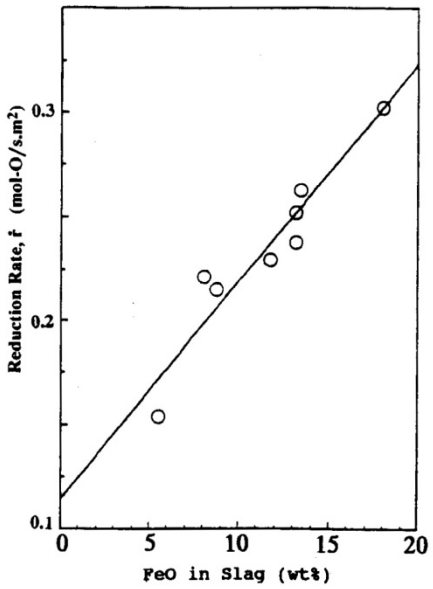

Figure 2.17 – Variations of the reduction rate with FeO content of $CaO - SiO_2 - Al_2O_3$ slag at 1823 K [64].

In Figure 2.18. obtained from the work conducted by Min et al. [61] on the decarburization of a 5-g Fe-C metal droplet with a FeO-containing slag, the effect of FeO content of the

slag on the rate of carbon loss is illustrated. As it can be seen in the figure, reaction reaches a steady state rate after an incubation period of about 10 to 15 second and considerably slows down afterwards once reaching to a certain low carbon level which depends on the FeO content of the slag. The carbon content at which the reaction slows decreases with increasing FeO content of the slag.

Many researchers [61,63,65,66] have observed the presence of an incubation period and a broad range of theories have been mentioned to justify this phenomenon. Min et al. [61] have argued two potential reasons; a) droplet needs some time to reach to the reaction temperature as its initial temperature is lower than the final reaction temperature and b) a finite time is needed to establish the gas halo necessary for the reaction to proceed at a reasonable rate. However, some other researchers [63,65] simply have argued that this period is due to the time needed for the oxygen build up on the droplet surface and then occurrence of the decarburization reaction.

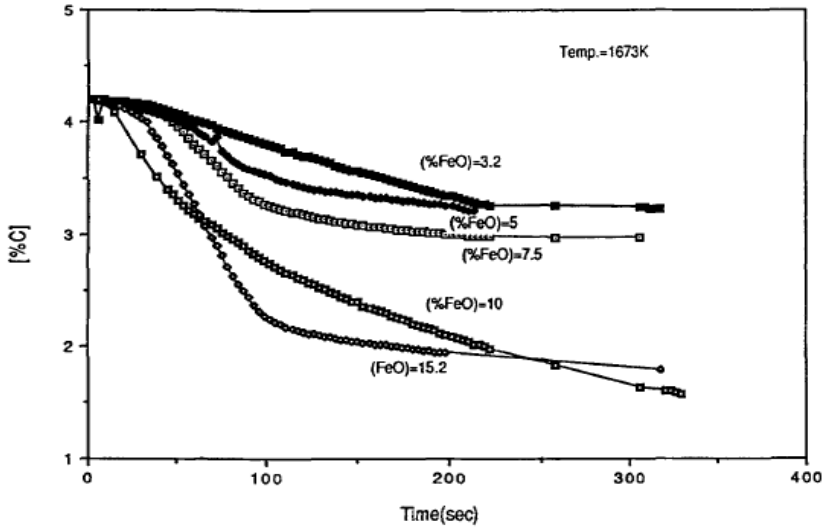

Figure 2.18 – Rate of carbon loss from the metal drop (5.3 g) containing initially 4.2 wt% C and 0.001 wt% S as a function of time for various FeO contents of slag [61].

2.3.1.b. Effect of carbon content of the metal droplet

High carbon content

Carbon content of the droplet also plays an essential role on the rate of the decarburization reaction [C + (O) = CO]. In general the greater the carbon content of the droplet, the faster CO evolution and thus the greater the decarburization rate. Once a droplet with high carbon content (more than 3 wt%) gets in contact with an oxidizing slag, CO bubbles form through a very rapid and violent decarburization reaction leading to almost immediate formation of a gas halo around the droplet [58,63,65].

However as Mulholland et al. [58] suggested there would be a period of inactivity (about a few minutes) before the foam forms and begins to rise. This might be due to the fact that once a gas halo is formed, the interfacial contact between droplet/slag is lost and further decarburization is only possible through the gas phase. In this condition, decarburization rate will depend on the following steps:

1) Production of CO_2 at the gas/slag interface or its transport through the gas phase (reactions [2.32] and step [5]).
2) CO gas evolution through the gas-solid reaction (reaction [2.31]).

Decarburization rate can only be less or equal to the rate of the above reactions.

Additionally, formation and then rise of huge foams in the case of droplet with high carbon content has been reported. Mulholland et al. [58] have experienced formation of a huge foam of over 500 mm using a droplet with 4.5 wt% carbon content.

In Figure 2-19, it is illustrated that CO evolution rate increases as FeO content of the slag (slag oxygen potential) increases. In addition, it is clear in the figure that carbon content of the metal droplet has a considerable influence on the rate. CO evolution rate increases as the carbon content of the droplet increases, but this increase does not seem to be linear. In Figure 2.20 similar behaviour is seen.

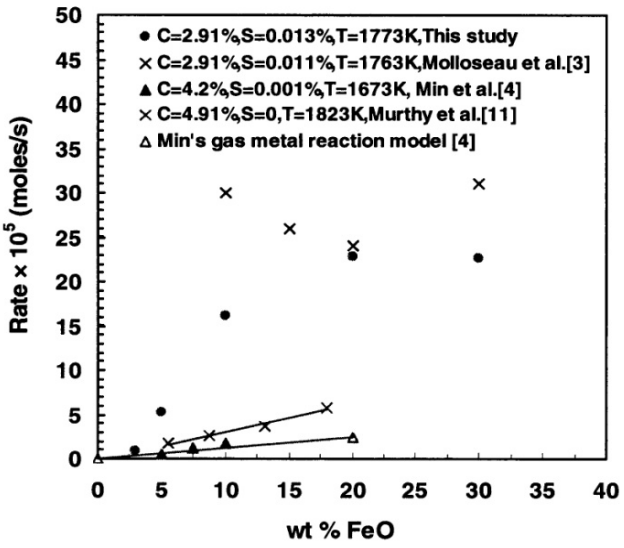

Figure 2.19 – CO evolution rate as a function of FeO content of the slag and carbon in the drop [63,65].

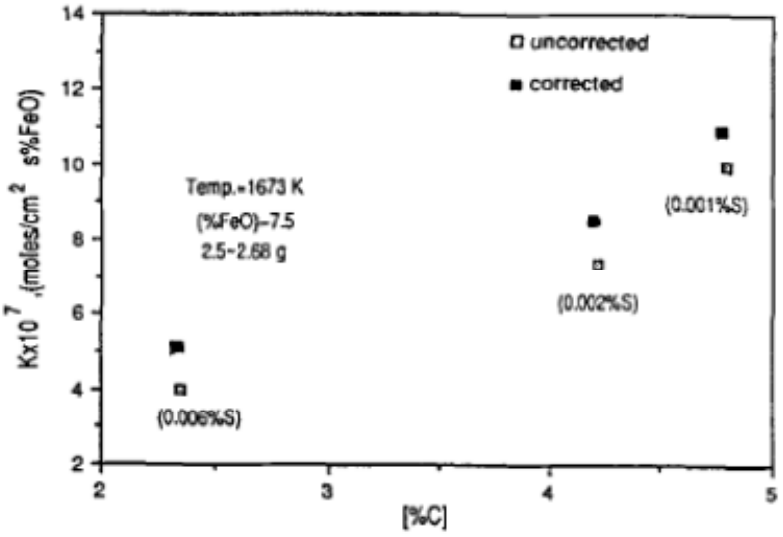

Figure 2.20 – The rate constant for 2.5-g drops at 1673 K as a function of carbon content [61].

In Figure 2.21, different steps of CO nucleation inside the metal droplet in contact with FeO-containing slag is demonstrated. CO nucleation inside the droplet has led to droplet swelling. This phenomenon is especially reported when the rate of oxygen transfer from the slag is much faster than the rate of carbon transfer from the drop to the interface.

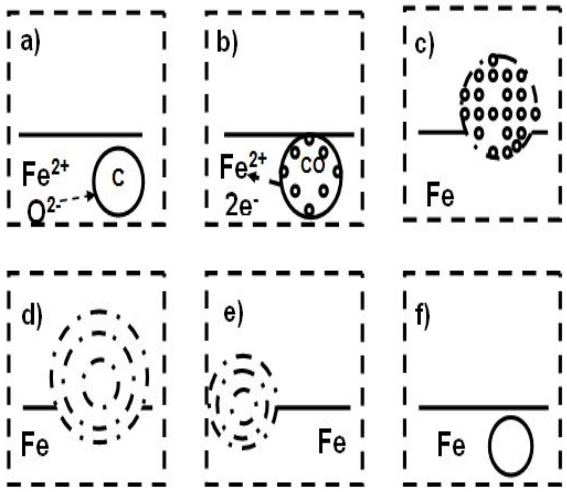

Figure 2.21 – Elementary steps of metal droplet reaction with slag to form a big swelling [63,65].

Low carbon content

When a droplet with low carbon content (less than 2 wt%) gets in contact with an oxidizing slag, CO bubbles form. However, the decarburization rate is obviously less than the case of droplet with higher carbon content. Different observations have been reported regarding the formation of a gas halo around the droplets with low carbon content. Some researchers [63,65] argued that since the transport of carbon to the interface of metal

droplet/slag cannot keep up with the supply of oxygen from the slag, CO bubble nucleation happens inside the droplet leading to droplet swelling (Figure 2.21). However, some other researchers have not reported droplet swelling [58,61]. A period of inactivity for the first few minutes of droplet/slag contact and then onset of CO evolution followed by the formation of a gas halo and rise of the foam has been reported by Mulholland et al. [58]. Although they observed CO bubble nucleation at the slag/metal interface, they did not report any swelling though.

Effect of impurities on the decarburization rate

Interface chemistry greatly influences the interfacial reactions such as decarburization. Thus, for having an acceptable understanding of the decarburization process, considering the effect of other elements present at the interface between slag and metal droplet is necessary. Below, the effects of some of the most important elements on the rate of the decarburization is discussed.

2.3.1.c. Effect of sulfur content of the metal droplet

Sulfur usually exists in materials mainly from the metal ore. As it is a surface-active element, it usually has a significant influence on the refining in metallurgical processes. The effect of the presence of sulfur in the metal droplet on the decarburization reaction has been studied by many researchers [60-62,67].

According to the "site-blockage" model, sulfur being a surface-active element occupies the reaction sites at the droplet/slag interface and consequently tremendously slows down the reaction. In such a condition fewer reaction sites would be available for oxygen to react with carbon and therefore CO nucleation rate decreases.

In contrast, it has been reported that very low traces of sulfur in the metal droplet could promote the rate of the decarburization reaction. Chen and Coley [63,65] in their study of the reaction between Fe-C-S metal droplets with an oxidizing slag have reported that the maximum decarburization rate at T=1773 K was obtained for the droplet with 0.0126 wt% sulfur content.

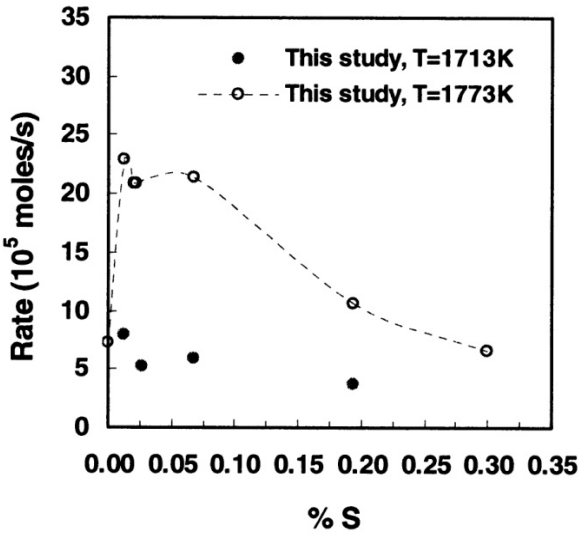

Figure 2.22 – Variations of CO evolution rate with sulfur content of the metal droplet [63,65].

As it is illustrated in Figure 2.22, CO evolution rate first dramatically increases with just a small increase in sulfur content of the metal droplet and after reaching to a maximum falls down with further sulfur increase. It has been argued [62,63,65] that in the presence of sulfur, two competing phenomena happen; a) decrease in the metal surface tension and b) sulfur segregation and poisoning of the reaction sites. Small traces of sulfur in the metal droplet could reduce the energy barrier for CO nucleation by decreasing the metal surface tension leading to a jump in the decarburization rate. But further increase in sulfur content of the metal droplet slows than the reaction by poisoning the reaction sites.

Molloseau et al. [62] have also reported these two competing effects. They have observed an increase in the rate of the decarburization by increasing the sulfur content of the metal droplet up to 0.011 wt%. They have postulated that this increase in rate is because sulfur decreases the surface tension of the metal droplet and thus enhances the emulsification of metal droplet, which leads to a significant increase in droplet surface area. But in agreement with others' observations, they have reported a decrease in the rate once sulfur content of the metal droplet further increased from 0.011 to 0.42 wt%. In addition, they believed that in high sulfur content, reaction [3.32] becomes the rate-controlling step.

Gaye et al. [67] have reported that the sulfur in the droplet enhances the Fe-C droplet emulsification.

In contrast to the above observations, Krishna Murthy et al. [64] have not observed any significant changes in the initial rate of the decarburization when adding sulfur amounts as high as 0.55 wt% to Fe-C metal droplets. They have argued that although sulfur

affected the interactions between droplet and slag and caused carbon to be reduced further but it did not have any significant effect on the rate. They had studied the kinetics of the decarburization of metal droplets in CaO-SiO_2-Al_2O_3-FeO slags at 1773 K. Their obtained results in this regard are illustrated in Table 2.1.

Table 2.1 – Effect of sulfur in Fe-C metal droplet on reduction rate of FeO [64].

	%C(slow)		%C(stop)		Droplet surface area A_d, cm^2		Reduction rate $\dot{r}$, mol O s^{-1} m^{-2}	
%S	1658 K	1713 K	1658 K	1713 K	1658 K	1713 K	1658 K	1713 K
0	2·71	2·42	1·637	1·773	3·34	1·9	0·045	0·1317
0·38	1·44	2·07	1·296	1·062	1·77	2·29	0·044	0·056
0·55	0·779	0·566	0·637	0·54	3·91	1·92	0·046	0·1683

* Droplet weight 2 g; 8·1%FeO. Slag compositions correspond to those given in Table 1.

Kozakevitch et al. [68] suggested that sulfur has a dynamic, rather than a static, blocking effect as they reported it did not interfere with the carbon removal when dealing with sulfur-saturated slags where it does not transfer to the slag anymore.

2.3.1.d. Effect of Mn and Si in the droplet

Metalloids such as Si and Mn compete with carbon to react with the available oxygen and as a result exert an influence.

Mulholland et al. [58] speculated that when silicon is present, it adsorbs on surface sites of the metal droplet, which otherwise would be occupied by carbon, and slows down the decarburization reaction. They also suggested that Si and Mn might retard the decarburization reaction through complicating the diffusion mechanisms involved. But they argued that the balance of evidence favours a site-blocking mechanism similar to sulfur. In addition, Baker et al. [69] reported that once a thin film of silica is formed around the metal droplet, decarburization was inhibited even more. They had studied droplet-gas reaction in free fall.

2.3.1.e. Effect of temperature

Temperature has a positive effect on the rate of the decarburization. Chen and Coley [63,65] reported that CO evolution rate increases with an Arrhenius type relationship by increasing temperature. However, Mulholland et al. [58] observed only a small positive effect of temperature on CO evolution rate in the range of 1450-1600 °C.

Molloseau et al. [62] studied the effect of temperature on the decarburization reaction for slags having 10-30 wt% FeO in temperature range of 1643 to 1763 K and found that there was a critical temperature for each FeO concentration at which point the rate of the

decarburization reaction increased dramatically. Although they failed to present a reason for this observation, however they postulated that surface tension of slag or metal, slag viscosity and the diffusivity of Fe^{2+} and O^{2-} ions in the slag might have contributed to the emulsification behaviour of the Fe-C-S metal droplets leading to a large increase in reaction rate with relatively small increase in temperature.

In Figure 2.23, the variations of the total moles of CO evolved (equal to the moles of FeO reduced) is plotted with respect to time, for 1.1 g metal droplets. It is seen in the figure that total CO evolved increases with increasing temperature from 1713 to 1763 K. Similar to Figure 2.16, in Figure 2.23 also it can be inferred from the sudden change in the slope of the lines that there are two distinctive reaction rates. As it is seen in this case (10 wt% FeO in slag), the initial rate varied greatly with temperature from 3.0×10^{-5} moles/s at 1713 K to 3.0×10^{-4} moles/s at 1763 K.

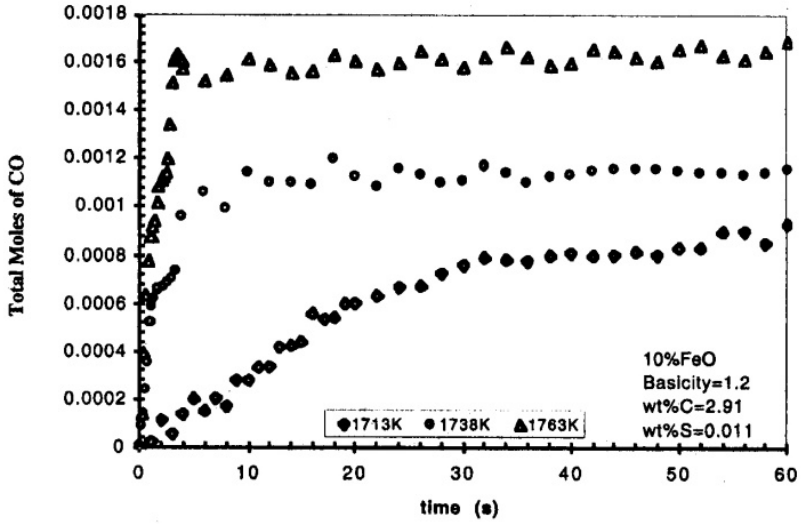

Figure 2.23 – Variations of the total moles of CO evolved with time (s) for 10 wt% FeO from 1713 to 1763 K (weight of the metal droplet = 1.1 g) [62].

As it is illustrated in Figure 2.24, an Arrhenius type relationship between temperature and reduction rate was proposed by Krishna Murthy et al. [60]. Additionally, temperature appears to have an effect on foam formation. It has been reported that due to higher slag viscosity at lower temperatures, CO bubbles take longer time to reach to the slag surface [58].

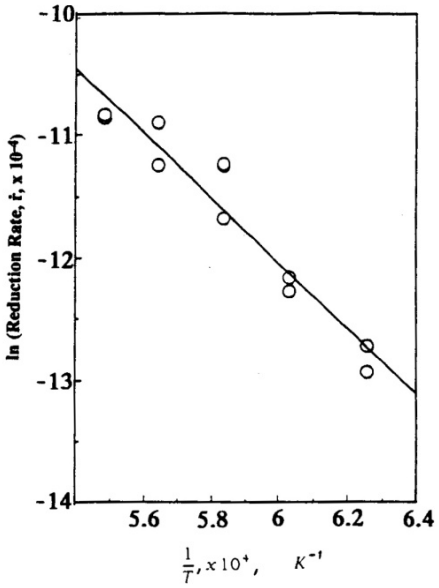

Figure 2.24 – Effect of temperature on the rate of reduction of FeO in slag [60].

2.3.1.f. Effect of metal droplet size

Krishna Murthy et al. [60] in their study of two types of droplet size of 1 and 2 g have reported that initial rate of the decarburization was independent of the droplet size and argued that only the extent to which carbon in the droplet reacted with FeO in the slag increased with decreasing droplet size.

In contrast, Chen and Coley [63,65] in their study of the decarburization rate of Fe-C-S metal droplets with an oxidizing slag using droplets with mass range of 0.5–2.5 g reported a linear increase in CO evolution rate by increasing the metal droplet mass. In Figure 2.25-a obtained from their study, it is seen that reaction rate linearly increases with droplet size. In Figure 2.25-b the effect of metal droplet size on swelling rate is

illustrated. It is seen that as expected, larger droplets have a more pronounced influence on the swelling rate. It shows that CO nucleation inside the metal droplet is more intense in larger droplets.

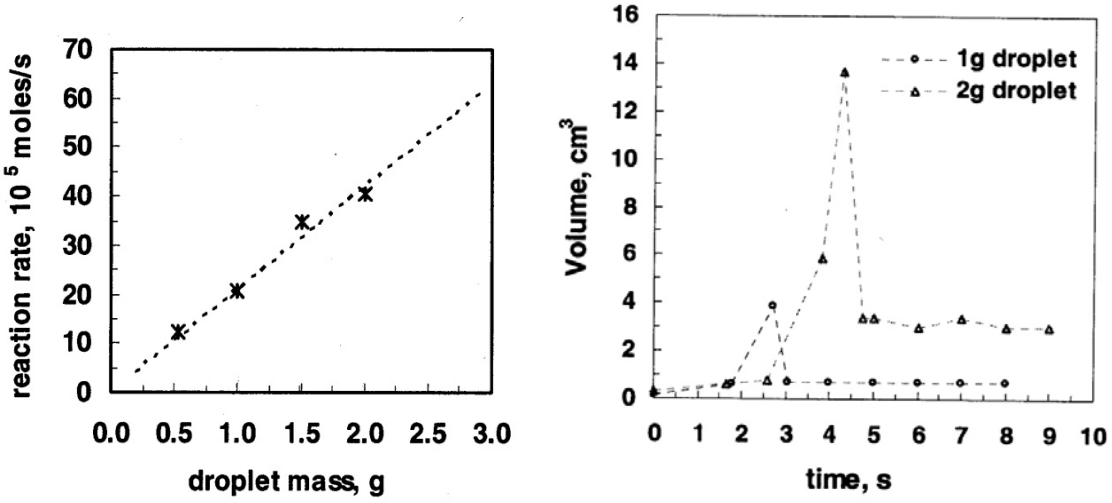

(a) (b)

Figure 2.25 – Effect of metal droplet size at 1773 K on a) CO evolution rate [63,65] and b) Swelling rate [63].

Figures 2.26 and 2.27 also support the fact that droplet size has an influence on CO evolution rate. Figure 2.26 shows the variations of the total moles of CO evolved as a function of time (s) for various mass of Fe-C-S metal droplets at 1673 K. As it is seen in the figure, there are two distinctive reaction rates for the case of larger droplets (4.6 and 5.1 g). While smaller droplets do not seem to show any change in the reduction rate over

time. Carbon and sulfur content of the metal droplet used in this study was 4.2 wt% and 0.001 wt% respectively and slag was $CaO\text{-}SiO_2\text{-}Al_2O_3$ having 7.5 wt% FeO.

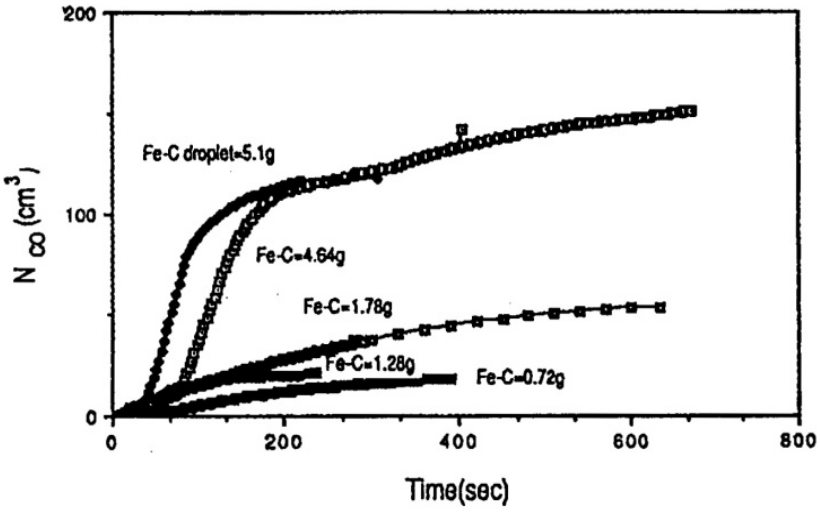

Figure 2.26 – Variations of the total moles of CO evolved as a function of time (s) for various mass Fe-C-S metal droplets at 1673 K [61].

In Figure 2.27, the relationship between the maximum CO evolution rate per unit area for two different droplet size with FeO content of the slag is illustrated. This figure shows that by increasing the FeO content of the slag as well as the metal droplet size, CO evolution rate increases.

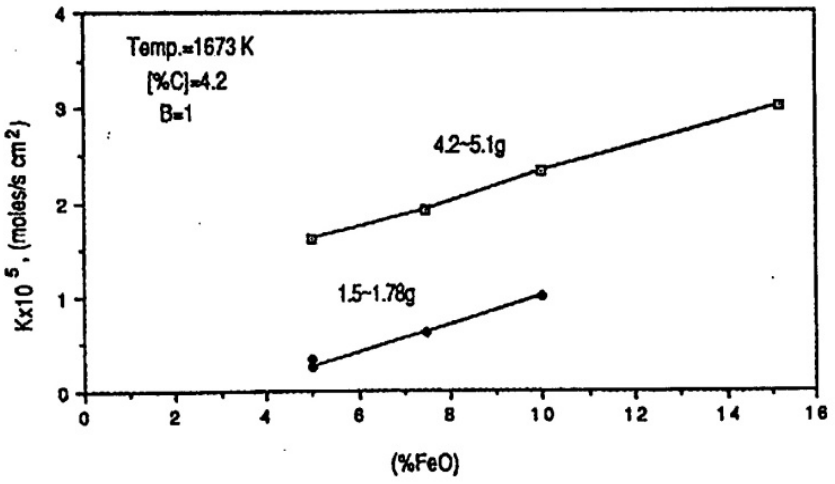

Figure 2.27 – Relationship between the maximum CO evolution rate per unit surface area for two different droplet size with FeO content of the slag [61]

It is worth mentioning that droplet size also has an influence on buoyancy effect. The buoyancy effects become more noticeable in smaller droplet sizes.

2.3.2. Droplet behaviour in slag

Kozakevitch et al. [68] were among the first scientists who employed X-ray to observe the decarburization of Fe-C droplets in contact with an oxidizing slag. They qualitatively analysed the decarburization rate by X-ray.

By using X-ray fluoroscopy, it is possible to investigate the changes in behaviour of the metal droplet in slag with time and then present the mechanisms involved in the reaction. In addition, the effect of different parameters on the rate of the decarburization reaction

can be justified by knowing the droplet behaviour in the slag. For example whether the droplet has become emulsified, has entered the foamed slag or has collapsed during the reaction all could be helpful for better understanding the reaction.

Figure 2.28, provided by Molloseau et al. [62], concisely illustrates the behaviour of Fe-C-S metal droplet in slag containing 20 wt% FeO. It is seen that after about 1 second of the time the droplet is fallen down into the molten slag, it emerges out of the slag while a foamed slag layer is simultaneously being formed due to CO evolution as a result of the decarburization reaction. Then it is seen that the droplet is quickly expanded and as it is argued possibly emulsified. The droplet size is now double its initial diameter. As reported droplet remains emulsified in the foamed slag formed until t=6 seconds at which time it starts to collapse. After that as it is seen, it recoalesces and enters the thick slag layer. Now the reaction is over and the droplet quickly falls to the bottom of the crucible. In addition, it is seen that once the reaction is over and droplet is fallen into the slag, foamed slag begins to collapse until finally disappears at about t = 30 seconds.

However, it appears that behaviour of the metal droplet in slag with low content of FeO (< 5 wt%) is much different. In this case similar to Min et al. [61], Molloseau et al. [62] also did not see any evidence that the droplet became emulsified in the slag. In addition, they reported that the droplet almost remained intact and the reaction with the slag took longer and was about 50 seconds.

X-ray technique has also been extensively employed for interfacial and surface tension studies of copper matte droplets [16,17,19-22].

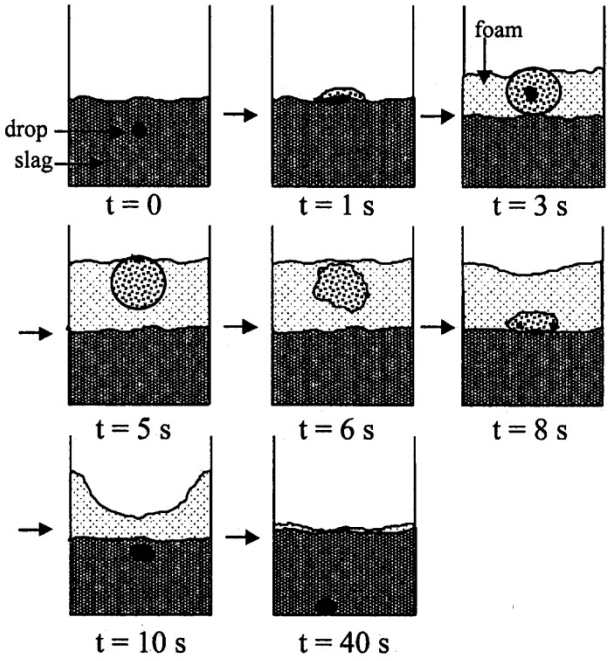

Figure 2.28 – Schematic diagram of X-ray fluoroscopy observations of the behaviour of Fe-C metal droplet in a slag containing 20 wt% FeO over time [62].

2.3.3. Oxidation kinetics of molten copper sulphide

Numerous researchers have studied oxidation kinetics of molten copper sulphide using an oxidizing gas mixture blown to the melt [6-15,67].

Jalkanen [12] studied phenomenology and the oxidation kinetics of molten cuprous sulphide and copper, using a thermal gravimetric technique. He injected a variety of oxidizing gas mixtures (air, oxygen and oxygen-nitrogen) from the top to the molten matte and investigated the effect of different variables including temperature (1150 to 1350 °C), initial sulfur content of the cuprous sulphide, gas blow rate as well as oxygen content of the blowing gas on the rate of the overall reaction.

In Figure 2.29 obtained from his work, variations of molten Cu_2S sample weight with time is demonstrated.

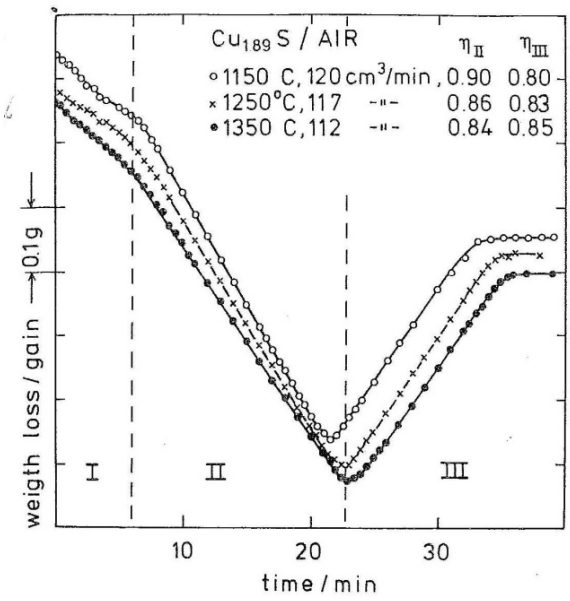

Figure 2.29 – Variations of molten Cu_2S sample weight with time [12].

In Figure 2.29, three different parts marked by sudden changes in the weight of the sample are seen. These parts represent different stages of the oxidation of molten copper sulphide (Cu_2S) to cuprous oxide (Cu_2O). Gas efficiency is also shown in this figure.

According to Jalkanen [12], the first stage corresponds to the saturation of the molten copper matte by oxygen and copper through these two reactions, respectively:

$$\frac{3}{2}\ O_2 + \underline{S} = \underline{O} + SO_2 \qquad (2.33)$$

$$O_2 + \underline{S} = SO_2 \qquad (2.34)$$

Where $\underline{S}$ and $\underline{O}$ correspond to sulfur and oxygen dissolved in the matte, respectively. The second part in Figure 2.29, represents copper sulphide reaction with oxygen adsorbed into

the melt surface and therefore sudden weight loss due to SO_2 gas evolution. The third stage corresponds to the oxidation of molten copper produced in stage two, and as a result formation of molten or solid Cu_2O, depending on the temperature. In fact, the reason for sample increased weight in third stage is copper oxide formation. As argued by Alyaser and Brimacombe [6,7], thermodynamically, copper oxide formation in copper converting is not possible unless copper sulphide is completely desulphurized and there is no copper sulphide present in the system.

Jalkanen proposed the following three potential rate-controlling mechanisms for the oxidation of molten Cu_2S matte with an oxygen-nitrogen gas mixture:

1- Mass transfer of oxygen molecules from the oxidizing gas mixtures stream on the melt surface
2- Chemical desulphurization reaction with S in Cu_2S with O_2 and formation of Cu and evolution of SO_2
3- Mass transfer of SO_2 molecules from the molten matte surface into the main gas stream

The third mechanism is composed of three interval steps that may take place:

a. Oxygen adsorption into the molten matte surface ($O_2 = 2[O]_{ads}$)
b. Formation of an intermediate activated complex such as SO ($\underline{S} + \underline{O} = \underline{SO}$)
c. Formation and adsorption of SO_2 ($\underline{O} + \underline{SO} = SO_2$)

Evaluating the experimental results obtained, Jalkanen [12] concluded that under top blow conditions with sufficient blow velocities, the overall rate was controlled by both mass transfer from the oxidizing gas mixture to the molten matte surface as well as the

chemical reaction (mixed-control). His experimental results also showed that oxidation rate of molten copper matte was temperature independent.

Alyaser and Brimacombe [6,7] similarly studied the oxidation kinetics of molten Cu_2S, under top blown conditions using oxygen/nitrogen (argon) as the oxidizing gas mixture. They studied the effect of oxygen partial pressure (0.2 to 0.78) in the system, temperature (1200 to 1300 °C), gas flow rate (1 to 4 L/min) and the bath mixing on the reaction kinetics.

They reported that the oxidation of molten Cu_2S took place in two distinct stages. In the primary stage, oxygen saturation and partial desulphurization of the single molten sulphide phase took place. Upon saturation of the melt with oxygen, the secondary stage proceeded. In this stage, reaction between sulfur, oxygen and copper ions took place and as a result, copper and SO_2 was generated.

Gas phase mass transfer of oxygen to the melt surface was found to be the rate-determining mechanism in the oxidation of molten Cu_2S. Ajersch and Toguri [8] had previously reported similar rate-controlling mechanism. Alyaser and Brimacombe [6,7] also reported that temperature had a negligible effect on the overall reaction rate in their studies.

Additionally, using X-ray, surface-tension-driven flow (the Marangoni effect) was observed by them throughout the experiments. They reported that in the X-ray images SO_2 bubbles were observed to erupt from the bath surface during the secondary stage only.

Chapter 3. Materials and experimental procedure

The experimental work in this study consisted of three major steps including: a) preparation of materials, b) performing the high-temperature experiment, and c) subsequent analyses. Droplet behaviour in the slag was analysed using X-ray fluoroscopy and reaction rate was measured using a pressure transducer and the constant volume pressure increase (CVPI) technique. In addition, chemical titration was done on synthesized slags in order to investigate the amount of Fe^{+2} and Fe^{+3} at different temperatures. Furthermore, structural analysis was performed on slag samples as well as matte/slag samples quenched from different temperatures by means of X-ray diffraction (XRD) as well as optical and scanning electron microscope, the latter equipped with an energy dispersive X-ray spectrometer (EDS).

In this chapter, the details of the materials, experimental procedure as well as the different analysis techniques employed will be discussed.

3.1. Materials

3.1.1. Matte droplet

Copper (I) sulphide (Cu_2S) is used as the matte droplet. High purity Chalcocite (99.5% purity) produced by Alfa Aesar was used in this regard. In order to study the effect of matte droplet size, pellets of copper sulphide varying in weight were produced using a

hydraulic press and die. The diameter of the pellets was 6 mm, but they varied in height and therefore had different weight. The weight of the pellets was 0.5, 0.75, 1 and 2 g.

Figure 3.1 shows two micrographs with different magnifications obtained from optical microscopy performed on Cu_2S pellets. Prior to performing the optical microscopy, the pellet was cold mounted and polished using silicon carbide polishing papers and water. In addition, no etching was applied.

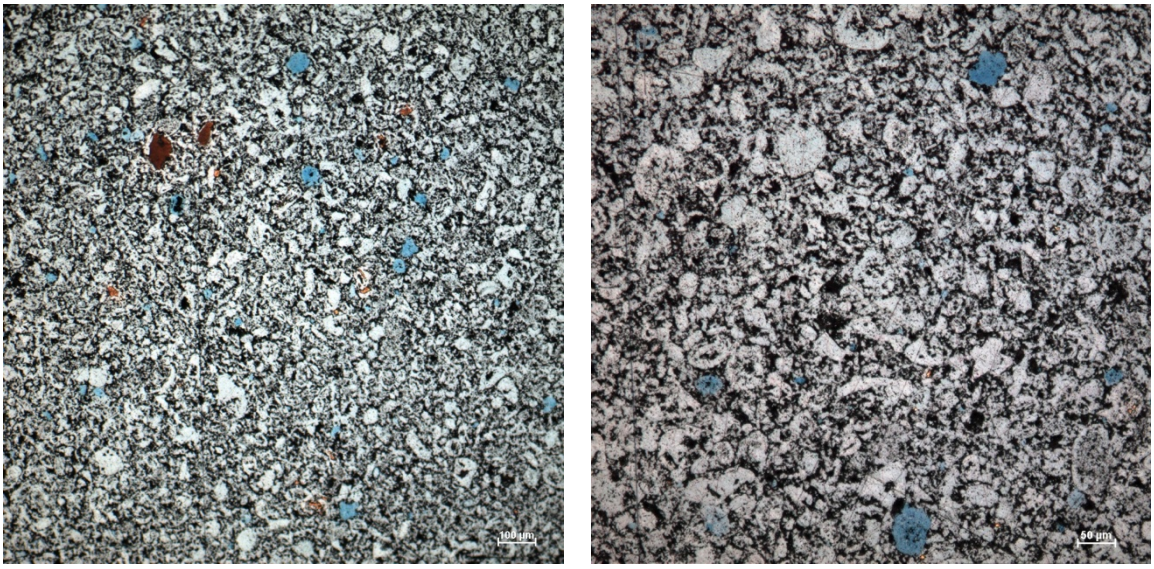

Figure 3.1 – Micrographs obtained from optical microscopy performed on Cu_2S pellets produced at room temperature by employing a hydraulic press. Copper sulphide pellet was cold mounted, polished using water and no etching was applied before analyzing the structure under the microscope.

In Table 3.1, important information about copper sulphide is presented. Theoretically, the sulfur content of Cu_2S is about 20.15 wt% and its melting point is about 1130 °C. The pellets would easily melt and form a droplet once exposed to high temperatures used in this study and then would fall into the slag at which point reaction will start to happen.

Table 3.1 – Some of the important characteristics of copper sulphide (Cu_2S) [70,71].

Crystal Structure	Monoclinic – Hexagonal Closed Packed (above 104 °C)	Density (g/cm^3)	5.6 at 27°C
Stoichiometric Range	$Cu_{1.997}S$ – $Cu_{2.000}S$	Melting Point (°C)	1130
Molar Weight (g/mole)	159.16 at 27 °C	Solubility in Water	Insoluble
Color	Bluish – Black	sulfur content (wt%)	20.15

3.1.2. Synthetic slag

Synthetic silica-saturated Fayalite ($2FeO - SiO_2$) was used in this study as slag. High purity hematite (Fe_2O_3), silica (SiO_2) and iron (Fe) powders were used in this regard. Hematite and silica powders with 99.5% purity were received from Alfa Aesar. Hematite and silica particles were finer than 5 and 37 microns, respectively. Very fine and highly pure iron powder (99% purity) produced by BDH Laboratory Supplies was also used.

Purity of the powders was confirmed by X-ray Diffraction analysis (XRD) as shown in Figure 3.2.

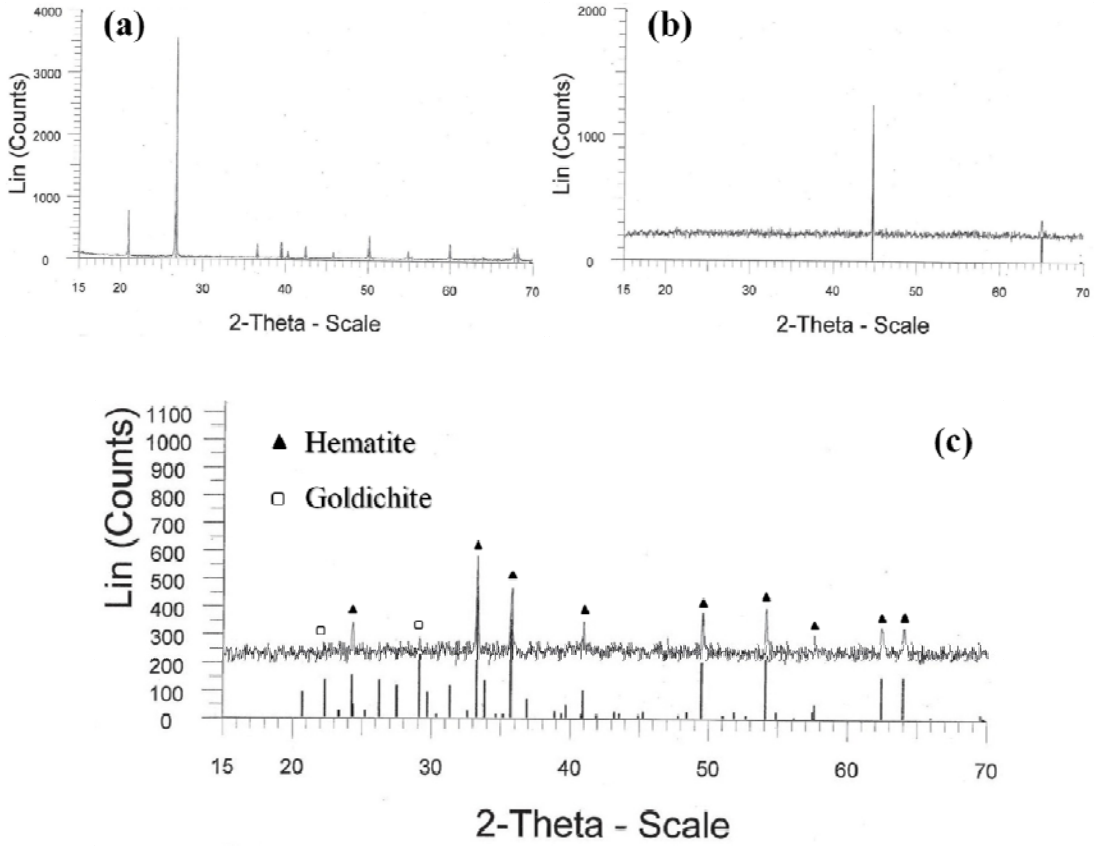

Figure 3.2 – X-ray diffraction patterns of silica (a), iron (b) and hematite (c) confirming the purity of the powders used.

As it can be understood from Figure 3.2, in the XRD patterns of silica and iron powders, no detectable irrelevant peaks are seen. But in the XRD pattern obtained from the hematite powder, besides the significant hematite peaks, some low-intensity peaks

corresponding to goldichite ($KFe + 3(SO_4)_2 \cdot 4H_2O$) are seen. However since the amount of impurity is very low (less than 0.5% according to the producer) and the structural water associated with it evaporates during furnace heat-up, it is believed that it would not have an impact on the experiments and the observations.

The powder mixture of fayalite slag was prepared manually by adding Fe, SiO_2 and Fe_2O_3 powders with respective ratios of 1:2:3.6. In order to make sure that the powder particles have been well distributed, the powder mixture was then mechanically mixed using a planetary ball mill for 50 seconds.

It is to be noted that in the initial stages of the research, fayalite slag was first tried to be produced by mixing stoichiometric amounts of high-purity FeO and SiO_2. However, it was later realized during the high-temperature experiments that segregation happens and thus it was decided that fayalite slag be produced by putting a crucible filled with the Fe, SiO_2 and Fe_2O_3 powder mixture with the previously mentioned specific ratio, at high temperatures. Alumina crucibles were also preferred compared to fused silica and zirconia crucibles, the former because of its reaction with FeO and therefore spinel formation in high-temperatures and the latter due to its X-ray absorption properties. Further details regarding these issues are mentioned in section 3.3.

In Figure 3.3, optical microscopy image obtained from the slag powder mixture after mechanical mixing is presented. Hematite, silica and iron particles are seen in the micrograph as areas with red, white and gray color, respectively. In addition, it appears

that some agglomerates of hematite and iron powders are formed probably due to intense mixing by mechanical ball mill.

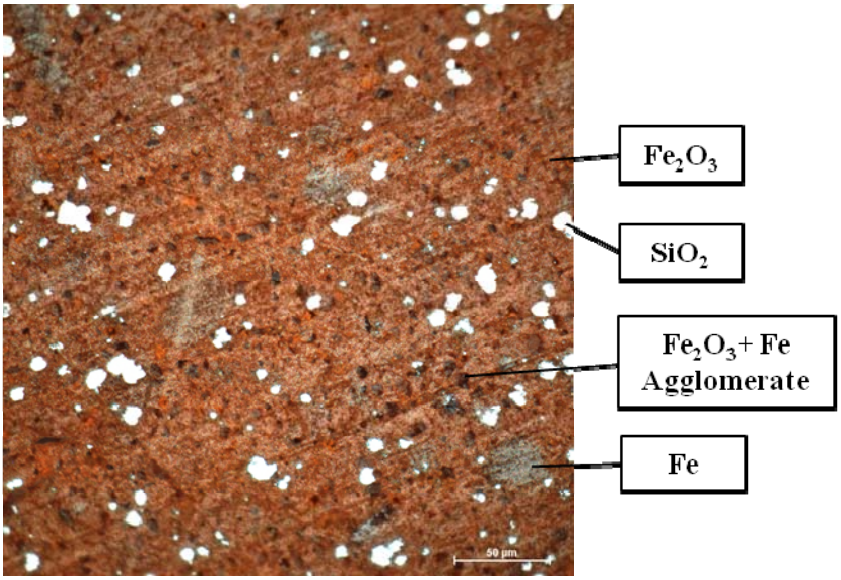

Figure 3.3 – Optical microscopy image of the slag powder mixture before doing the experiments. Hematite, iron and silica particles as well as hematite and iron agglomerates are shown in this figure. The sample was cold mounted, polished using water and no etching was applied.

3.2. Experimental set-up

The experimental setup employed in this study was the same as that of two former McMaster University's graduate students in Dr. Coley's group; Chen [65] and Pomeroy [72]. The experimental setup consisted mainly of three units of a) furnace, b) X-ray fluoroscopy apparatus and c) pressure transducer [Figure. 3.4]. The details of each unit will be explained in detail below.

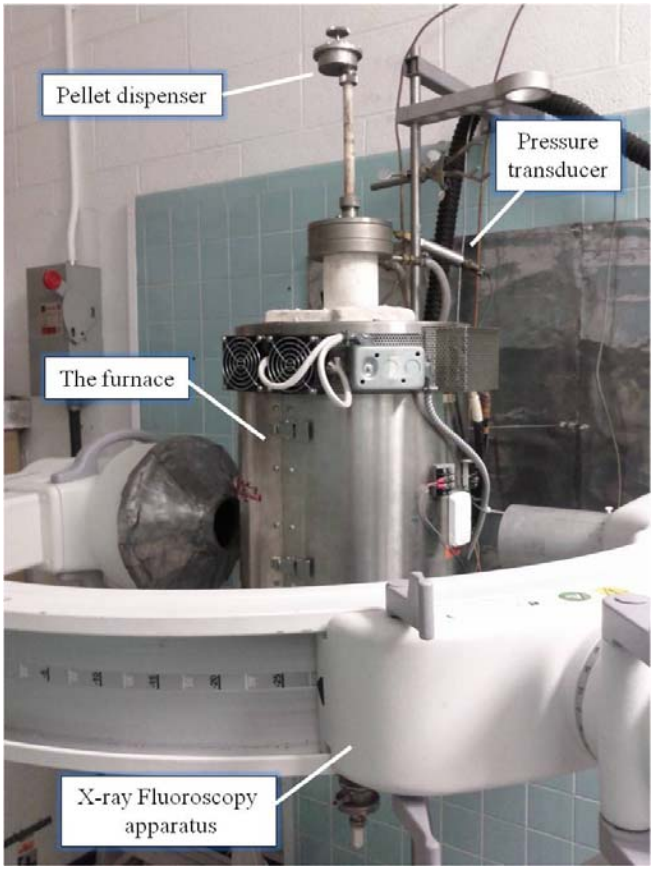

Figure 3.4 – A picture of the experimental set up. The furnace, X-ray fluoroscopy apparatus, the pressure transducer as well as the pellet dispenser are shown here.

3.2.1. The furnace

A furnace was used to perform the high-temperature experiments. Two rectangular holes were cut onto the stainless steel shell of the furnace so that X-rays could pass with minimum absorption to the wall and to achieve higher image quality for analysing the droplet behaviour. The furnace was heated by Kanthal Super 1800 molybdenum disilicide ($MoSi_2$) elements and they were obtained from Sandvik Heating Technology. An alumina working tube (I.D = 79.4 mm, O.D = 88.9 mm, Height = 762 mm) obtained from McDanel Advanced Ceramics, LLC was installed inside the furnace. The two ends of the working tube were completely sealed using an O-ring as well as stainless steel end caps, which were water-cooled throughout the experiment. The sealed alumina tube worked as a container in which pressure variations during the experiments were measured.

For a couple of initial experiments, fused silica crucible (cylindrical; OD = 45mm, height = 90mm) obtained from Leco Corporation was used. But for the experiments with higher temperatures, which ended up showing meaningful data, alumina crucible (cylindrical; OD = 35mm, height = 64mm and/or OD = 40 mm, height = 60 mm) obtained from either McDanel Advanced Ceramics, LLC, Anderman Ceramics or CoorsTek Advanced Technical Ceramics was used in which molten fayalite slag was produced and the reaction between the matte droplet and the slag took place.

An alumina dispensing tube (I.D = 11mm, O.D = 17mm) was placed inside the working tube, about 90 mm above the alumina crucible. There was a 4.7mm diameter hole at the base of the dispensing (delivery) tube, which allowed the pellet to melt prior to entering

the slag. Because of the size of the hole, usually only pellets smaller than 0.75 g fell in one piece and the larger pellets fell in the form of more than one drop (usually two pieces).

Temperature control in the furnace was done using a programmable EUROTHERM Power Controller from Neal Systems Inc. Furnace had a type B thermocouple (Pt-6%Rh vs. Pt-30%Rh) which was was inserted through small holes made to one side of the furnace and then was attached to a temperature reader installed on the furnace control box. The reader showed the highest temperature (hot zone) just outside the alumina working tube. Because of the structure of the furnace (i.e. placement of crucible inside an alumina working tube), obviously the real temperature at which experiments are performed is different than what the furnace thermocouple shows, so temperature calibration is needed which is to be discussed later in this chapter.

Figure 3.5 schematically illustrates the arrangement of different parts of the furnace as well as the location where crucible sits inside the furnace. The crucible was first placed on a graphite disc on an alumina support tube, but to prevent any possible reaction between the oxidizing slag and the graphite, a thin alumina disc obtained from Ceramic Solutions was used for all the next experiments and the previously performed experiments were also repeated. As it is seen in Figure 3.5., the crucible and the disc were placed on an alumina support tube.

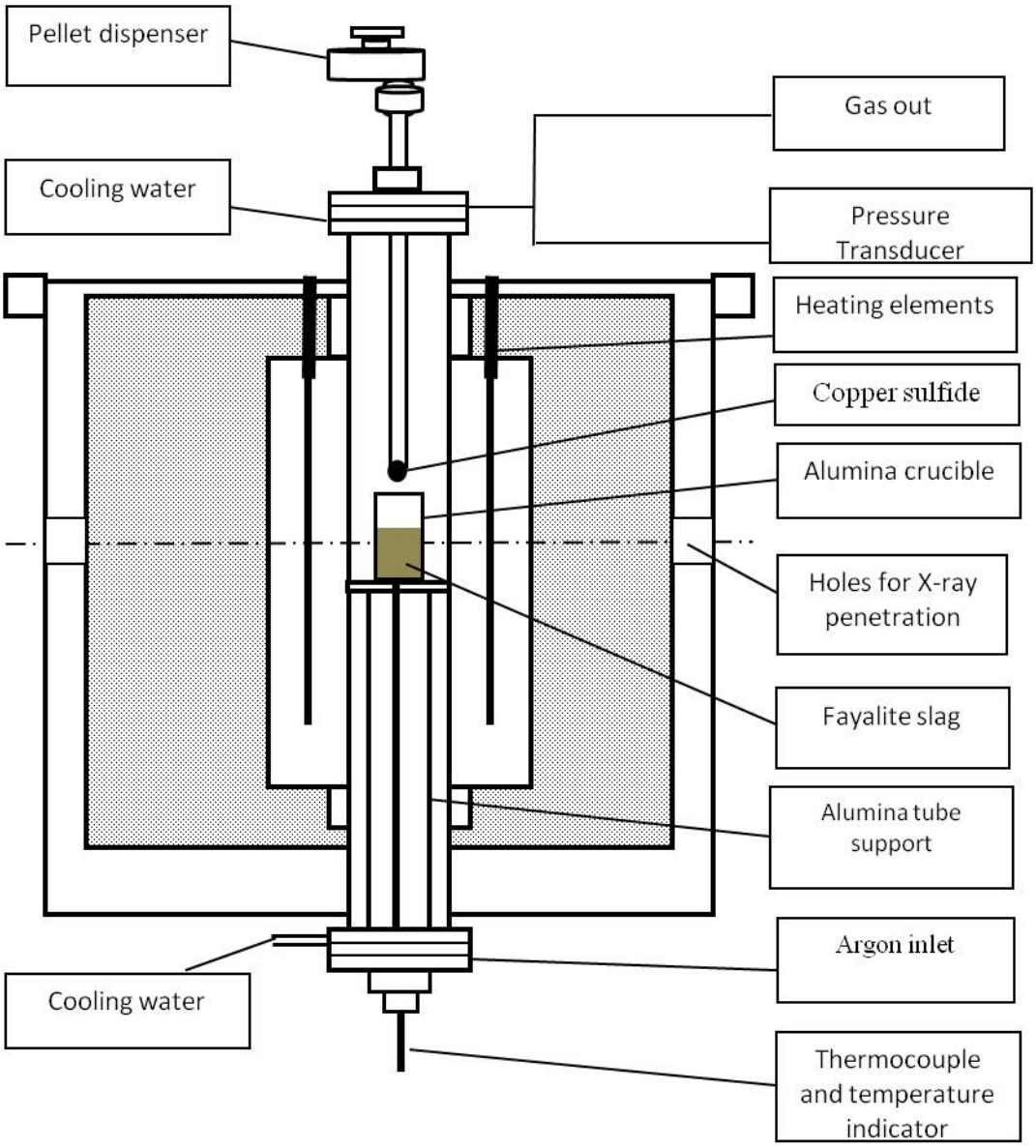

Figure 3.5 – Schematic diagram of the experimental setup, showing the different parts of the furnace, location of the crucible, the delivery tube as well as the thermocouple.

3.2.2. X-ray fluoroscopy

The X-ray fluoroscopy apparatus (GE OEC Medical Systems, Inc.) consisted of an OEC Workstation and movable C-arms. The workstation includes a touch-screen, workstation keyboard and an infrared remote control. The X-ray image was obtained on a 230 mm diameter round fluorescent screen located on the C-arms and was displayed on the screen. The X-ray images were recorded on a computer for further analysis.

3.2.3. Pressure transducer

In this study, a very low pressure transducer with the maximum measurable range of 14 kPa of differential pressure (FLW Southeast, Inc, 157C-W050NR) and sensitivity of 3.03 Pa was used in order to measure any variations in the pressure inside the furnace as the desulphurization experiment (reaction [3.1]) proceeds and thus as gas is released. The set of measurements on the pressure changes consist of a sensor (pressure transducer) and a data acquisition system (RS232 Interface). The obtained data from the transducer were then accurately recorded for further analysis to a computer using a special software. The data recording interval was set at 1 Hz.

$$Cu_2S + 2\underline{O} = 2Cu + SO_2 \qquad (3.1)$$

The output data of the pressure transducer is expressed in terms of psi, which needs to be converted to the molar amount of SO_2 released.

From the calculation of the furnace volume (about 4.1×10^{-3} m^3) and by considering reaction (3.1), it was estimated that the pressure increase due to SO_2 released from

reaction of a 1-g Cu_2S droplet at 1475 °C (1748 K) with slag would be about 22.4 kPa. As it is seen the pressure increase even for the 1 g droplet is well above the 14 kPa capacity of the transducer. In addition, theoretically, the gas released for the 2 g droplet would be expected to be larger than the maximum capacity of the transducer and at first, it appeared that a larger capacity transducer should be used. However, the important point here is that not the whole droplet reacts with the slag. In fact, the results showed that the pressure increase even in the experiments with the 2 g droplet stayed well below the capacity of the transducer. The data shown in the next chapter are more indicative of the reality that only a portion of the droplet reacts and thus this type of pressure transducer was appropriate for this study.

3.3. The experimental procedure

As it was mentioned earlier in section 3.1.2, in the initial stages of the research, it was first tried to produce the fayalite slag by mixing stoichiometric amounts of high-purity FeO and SiO_2. However, it was later realized in the X-ray photos taken during the high-temperature experiments that segregation happens in that type of slag; where higher density species settle at the bottom of the crucible (Figure 3.6-left). As it is seen in the figure, for the case of $2FeO – SiO_2$ mixture at 1250 °C, which is the common temperature mentioned in the literature, slag was obtained only partially molten and a sharp segregation has happened. In this experiment, a silica crucible was used.

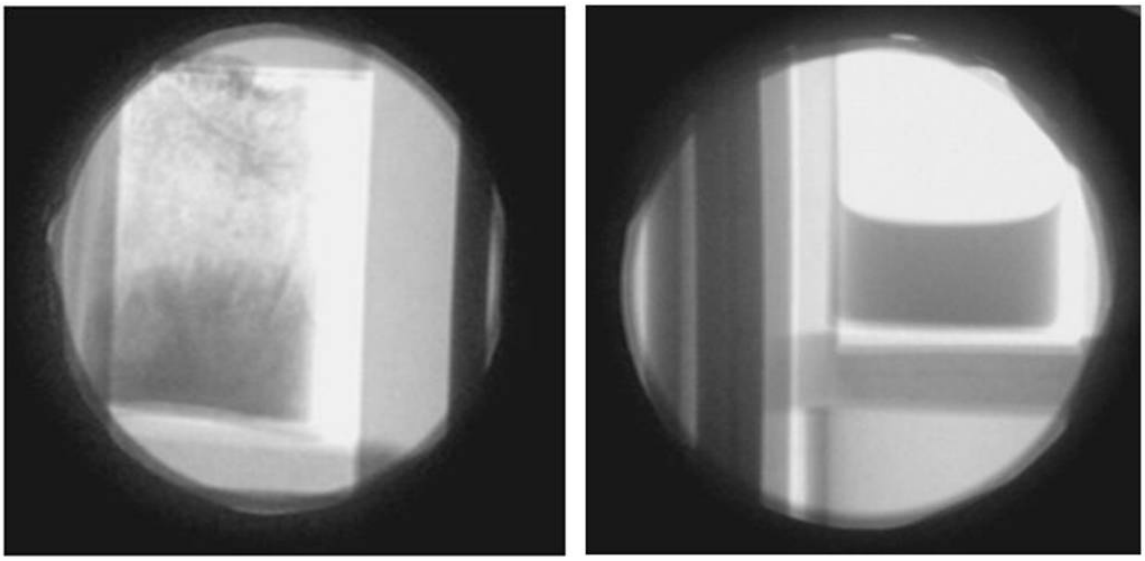

Figure 3.6 – Two different slags. Left, shows that segregation has happened and the slag is not completely molten. Right, a completely molten and homogeneous slag is seen. The meniscus formation is also clear.

So, to obtain a homogeneous and completely molten slag, temperature was increased up to 1300 °C. Even in this temperature, no completely molten slag was obtained. Further increase in the temperature was not feasible as the silica crucible was not able to withstand the heat. Consequently, we had to change the crucible. Zirconia and alumina crucibles were the options available. But, since zirconia is an X-ray absorbent and as a result undermines the quality of the X-ray pictures taken during the high-temperature experiments for analysis of droplet behavior, we had to use crucibles made of alumina.

However since alumina and FeO together form spinel ($FeAl_2O_4$) in elevated temperature [73], it was not possible to use FeO-SiO_2 powder mixture in the experiments. Therefore, it was decided that slag be produced through mixing Fe_2O_3, SiO_2 and Fe powders according

to the details mentioned earlier. No segregation was observed in the slag produced with this procedure.

So in this study, 33 g of the powder mixture prepared by mixing of Fe, SiO_2 and Fe_2O_3 powders according to respective ratios of 1:2:3.6 were charged into an alumina crucible each time before the furnace was turned on. It is to be noted that Fe/SiO_2 ratio in the slag was purposely chosen to be about 1.76 in this study, in order to be close to silica-saturated fayalite slags present in matte smelting furnaces in industry.

The crucible was then placed on a thin alumina disc and was subsequently placed on an alumina support tube inside the furnace. In addition, copper sulphide pellet was inserted into the pellet dispenser. After closing the two-end of the furnace and getting furnace completely sealed and making sure that there is no leak in the furnace (using the pressure transducer), the argon valve was opened in order to perform the experiment in an inert atmosphere and also to prevent any unwanted oxidation of either the copper sulphide or the slag before the experiment. Highly pure argon employed was even more purified before entering the furnace by passing through a column of "Drierite". Argon gas was stopped during the experiments

In different experiments, the furnace was set at a specific high temperature ranging from 1400 to 1475 °C. The average rate of the temperature increase was about 1.5 °C/s.

Once the desired temperature was reached, the furnace was sealed again by injecting specific amounts of argon to the furnace and tracking the pressure increase inside the furnace using the pressure transducer. Details of pressure and temperature calibration are

to be discussed later in this chapter. After the pressure calibration is done, copper sulphide pellet is released. Quickly after that, recording of the data read by the pressure transducer as well as videos captured by the X-ray fluoroscopy are recorded on a computer for further analysis.

After pellet release, it falls and stays at the end of the narrow alumina delivery tube until it melts and falls as a drop. Depending on the temperature at which the experiments are done, this staying time differs from 20 seconds at lower temperatures and decreases at higher temperatures. Due to the size of the hole at the end of the delivery tube, if the pellet is larger than 1 g, it usually falls in the slag as more than one drop. When the droplet falls, there is an incubation time after which the reaction starts to happen and the pressure inside the furnace goes up, until becomes stable.

The rate of the pressure increase inside the furnace will be used to study the effect of temperature (1400, 1425, 1450 and 1475 °C) and droplet size (0.5, 0.75, 1.0 and 2.0 gr.) on the desulphurization reaction rate and the X-ray photos taken will be evaluated to study the droplet behaviour inside the oxidizing slag and any possible halo formation.

3.4. Calibration

3.4.1. Temperature calibration

As briefly explained earlier in this chapter, obviously, there is a difference in the temperature the furnace thermocouple shows and what the real temperature is. Therefore, the temperature calibration was done because of the following two reasons:

- To obtain the temperature profile of the furnace and to identify the location of the hot zone
- To find the real temperature at which the crucible is and to know the difference between the real temperature and what the furnace thermocouple is showing

In order to perform the temperature calibration on the furnace, a thermocouple type B (Pt-6%Rh vs. Pt-30%Rh) was employed. To protect the thermocouple wire from damage and to be able to do the temperature measurements accurately, the wire was placed inside a round double bore extrusion made of high purity alumina and the extension itself was then fitted into a single bore alumina tube. The wire thermocouple and the tubes were obtained from Omega Engineering Inc. and McDanel Advanced Ceramics Technologies, LLC, respectively.

As it is seen in Figure 3.5, the thermocouple was inserted from the bottom of the furnace and was located close to the sample to find the real temperature at which the experiments are being done. The other end of the thermocouple was attached to a voltmeter, which showed the potential difference between the two wires. This number was then converted to temperature using the corresponding reference table for thermocouple type B. This process of obtaining the real temperature was done for every centimetre of the vertical tube inside the furnace.

In Figure 3.7, temperature profile of the furnace is illustrated for three different temperatures. As it is seen a hot zone of 60 mm long was identified in which the temperature varied within ±1 $^{\circ}$C. A schematic illustration of the location where the

crucible sits in the hot zone of the furnace has also been presented. The temperature, at which the controller was set, was then adjusted according to the result obtained from these calibrations in order to perform the experiments at the exact temperature.

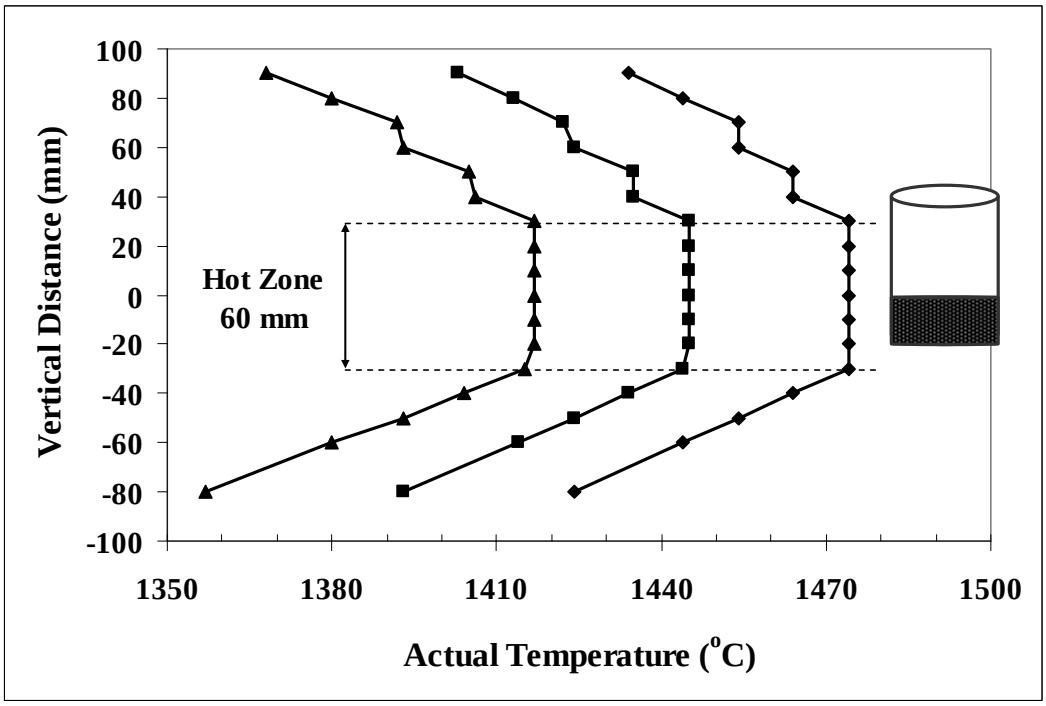

Figure 3.7 – The temperature profile inside the furnace for temperature controller set at T=1530, 1505 and 1480°C. A schematic photo of the location of the crucible in the furnace with molten slag is also presented.

3.4.2. Pressure calibration

In this study constant volume pressure increase (CVPI) technique was employed to measure the reaction rate. This is because as the reaction proceeds (reaction [3.1]), more and more amounts of gas is released and as the volume and the temperature is constant in the furnace, pressure inside the furnace increases. Therefore, as the data obtained from the pressure transducer are going to be used for reaction rate measurements, it is vital to calibrate the pressure data. In order to do that, when the furnace was at the specific temperature of the experiment and before starting the experiment (releasing the pellet), specific amounts of high-purity argon gas was injected into the furnace and the resulting pressure increase detected by the pressure transducer was carefully recorded.

As it is seen in Figure 3.8, pressure almost linearly increases with injecting the gas inside the furnace. The first injection was done after the first minute of the starting point of recording the data and the injection interval was 2 minutes. Every time, 5 ml of argon was injected.

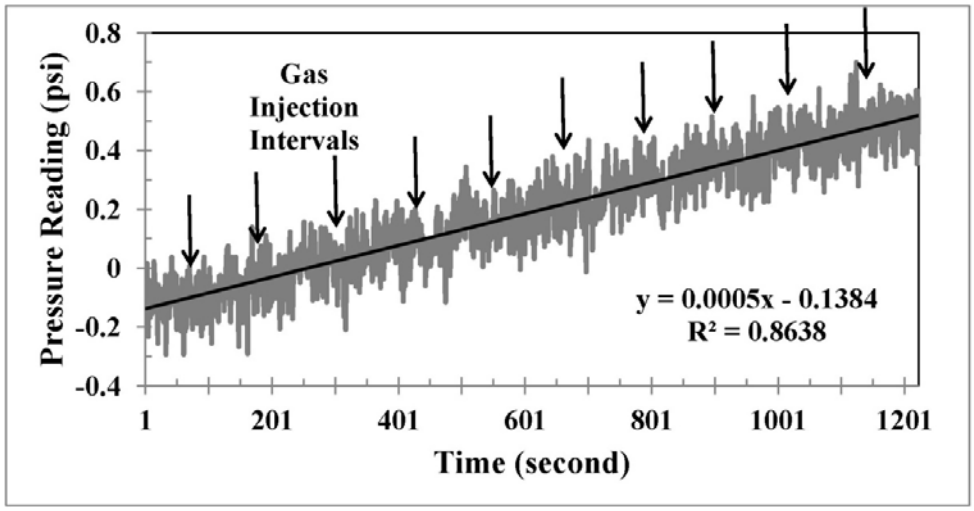

Figure 3.8 – A typical example of how the pressure increased by injecting specific amounts (5 ml) of argon in specific intervals (2 min). T is 1475 °C and the first injection happened at t = 1 min.

This correlation between pressure increase and the amount of injected gas was used later in order to calculated the amount of SO_2 released during the experiment and then for the reaction rate analysis.

Since different parameters (e.g. temperature, the size of the alumina support tube, the size of the crucible, etc.) affect the amount of pressure increase, pressure calibration was done prior to every experiment and corresponding data were used for reaction rate measurements of that specific experiment.

3.5. Analysis

Different kinds of analysis were done in this study. Droplet behaviour was carefully studied using the X-ray fluoroscopy apparatus in order to identify any possible phenomena (such as droplet swelling, halo formation around the droplet or variation in size of the droplet over time) that might occur during the experiments.

Structural analysis was performed on the slag/matte droplet samples. To study the slag-gas-matte interface, slag was quenched in air. The quenching was done exactly at 2 minutes after the droplet fist touched the slag following the free-fall. Afterwards, the crucible was cut, slag was cold mounted and polished (Struers Multidoser Rotocom) and the interface was then analysed using an optical microscope (Nikon LV100, NIS Elements).

Elemental analysis of different points in slag as wells as inside the matte was investigated, employing the energy dispersive X-ray spectroscopy (EDS) technique. The analysis was done on the quenched samples using one of the scanning electron microscopes (JEOL 6610LV) available in the Canadian Centre for Electron Microscopy (CCEM). The SEM was equipped with the necessary energy dispersive X-ray spectrometer (EDS or as is sometimes called EDS). The preparation steps taken prior to using the microscope included mounting and polishing the samples, and then applying a sputtered coating layer of graphite with an estimated thickness of 15-20 nm as well as making a conductive path made of silver on the samples. The software employed in order

to extract and analyze the data was called "The Microanalysis Suit, Oxford Instruments INCA 4.15".

Chemical titration test was performed on the slag samples obtained at different temperatures in order to measure the Fe^{+2}/Fe^{+3} ratio in the slag. The details of the titration test is presented in Appendix 1.

As briefly stated before, reaction rate measurements were also done in this study using the data obtained from the pressure transducer after the droplet fell into the slag. Details of the pressure calibration were mentioned earlier in section 3.4.2. Reaction rate measurements in this study are based on CVPI technique, which itself is based on the simple thermodynamic fact that when both temperature and volume of the vessel are constant, the pressure inside the vessel increases linearly with an increase in the amount of gas. In this study, as the amount of SO_2 gas released in the furnace increases because of reaction (3.1), the pressure increases. Thus, the data obtained from the pressure transducer was converted to the corresponding volume (using the data obtained from the pressure calibration) and then the volume of gas was converted to mole (considering SO_2 behaves as an ideal gas) and eventually graphs showing variations of SO_2 mole released over time were drawn for every experiment.

Chapter 4. Results and discussion

4.1. X-ray fluoroscopy observations

Using an X-ray fluoroscopy device, different phenomena happening during the high-temperature experiments were recorded as videos. Pictures were then extracted from the videos and are presented in this chapter. In order to make sure that all the phenomena happening during the experiments were closely monitored and no important event was missed, recordings were made practically throughout the experiments (i.e. from a few seconds before the copper sulphide droplet was released until all the ongoing phenomena ceased).

In Figure 4.1, X-ray photos related to the experiment done using a Cu_2S droplet size of 0.75 g at 1475 °C are presented. These photos show the general sequence of the events. In photo (a) in this figure, which was captured a few seconds prior to the droplet release, a completely molten and homogeneous slag (known from the similar colour contrast everywhere in the slag) can be seen. In addition, meniscus formation is easily recognizable not only in this photo but in all the captured photos. It indicates that the synthesized slag is indeed in a molten state.

Photo (b) was recorded after the droplet was released exactly at the time when it touched the slag for the first time (t=0). Note the difference in contrast between the slag and the droplet at top. It should be noted that depending on the temperature at which the

experiment was being done, it took between 11 to 23 seconds for the droplet to enter the slag from the time it was released from the droplet dispenser.

Photo (c) was captured three seconds after photo (b) (t=3 seconds). It is seen that in this experiment, the droplet has broken into two portions. In this photo, the first portion is seen at the bottom of the crucible, while the second portion has just touched the slag and is at top. No droplet swelling is observable. Instead it appears that a very thin gas halo is formed surrounding the portion of the droplet immersed in the slag. This halo formation is more distinguishable in next photos which were taken at later times, especially in photo (e) which was taken at t=5 seconds when the two portions of the droplet have joined together at the bottom of the crucible.

In photo (d) captured at t=4 seconds, the second portion of the droplet is seen leaving the top of the slag and is about to join the first portion at the bottom.

In photo (e) obtained at roughly t=5 seconds, the second portion of the droplet has joined the first and consequently the whole droplet is seen as one piece which is located at the bottom of the crucible. A gas halo can also be seen surrounding the droplet. In addition, as it is seen, the shape of the droplet is ellipsoidal rather than spherical. The shape of the droplet at the bottom of the crucible is governed by gravity force and wetting phenomena, which depend on slag properties (slag composition and viscosity), temperature and type of the crucible used.

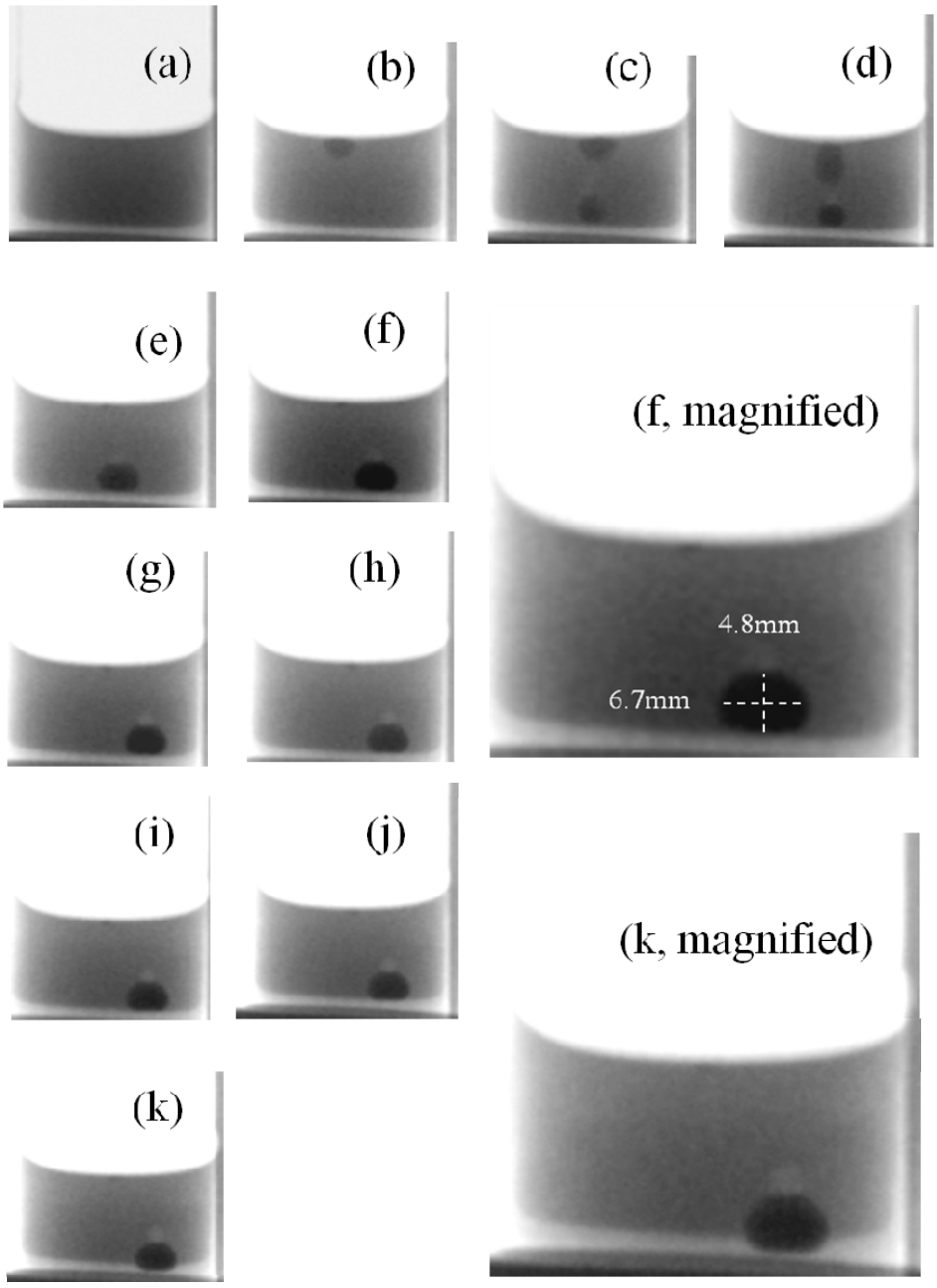

Figure 4.1 – X-ray fluoroscopy photos extracted from movies captured during the experiment conducted using a Cu_2S droplet size of 0.75 g at 1475 °C. Each photo is captured at different time: (a) a few seconds before the droplet release, (b) exactly when the droplet touched the slag for the first time (t=0), (c) t=3 seconds, (d) t=4 seconds, (e) t=5 seconds, (f) t=6 seconds, (g) t=10 seconds, (h) t=20 seconds, (i) t=60 seconds, (j) t=360 seconds, (k) t=2360 seconds. Two magnified photos correspond to photos f and k.

Photo (f) is captured at t=6 seconds. An ellipsoidal droplet can be seen at the bottom of the crucible. The size of the droplet was carefully measured and is illustrated in a magnified image beside photo (f). Knowing the crucible diameter, the size of the droplet was estimated to be 6.7 mm by 4.8 mm. Similarly, the gas halo is also seen in this photo.

More photos captured at later times are presented in Figure 4.1. Slight droplet movement is seen over time. Furthermore, it appears that a small dome-like gas area is formed at the top of the droplet especially in later times. This finding was supported by micrographs obtained from both optical and scanning electron microscopes, which are to be presented later in this chapter. In the movies captured using X-ray fluoroscopy during the experiments, it appeared that gas molecules formed on droplet surface, which led to gas halo formation around the droplet. Gas halo almost instantly formed around the droplet as it touched the slag. Afterwards, it appeared that gas molecules continued to accumulate on the droplet surface but with a much lower rate. Since the gas density is much lower than slag and copper sulphide (matte) density, the gas molecules tend to gradually move upward and consequently form a dome-like area at the top of the droplet. It was seen that this dome-like gaseous area (bubble) was gradually growing over time to a point at which the dome was detached from the droplet and quickly went to the top of the slag and was added to the furnace atmosphere.

Gas halo formation, the formation of a dome-like bubble at the top of the droplet as well as detachment of the bubble from the droplet joining the furnace atmosphere, was clearly observable and especially significant in experiments performed at higher temperatures

and using larger droplets. In fact, dome-like bubbles were only observed in experiments with droplets with mass equal to 0.75 g or larger.

In later times no major difference is seen in the photos and this is true even in photo (k), which is captured at t=2360 seconds. This indicates that no major phenomena are happening. A magnified version of that photo is presented exactly besides photo (k). In that large photo, droplet in slag and the gas halo surrounding the droplet is clearly seen and similar to previous observations, no swelling could be observed.

As seen in Figure 4.1, the 0.75 g droplet used in that experiment separated into two pieces. This phenomenon usually happened in every experiment that was done using droplets with size equal to 0.75 g or larger. However, the two portions of the droplet usually joined each other right after the second portion entered the slag, in cases when 0.75 and 1 g droplets were used. This did not happen when 2 g droplets were used. For some reasons, the two portions did not join. An example of this phenomenon is shown in Figure 4.2. In some rare cases when a 2 g droplet was used, it fell in 3 pieces. These experiments were repeated. However, no 2 g droplet fell in only 1 piece.

In Figure 4.2 related to experiment performed at 1475 °C and using a 2 g droplet, it is seen that the droplet has fallen in two pieces. The second piece entered the slag right after the first piece; however, the two pieces did not join. From the photos, the size of the two copper sulphide pieces in 2 g experiments were measured to be roughly about 2/3 and 1/3 of the total size (mass) of the droplet. This finding was later used to modify droplet surface area measurements.

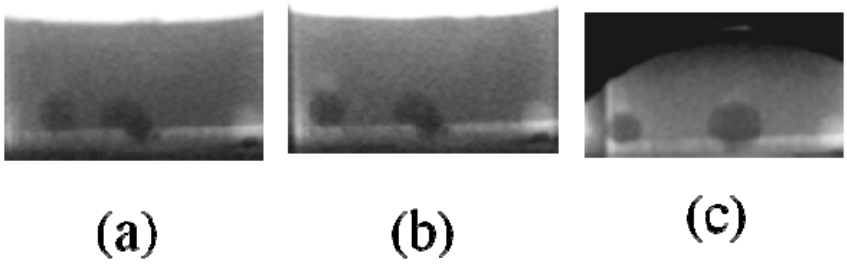

Figure 4.2 – X-ray fluoroscopy photos extracted from movies captured during the experiment conducted using a Cu_2S droplet size of 2 g at 1475 °C. Droplet fell in two portions (size of the second portion being twice as large as the first). Each photo is captured at different time: (a) exactly at the time second portion of the droplet fell, (b) t=1 seconds after the second portion touched the slag and (c) t=5.

The relatively small size of the hole at the end of the droplet delivery tube caused droplets larger than 0.75 g to fall in more than one piece. The hole had an optimum size and it was not possible to increase its size. Therefore, the issue with larger droplets falling in two pieces rather than the expected one piece was not preventable.

Finally, it should be emphasized that after close monitoring and repeated analysis of the recorded movies, no droplet swelling or white-contrast area inside the droplet, which might be an indication of formation of gas molecules, was observed in the experiments.

4.2. Slag/matte reaction

The desulphurization reaction between copper matte (copper sulphide) and oxidizing slag (fayalite) can be simply shown as:

$$\underline{S} + 2\underline{O} = SO_2\,(gas) \qquad (4.1)$$

Where $\underline{S}$ and $\underline{O}$ are sulfur and oxygen dissolved in the matte and the slag, respectively. As the desulphurization reaction proceeds in high-temperature, sulfur inside the matte reacts with oxygen from the slag and then a gaseous product is formed. If the experiment is performed in a sealed medium, the produced gas will cause an increase in pressure inside the vial. This is the basic philosophy behind the constant volume pressure increase (CVPI) technique, which was used here by employing a pressure transducer attached to the furnace in order to study the variation in gas evolution rate.

In this study, the effect of droplet mass as well as temperature on gas evolution rate was investigated, while Fe/SiO_2 ratio (1.76) in the slag and its oxidizing capacity (Fe^{3+}/Fe^{2+}) were constant.

4.2.1. Rate measurements

The pressure transducer, which was attached to the furnace, gave instant pressure variations during the high-temperature experiments. An example of the obtained results is presented in Figure 4.3. In this figure, which presents data from an experiment conducted at 1475°C using a 1 g copper sulphide droplet, the time at which the droplet was released

from the pellet dispenser as well as the time when the droplet touched the slag for the first time is illustrated. At this temperature, it took about 8 to12 seconds for the pellet to melt and fall. After the droplet entered the slag, a sudden increase in pressure was detected. This increase in pressure indicated that gas evolution has happened and by measuring the rate of increase, one can know the initial gas evolution rate.

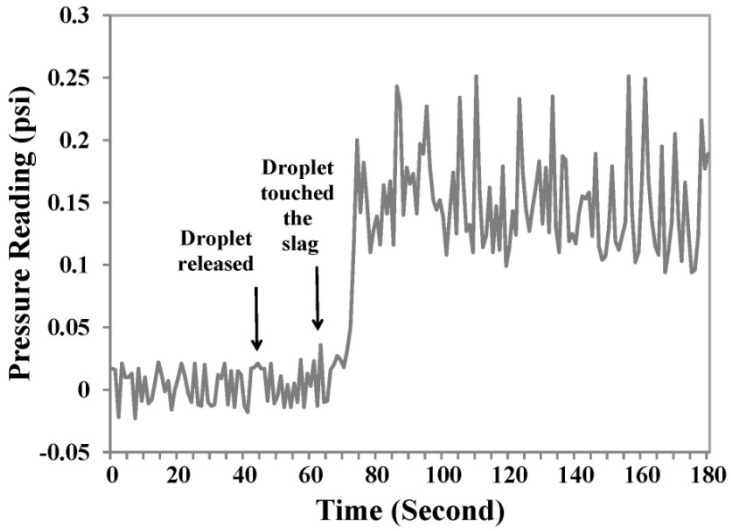

Figure 4.3 – Pressure variations with time in high-temperature experiments. This graph is related to experiment conducted at 1475°C using a 1 g copper sulphide droplet. The time at which pellet was released from the pellet dispenser and the time at which the droplet touched the slag is indicated.

As described in Chapter 3, pressure calibration was done before every experiment at high-temperature (an example of which is shown in Figure 3.8). Using the corresponding pressure calibration graph, the amount of gas evolved (moles) was determined. Initial gas

evolution rate, which has a direct relationship with the rate of desulphurization reaction (according to reaction [3.1]), can finally be determined.

In the case of Figure 4.3, initial increase in pressure was measured to be about 0.14 psi, which corresponded to 10.3 Ncm^3 of gas evolved. Initial gas evolution rate was measured to be $22.8*10^{-5}$ moles/s in this case.

As it is seen in Figure 4.3, after the initial increase in pressure following the droplet entrance to the slag, pressure remained almost constant for the rest of the experiment. This phenomenon was observed in all the experiments and suggested a change in the rate-controlling mechanism.

There was a very short delay between the time when droplet touched the slag and entered it and the time at which the pressure started to increase. This time is often called "the incubation period", which was very short in this study (only a few seconds). The incubation period in this study for a matte droplet containing no dissolved oxygen is because of the following stages that need some time to happen:

- Diffusion of O^{2-} from the slag to the slag/matte interface
- Desulphurization reaction at the interface, SO_2 nucleation and gas evolution

4.2.2. Effect of matte droplet size (mass)

At constant temperatures (1400, 1425, 1450 and 1475 °C) as well as slag composition (Fe^{3+}/Fe^{2+}= 0.49), the effect of Cu_2S droplet mass (size) on gas initial evolution rate was investigated. It is seen in Figure 4.4 (related to experiments performed at 1475 °C) that the rate (moles/second) increases with increasing the droplet mass. However, no linear correlation is observed. Similar behavior was observed for the experiments performed at other temperatures (1400, 1425 and 1450 °C).

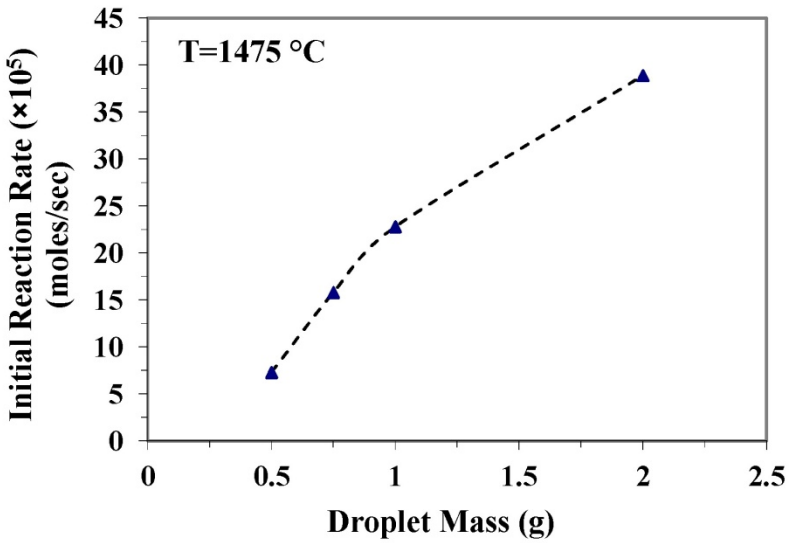

Figure 4.4 – Variation of gas evolution rate with droplet size (mass) at constant temperature (T=1475 °C) and slag composition (Fe^{3+}/Fe^{2+}= 0.49).

In Figures 4.5 to 4.7, variation of gas evolution rate with droplet size at different constant temperatures of 1450, 1425 and 1400 °C is demonstrated, respectively. No linear correlation could be observed between the droplet mass and the rate in those figures. Note that titration results showed that the slag composition was constant at all the experiments.

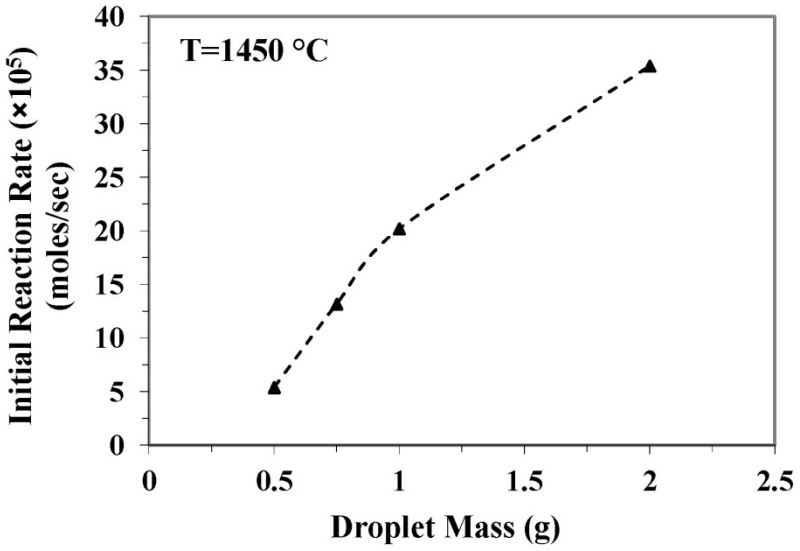

Figure 4.5 – Variation of gas evolution rate with droplet mass (gram) at constant temperature (T=1450 °C) and slag composition (Fe^{3+}/Fe^{2+}= 0.49).

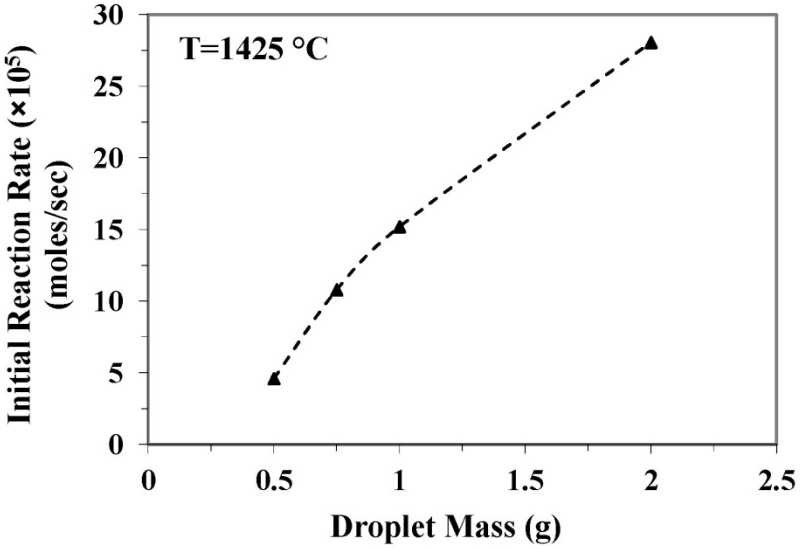

Figure 4.6 – Variation of gas evolution rate with droplet mass (gram) at constant temperature (T=1425 °C) and slag composition (Fe^{3+}/Fe^{2+}= 0.49).

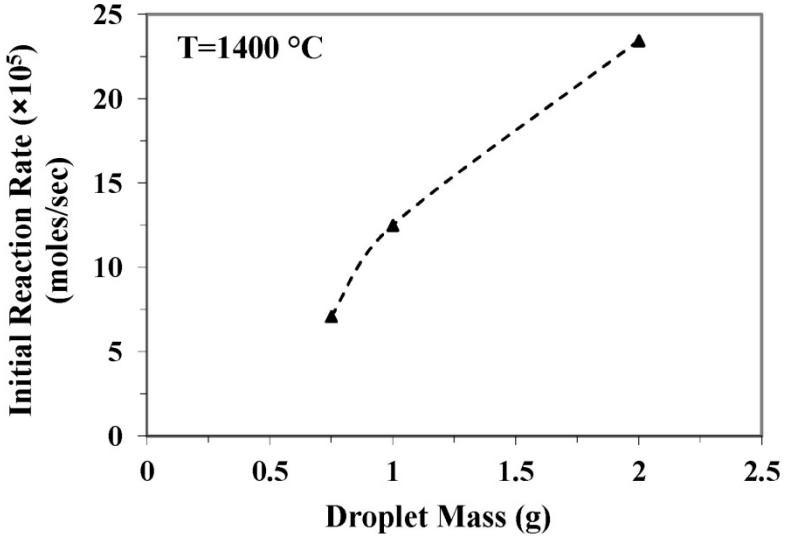

Figure 4.7 – Variation of gas evolution rate with droplet mass (gram) at constant temperature (T=1400 °C) and slag composition (Fe^{3+}/Fe^{2+}= 0.49).

If the relationship between rate and droplet mass was linear, it meant that the rate had a linear relationship with the droplet volume. If that was the case, it could be an indication of internal gas nucleation (droplet swelling) or sub-surface nucleation, according to the literature, which was discussed in more detail in Chapter 2. However, since the relationship between variations in droplet mass and gas evolution rate was not linear in this study and given the fact that gas halo could be seen surrounding the droplet in X-ray fluoroscopy images taken at high temperatures, it was decided to investigate whether or not there was any linear relationship between the rate and the droplet surface area. The results of this analysis are presented in the next section.

4.2.3. Rate correlations with droplet surface area

In this section, correlation between reaction rate and droplet surface area will be discussed. Droplet surface area was estimated by knowing the droplet mass (0.5, 0.75, 1 or 2), density of the copper sulphide (5.6 g/cm^3) and assuming the droplets were: a) spherical and b) fell in only one piece. The values obtained for surface area by this method are raw and have been named nominal droplet surface area (A_0). However, as it was observed by X-ray fluoroscopy only 0.5 g droplets fell in one piece and droplets equal to 0.75 gram or larger mostly fell in two pieces into the slag. This is important because droplet surface area is higher when droplet falls in more than one piece. In addition, X-ray observations showed that the two portions of the larger droplets fell as 2/3

and 1/3 of the total mass of the droplet. These important observations should be considered when calculating the surface area values for different droplets.

As observed by X-ray fluoroscopy, after a droplet fell into the slag, it quickly settled to the bottom of crucible and a bubble formed on top of the droplet. So only a fraction of droplet is directly in contact with the oxidizing slag. Therefore in order to have an accurate estimate of the droplet surface area available for reaction, the effective surface area ($A_{effective}$) which is directly involved in reaction should be calculated by deducting droplet/bubble as well as droplet/crucible contact area from A values obtained previously.

Droplet/bubble and droplet/crucible contact areas were estimated by carefully evaluating the X-ray fluoroscopy photos corresponding to different droplet sizes as well as SEM images obtained from quenched samples. For estimating droplet/bubble contact area, a spherical geometry was assumed ($A=2\pi RH$ where R is the cap radius, H is the cap height). The values determined were small and roughly equal to 0.02, 0.04, 0.06 and 0.11 cm^2 for 0.5, 0.75, 1 and 2 gram droplets, respectively. Values determined for droplet/crucible contact area were larger in comparison and were approximately equal to 0.23, 0.31, 0.38 and 0.60 cm^2 for 0.5, 0.75, 1 and 2 gram droplets, respectively. The estimated values were deducted from A values obtained previously and $A_{effective}$ values were obtained.

In Table 4.1, surface area values calculated for different droplet sizes have been presented. In this table, A_0 corresponds to nominal droplet surface area (if all the droplets had fallen in only one piece), A corresponds to estimated droplet surface area values

considering the fact that droplets equal to 0.75 gram or larger mostly fell in 2 pieces and $A_{effective}$ is effective droplet surface area values obtained after deducting droplet/bubble and droplet/crucible contact area from A values. Note that in all the next plots, values for $A_{effective}$ are considered.

Table 4.1– The value of droplet surface area calculated for different matte droplet sizes.

Droplet mass (g)	Droplet surface area (cm^2)		
	A_0	A	$A_{effective}$
0.5	0.966	.966	0.72
0.75	1.266	1.575	1.23
1	1.534	1.913	1.47
2	2.434	3.036	2.35

In Figure 4.8, which is related to experiments performed at T=1475 °C and constant slag composition (Fe^{3+}/Fe^{2+}= 0.49), it can be seen that gas evolution rate linearly increases with droplet surface area. This observation suggested that reaction has happened on the surface of the matte droplet and therefore as the surface area increases, reaction rate increases. This is in agreement with X-ray fluoroscopy observations, indicating gas halo formation around the droplet as well as bubble formation on top of the droplet during the experiments.

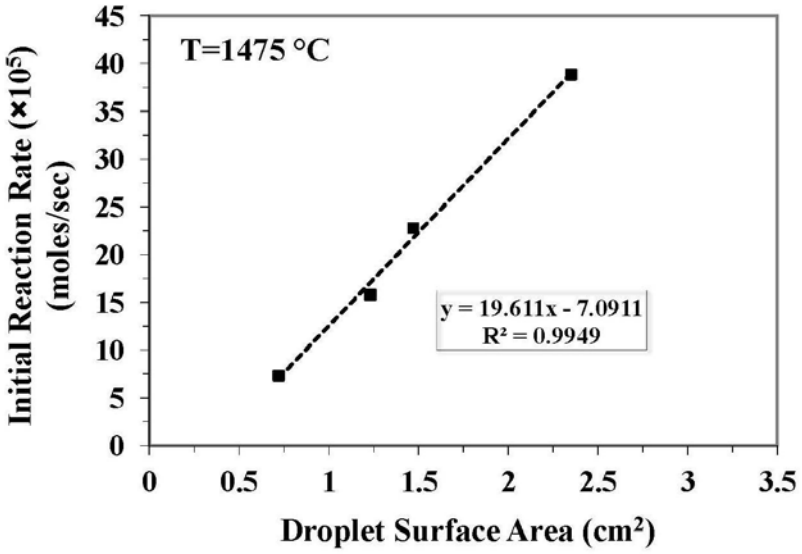

Figure 4.8 – Variation of gas evolution rate with droplet surface area (cm^2) at constant temperature (T=1475 °C) and slag composition (Fe^{3+}/Fe^{2+}= 0.49).

As it can be seen in this figure, extrapolation of the experimental data does not extend though the origin, in contrast to what was expected. Instead, it crosses the horizontal axis at about point 0.36, which roughly corresponds to a 0.1 gram droplet. This finding suggests that as the droplet gets smaller the rate becomes limited by something other than surface area.

In Figures 4.9 to 4.11, variations of gas evolution rate with droplet surface area is presented at different constant temperatures of 1450, 1425 and 1400 °C, respectively. Extrapolations of the experimental data points has also been shown in these figures. As it is seen, the extrapolation lines cross the horizontal axis at a point larger than zero. In lower temperatures, this line crosses the axis farther to origin.

High values of R^2 for the extrapolated lines in these figures indicates that there is a very good linear correlation between the experimental reaction rates and the calculated droplet surface areas in this study.

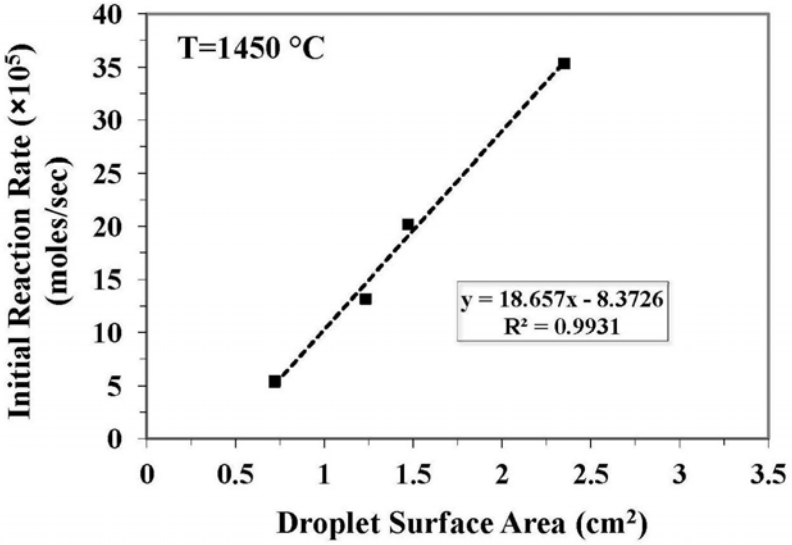

Figure 4.9 – Variation of gas evolution rate with droplet surface area (cm^2) at constant temperature (T=1450 °C) and slag composition (Fe^{3+}/Fe^{2+}= 0.49).

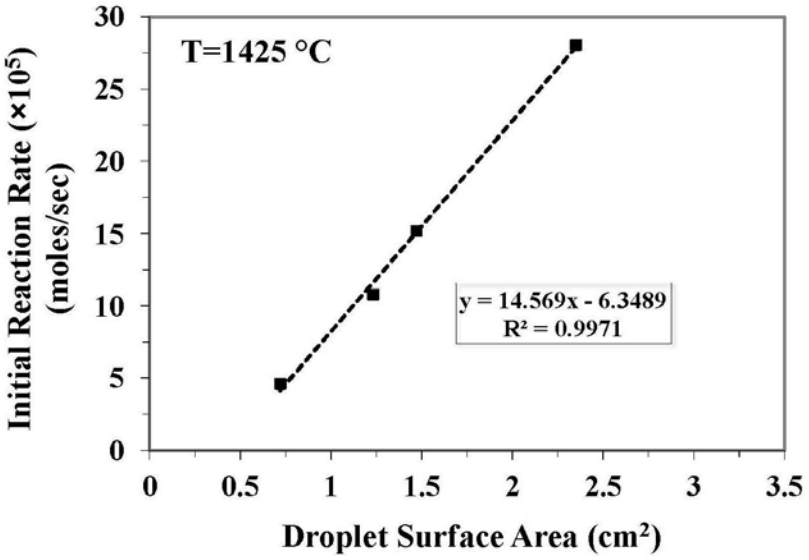

Figure 4.10 – Variation of gas evolution rate with droplet surface area (cm^2) at constant temperature (T=1425 °C) and slag composition (Fe^{3+}/Fe^{2+}= 0.49).

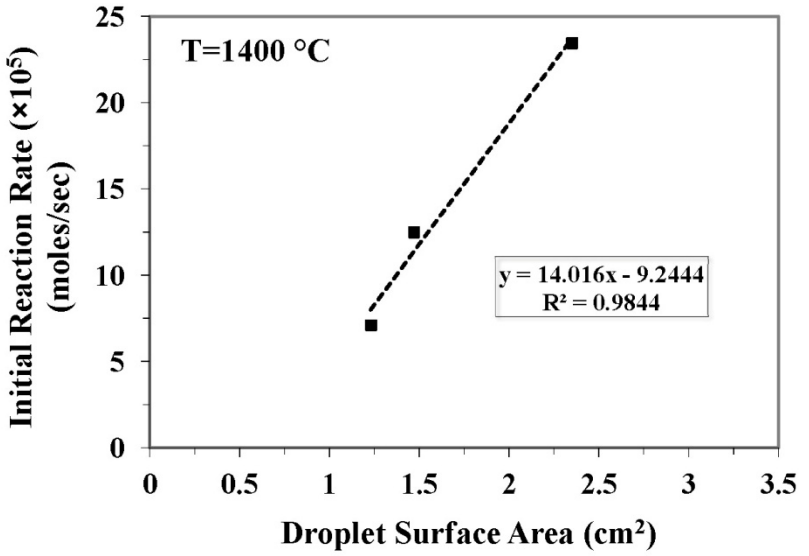

Figure 4.11 – Variation of gas evolution rate with droplet surface area (cm^2) at constant temperature (T=1400 °C) and slag composition (Fe^{3+}/Fe^{2+}= 0.49).

4.2.4. Effect of temperature

In Figure 4.12, variations of gas evolution rate per unit droplet surface area (R/A) is shown with temperature. Four lines are illustrated in the figure corresponding to four different matte droplet sizes (0.5, 0.75, 1 and 2 gram). It is seen that the rate exponentially increases as the temperature increases.

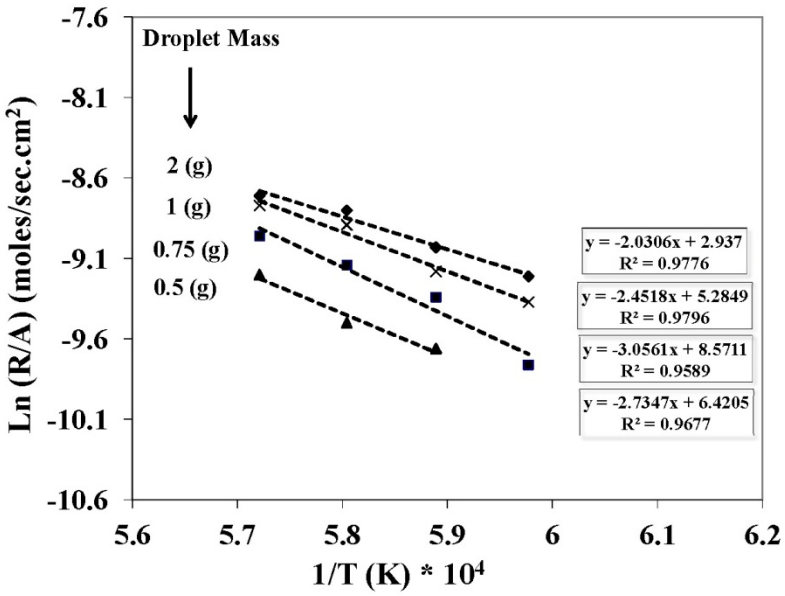

Figure 4.12 – Variation of gas evolution rate over surface area (LnR/A) with temperature for different matte droplet sizes (0.5, 0.75, 1 and 2 gram). The slag composition was constant (Fe^{3+}/Fe^{2+}= 0.49).

In order to eliminate the effect of droplet surface area and to only show the effect of temperature on the rate, values corresponding to Ln (R/A) were considered in this figure. Therefore, it was expected to see all the four lines overlapped on each other. The

extrapolated lines are very close but they are not exactly overlapped, which might be due to some small error in measured reaction rate values. This is especially the case for data obtained for the 0.5 gram droplets. This discrepancy is not unexpected and is another manifestation of the observation that whilst rate is a linear function of droplet area, a plot of rate versus area does not go through the origin.

4.2.5. Partial pressure of gaseous species

As a result of matt/slag reaction, SO_2 gas is produced (reaction 4.1). That reaction might also simply be shown as [74,75]:

$$\tfrac{1}{2} S_2 + O_2 = SO_2 \qquad \Delta G^\circ = -361665 + 72.68\ T \text{ (joules)} \qquad (4.2)$$

Other types of sulfur oxides (e.g. SO or SO_3) potentially may form as a result of reactions between different gaseous species. Theoretically, SO and SO_3 gases may form through the following reactions [74,75]:

$$\tfrac{1}{2} S_2 + \tfrac{1}{2} O_2 = SO \qquad \Delta G^\circ = -57781 - 4.98\ T \text{ (joules)} \qquad (4.3)$$

$$SO_2 + \tfrac{1}{2} S_2 = 2SO \qquad \Delta G^\circ = 246103 - 82.63\ T \text{ (joules) (at matte/gas interface)} \qquad (4.4)$$

$$\tfrac{1}{2} S_2 + \tfrac{3}{2} O_2 = SO_3 \qquad \Delta G^\circ = -457897 + 163.34\ T \text{ (joules)} \qquad (4.5)$$

$$SO_2 + \tfrac{1}{2} O_2 = SO_3 \qquad \Delta G^\circ = -96232 + 90.67\ T \text{ (joules)} \qquad (4.6)$$

SO_2 might also form at the gas/slag interface [74]:

$SO + ½ O_2 = SO_2$ $\Delta G° = -303884 + 77.66\ T$ (joules) (at gas/slag interface)(4.7)

It is important to know the dominant gaseous species in this system in order to determine the rate-determining steps. Additionally, determination of the equilibrium oxygen pressure in the Fe-O-S systems is significantly important not only because it is a measure of the oxidation state (the oxidizing capacity) of the slag [48], but also as knowing P_{O_2} is crucial for estimating the values of partial pressures of sulphide oxides in this system. Therefore, the results obtained for pressure of different gaseous species (P_{S_2} , P_{O_2} , P_{SO_x}) in this study will be briefly discussed in this section.

4.2.5.a. Equilibrium pressure of oxygen (P_{O_2})

As explained later in more detail, chemical titration results showed that regardless of the temperature used, 35.5 wt% ferrous iron (Fe^{2+}) and 17.25-17.50 wt% ferric iron (Fe^{3+}) were present in the molten synthesized slag. By knowing the amounts of total Fe (53.3 wt%) and SiO_2 (30.3 wt%) in the powder mixture employed for synthesizing the slag, it is possible to determine the values of P_{O_2}(equilibrium oxygen partial pressure) at different temperatures. Equation (2.29) proposed by Matousek [48] for iron silicate slags was employed in this regard.

The calculated values for P_{O_2} at different temperatures is presented in Table 4.2. As seen in this table, equilibrium oxygen pressure increases from about 2.574×10^{-5} to about 1.469×10^{-4} atm by increasing temperature from 1400 to 1475 °C.

In order to make sure that the determined values for P_{O_2} are reliable, relevant results and ternary diagrams reported by different researchers for iron silicate slags were reviewed carefully. As explained below, acceptable agreement was found between P_{O_2} results obtained in this study and those reported by different researchers.

In the FeO-Fe_2O_3-SiO_2 ternary diagram reported by Goel et al. [46] (Figure 2.14), a similar range of values (~10^{-5} atm) are reported for the equilibrium pressure of oxygen at 1400 °C for slag compositions relevant to this research (45.5 wt% FeO – 30 wt% SiO_2 – 24.5 wt% Fe_2O_3). In addition, Timucin et al. [53] in their calculated ternary diagram have reported that log $P_{O_2} \cong$ -4.1, (P_{O_2}= 7.94×10^{-5} atm) at 1450 °C, which is very close to what is reported in Table 4.2 for this temperature.

4.2.5.b. Equilibrium pressure of sulfur (P_{S_2}) and sulfur oxides (P_{SO_x})

As it was mentioned earlier, it is necessary to calculate P_{S_2} (equilibrium partial pressure of sulfur) at different temperatures. P_{S_2} can be determined at equilibrium by considering reaction (4.8):

$$2Cu\ (l) + \tfrac{1}{2}\ S_2\ (g) = Cu_2S\ (l) \qquad \Delta G^\circ = -148909 + 43.64\ T\ (\text{joules}) \qquad (4.8)$$

ΔG° for this reaction was calculated by considering the Gibbs free energy relations reported for reactions 4.9 [32], 4.10 [32] and 4.11 [76] in the literature.

$Cu_2S\ (s) = 2Cu\ (s) + ½\ S_2\ (g)$ $\Delta G° = 131796 - 30.79\ T\ (joules)$ (4.9)

$Cu_2S\ (s) = Cu_2S\ (l)$ $\Delta G° = 8996 - 6.40\ T\ (joules)$ (4.10)

$Cu\ (s) = Cu\ (l)$ $\Delta G° = 13054 - 9.62\ T\ (joules)$ (4.11)

The equilibrium constant (K) for reaction (4.8) is:

$$K = \exp\left(\frac{-\Delta G^{\circ}}{RT}\right) = \frac{a_{Cu_2S}}{a_{Cu}^2 . p_{S_2}^{\frac{1}{2}}} \quad (4.12)$$

Where R (the gas constant) = 8.314 (J/mole.K) and T corresponds to temperature in Kelvin. In addition, a_{Cu_2S} and a_{Cu} correspond to activities of Cu_2S and Cu respectively and P_{S_2} is partial pressure of sulfur in atm.

Since Cu_2S and Cu are in their standard state (liquid) at high temperatures employed in this study, a_{Cu_2S} and a_{Cu} are considered to be equal to 1. By calculating ΔG° for reaction (4.8), P_{S_2} values were determined at different temperatures.

Estimated values for partial pressure of S_2, O_2, SO, SO_2 and SO_3 are reported in Table 4.2 for different temperatures. First P_{S_2} and P_{O_2} were calculated by the method explained earlier and then P_{SO}, P_{SO_2} and P_{SO_3} were estimated by considering reactions 4.6 and 4.7 and assuming P_{Total} = 1 atm.

Table 4.2 – Calculated partial pressure of gas species (S_2, O_2, SO, SO_2, SO_3) at different temperatures.

Temperature (°C)	Pressure (atm)				
	P_{O_2}	P_{S_2}	P_{SO}	P_{SO_2}	P_{SO_3}
1400	2.574×10^{-5}	1.810×10^{-5}	7.236×10^{-4}	0.999	9.387×10^{-5}
1425	4.679×10^{-5}	2.481×10^{-5}	7.404×10^{-4}	0.999	1.143×10^{-4}
1450	8.361×10^{-5}	3.370×10^{-5}	7.570×10^{-4}	0.999	1.384×10^{-4}
1475	1.469×10^{-4}	4.538×10^{-5}	7.736×10^{-4}	0.999	1.666×10^{-4}

As seen in Table 4.2, SO/SO_2 are dominant in this system and P_{SO_3} is negligible. SO_3 is in fact unstable at high temperatures. Although compared to partial pressure of SO_2 (0.999 atm), P_{SO} is also very low, but it is still the largest among the minor species. Therefore, in evaluations of the rate-determining mechanisms, SO/SO_2 binary gas mixture would be considered later for mass transfer analysis inside the gas halo.

4.2.6. Rate-controlling mechanisms

The oxidation of copper sulfide matte in contact with fayalite oxidizing slag can be simply written as:

$$Cu_2S + O_2 = 2Cu + SO_2 \qquad \Delta G^\circ = -212756 + 29.04\ T \text{ (joules)} \qquad (4.13)$$

or $\underline{S} + 2\underline{O} = SO_2$, or $\frac{1}{2} S_2 + O_2 = SO_2$, where $\underline{S}$ and $\underline{O}$ are sulfur and oxygen dissolved in the matte droplet and the slag, respectively.

Reaction (4.13) happens at the matte/slag interface and of course oxygen here is in the form of O^{2-}, which is coming from the slag. Therefore, oxygen potential of the slag (which is controlled by Fe^{3+}/Fe^{2+} equilibrium) as well as mass transfer in the slag are two important factors.

Once SO_2 is released, a gas layer or halo may form around the droplet and thus reactions between gaseous species may be required for the overall desulphurization reaction to progress. As mentioned previously, SO/SO_2 gases are dominant in this system, so reactions (4.4) and (4.7) are significant as they take place at matte/gas and gas/slag interfaces, respectively. In addition to reactions at two different interfaces, counter mass transfer of SO/SO_2 gases in the gas halo (bubble) is important.

So in total, there are three chemical reactions and two mass transfer steps that may potentially be rate-controlling. This is also shown schematically in Figure 4.13.

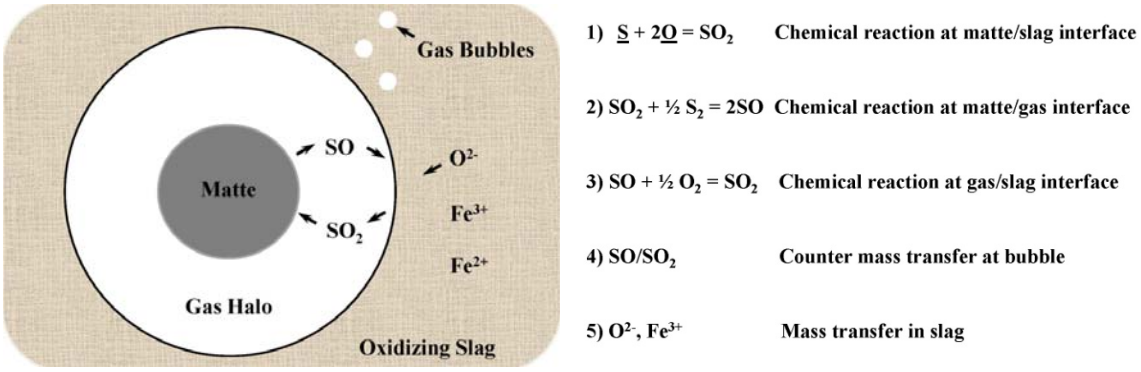

Figure 4.13 – Schematic diagram of the desulphurization reaction of matte droplet with an oxidizing slag.

If mass transfer in the slag was rate-controlling, other steps could be considered fast and in equilibrium. So reaction (4.13) is considered at equilibrium and P_{O_2} is calculated at equilibrium at different temperatures, considering that Cu_2S and Cu are at their standard state (liquid; $a_{Cu_2S} = a_{Cu} = 1$) and $P_{SO_2} = 1$ atm. Subsequently, using Matousek's formula (Equation 2.29) for equilibrium P_{O_2} in iron silicate slags, corresponding values for Fe^{3+}/Fe^{2+} ratio is obtained, from which Fe^{3+} values can then be determined (as Fe total in slag is known). Using this method and as SO_2 gas evolution rate is measured in experiments done at different temperatures, mass transport constant in slag (k_s) and subsequently the activation energy (Q) can be estimated. Details of this analysis are explained below.

As mentioned earlier, Fe^{3+}/Fe^{2+} ratio controls the oxygen potential of the slag [47,48,55] and a higher ratio means a higher slag oxygen potential. Therefore, it is reasonable to

consider the flux of Fe^{3+} in the slag when evaluating whether mass transfer in the slag might be the rate-controlling step. For the flux of Fe^{3+} in the slag, it can be written:

$$J_{Fe^{3+}} = \frac{k_S .A .\rho_S}{100\, MW_{Fe}} (Fe_B^{3+} - Fe_i^{3+}) = 4J_{SO_2} \quad (4.14)$$

Where $J_{Fe^{3+}}$ is the flux of Fe^{3+} in the slag given in mole/s, J_{SO_2} is the SO_2 gas evolution rate (experimentally measured), k_s corresponds to mass transport constant in the slag (cm/s), A is the matte droplet-slag interfacial area (cm^2), ρ_s is the density of the slag (measured to be equal to 3.7 g/cm^3), MW_{Fe} is the molar weight of Fe and $Fe_B^{3+}$and Fe_i^{3+} correspond to Fe^{3+} concentration in the bulk of the slag and at the interface in wt%, respectively. $J_{Fe^{3+}}= 4J_{SO_2}$ because 4 moles of Fe^{3+} is needed in order to produce 2 moles of O^{2-}, which will form one mole of SO_2 when reacted with S^{4+}at the interface. So the flux of Fe^{3+} in the slag is four times larger than that of SO_2 gas evolution in this system. Reaction (4.15) shows the charge transfer in the slag and O_{ads} represents adsorbed oxygen at the surface of the matte:

$$2Fe^{3+} + O^{2-} = 2Fe^{2+} + O_{ads} \quad (4.15)$$

Equation (4.14) can be written for k_s (mass transport constant in the slag):

$$k_S = \frac{400.MW_{Fe}.J_{SO_2}}{A.\rho_S.(Fe_B^{3+} - Fe_i^{3+})} \quad (4.16)$$

Values for matte-slag interfacial area (A) for different droplet sizes are given in Table 4.1. Values for J_{SO_2} are those measured in the experiments. Fe_B^{3+} was measured by titration and is equal to about 17.4 wt%. Fe_i^{3+} values were determined by the method previously

explained. Fe_i^{3+} values were found to be equal to 13.99, 13.04, 12.14 and 11.33 wt% at 1400, 1425, 1450 and 1475 °C, respectively. Using these data, k_s values can be determined at different temperatures.

In Figure 4.14, variations of mass transport constant in the slag with temperature is illustrated for different matte droplet sizes. It is seen that k_s increases with increasing temperature. Since the effect of surface area on rate is considered in Equation (4.16), it was expected that four curves in this figure overlap on each other or be very close. There might be two potential reasons why this has not happened, one might be because of geometrical aspects of the droplets and the other might be due to difficulties and uncertainties associated with rate measurements for smaller droplets (especially 0.5 gram droplet), which exhibited much lower gas evolution rates compared to larger droplets especially in lower temperatures.

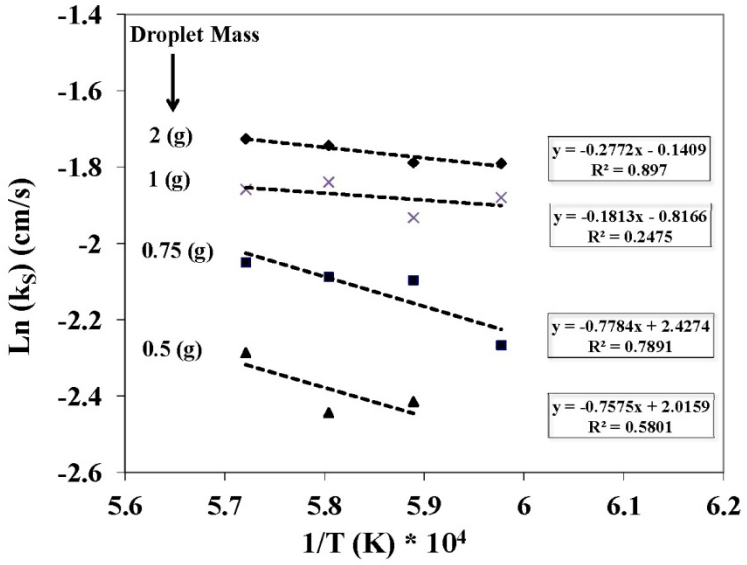

Figure 4.14 – Variation of mass transport constant in the slag (Lnk_s, cm/s) with temperature (Kelvin) for different matte droplet sizes (0.5, 0.75, 1 and 2 gram).

Considering the following Arrhenius equation, values for activation energy can be found from the data presented in Figure 4.14.

$$k_s = k_0 . e^{(-Q/RT)} \quad (4.17)$$

In this equation, k_0 is the frequency constant, Q is activation energy (J/mole), R is the gas constant (8.314 J/mole.K) and T is temperature in Kelvin.

Curves of least squares in Figure 4.14, yielded activation energies in the range of 14.7-64.9 kJ/mole, which are a characteristic of mass transfer control [77]. Activation energies for chemical reaction control and adsorption-desorption control are generally much higher and are in the range of 400-600 kJ/mole [77,78], therefore it can be concluded that mass

transfer in the slag is the controlling mechanism in this system, prior to gas halo formation.

As it was seen in Figure 4.3, after a sharp increase in pressure inside the furnace, gas evolution was substantially suppressed. This sudden change in reaction rate indicates that the controlling mechanism changes in later times. Since gas halo formation was obvious from X-ray fluoroscopy observations, it is reasonable to believe that the controlling mechanism might have changed to SO/SO_2 counter mass transfer in the halo. This is evaluated below.

For the flux of SO_2 in the gas halo, it can be written that:

$$J_{SO_2} = \frac{D_{SO-SO_2}.P}{\delta RT}\left(P_{SO_2}^{s/g} - P_{SO_2}^{m/g}\right) = -J_{SO} \qquad (4.18)$$

J_{SO_2} and J_{SO} are the flux of SO_2 and SO gases in the gas halo, respectively, in mole/s. $D_{SO\text{-}SO_2}$ is the SO/SO_2 binary diffusion coefficient or intermolecular diffusion coefficient (diffusivity) for the $SO\text{-}SO_2$ gas mixture and given in cm^2/s, P is total pressure (1 atm), δ is the thickness of the gaseous layer or in other words gas diffusion path length and is given in cm, R is the gas constant (82.06 cm^3.atm/mole.K), T is temperature in Kelvin and $P_{SO_2}^{s/g}$ and $P_{SO_2}^{m/g}$ correspond to equilibrium partial pressure of SO_2 at the slag/gas interface and at the matte/gas interface, respectively and are given in atm.

If mass transfer in the gas bubble is assumed to be the rate controlling step, then four other steps would be considered fast and reactions (4.4) at the matte/gas and (4.7) at the gas/slag interfaces would be at equilibrium. Therefore, $P_{SO_2}^{s/g}$ and $P_{SO_2}^{m/g}$ values can be

estimated from the two aforementioned reactions at equilibrium and considering P_{total} = P_{SO}+ P_{SO_2}= 1 atm and using $P_{O_2}$and P_{S_2}values calculated for different temperatures, which were presented in Table 4.2. Calculated P_{SO_2}values at the slag/gas and the matte/gas interfaces for different temperatures are presented in Table 4.3.

Table 4.3 – Calculated partial pressure of SO_2 at the slag/gas interface as well as at the matte/gas interface at different temperatures.

P_{SO_2} (atm)	Temperature (°C)			
	1400	1425	1450	1475
At slag/gas interface ($P_{SO_2}^{s/g}$)	0.99928	0.99926	0.99924	0.9992
At matte/gas interface ($P_{SO_2}^{m/g}$)	0.99865	0.99830	0.9980	0.9975

$D_{SO\text{-}SO_2}$ values were calculated using the equation proposed by Fuller et al. [79]. $D_{SO\text{-}SO_2}$ values were determined to be 2.12, 2.18, 2.23 and 2.29 cm^2/s at 1400, 1425, 1450 and 1475 °C, respectively.

As shown later in the optical microscopy images of quenched matte/slag samples, a gas halo thickness of about 50 μm could be seen around the matte droplets in the micrographs. If this is assumed to be the value for δ in Equation (4.18), then values for J_{SO_2} for the time such a gas halo is formed around the droplet can be calculated. J_{SO_2} values obtained were in the order of 10^{-6} mole/s, which is in good agreement with the gas

evolution rate values obtained for the later times in the experiments when the curve corresponding to the gas evolution rate became almost horizontal, meaning a very slow reaction.

4.2.7. Conclusions

No linear relationship was observed between droplet mass and gas evolution rate. However, a linear relationship was found between rate and the droplet surface area. These two findings suggest that gas nucleation occurred on the surface of the droplet, which is in agreement with gas halo observations in X-ray fluoroscopy movies captured during the high-temperature experiments.

As mentioned in the literature review, gas halo formation had been reported by numerous researchers in Fe-C droplet experiments, when higher content of carbon was used, especially when the slag had low oxygen potential. In contrast, when carbon content of the metal droplet was low or the mass transfer of oxygen from the slag was higher (higher slag oxygen potential), internal gas nucleation, and droplet swelling was reported. This might be the key point here and can explain the reason why a gas halo was formed around the matte droplets in this investigation.

In order for the desulphurization reaction to proceed (reaction [4.1]), oxygen from the slag needs to diffuse to the slag/matte interface. Since the sulfur content of the copper sulphide droplet is high (~ 33.1 mol%) and thus sulfur is readily available, it does not

need to diffuse to the interface. Therefore, it is expected that the supply of S from the droplet to the slag/matte interface be able to easily keep up with the supply of O from the slag. Consequently, gas nucleation inside the matte droplet and as a result, droplet swelling, which occurred in the case of low carbon Fe-C metal droplets in contact with an oxidizing slag, was not seen.

Five potential rate-controlling steps composed of three chemical reactions (at matt/slag, matte/gas and gas/slag interfaces) and two mass transfers (in the slag and in the gas halo). Activation energies determined were in agreement with the assumptions that mass transfer in the slag was the rate-controlling step. In addition, counter mass transfer of SO/SO_2 gases in the gas halo was found to be the rate controlling mechanism when the thickness of the halo became large enough, in later times. For the case of having a 50-micron-thickness halo forming around the droplet, which is seen in optical microscopy images, it was found that the mass transfer of gases in the gas halo was the rate controlling step, as it was much slower than the experimental values obtained for gas evolution rate.

It was found that gas evolution rate exponentially increased with increasing temperature. Although the desulphurization reaction is exothermic, higher temperatures appeared to be highly beneficial in terms of increasing the rate. Temperature not only facilitates mass transfer, but also lowers the viscosity of the slag. It is especially important since viscosity of slag in this study was high due to high amounts of silica present in the liquid slag. Kaiura et al [80] investigated the viscosity of fayalite-based slags and reported that slag viscosity dramatically decreased with increasing temperature. For a similar slag

composition (i.e. SiO_2 = 35 wt%, FeO = 58 wt% and Fe_2O_3 = 7 wt%) to that synthesized in this study, they reported that slag viscosity significantly decreased from 128 to 81 cP (centipoise) by increasing temperature from 1250 to 1350 °C.

Since gas halo formation dramatically decreased the rate, it appears that stirring could be beneficial and in fact in industry, oxygen/air blown to the converting furnace induces stirring, which helps to increase the rate.

4. 3. Chemical and structural analysis

In order to better understand the phenomena happening during the high-temperature experiments including any possible gas halo formation, and to make sure that the desulphurization reaction has indeed taken place and a product phase was formed, an extensive chemical and structural analysis was performed. In this regard, optical as well as scanning electron microscopy, the latter equipped with an energy dispersive X-ray spectrometer (EDS) was employed. Furthermore, chemical titration was performed on the slag samples synthesized at different experimental temperatures.

Optical microscopy analysis was performed on copper sulphide, slag powder mixture as well as synthesized fayalite slag. In addition, an extensive structural analysis was done on slag/matte samples quenched from high temperatures at time equal to 2 minutes after the droplet touched the slag for the first time. The obtained results are presented in this section.

4.3.1. Synthetic oxidizing slag

Synthesized oxidizing slag was produced by exposing the slag powder mixture to the experimental temperatures used in this study. Chemical titration as well as structural analysis were conducted on the synthesized slag. Since argon gas was injected into the sealed furnace prior to the experiments, it was expected that iron powder in the slag powder mixture will react with oxygen in hematite and transform most of the hematite (Fe_2O_3, with 30.1 wt% oxygen content) to other types of iron oxides with lower contents of oxygen such as magnetite (Fe_3O_4, 27.7 wt% O) and wustite (FeO, 22.3 wt% O). FeO itself could form fayalite ($2FeO.SiO_2$) in association with silica, which was also present in the slag powder mixture.

4.3.1.a. Chemical titration and XRD analysis

In order to determine the amount of iron in different forms of metallic iron, Fe^{2+} (ferrous iron) and Fe^{3+} (ferric iron) in slags synthesized at different experimental high-temperatures, standard chemical titration was performed using potassium dichromate as the oxidizing titration agent. Details of the procedure and the chemicals employed in this regard are mentioned in Appendix 1. As explained there, in order to increase the accuracy of the results, titration was done at least 3 times on each slag sample and an average value was considered for reporting the results. The results were in a very close range.

The results obtained from chemical titration done on synthesized slags quenched from different high-temperatures of 1400 to 1475 °C are presented in Table 4.4. The results for different types of iron are very close, regardless of the temperature at which slag was synthesized. Titration results showed that there is no significant amount of metallic Fe in the molten slag. Ferrous (Fe^{2+}) and ferric (Fe^{3+}) iron was measured to be around 35.5 and 17.5 wt%, respectively, regardless of the temperature used.

Table 4.4 – Results obtained from chemical titration performed on synthesized slags quenched from different high temperatures of 1400, 1425, 1450 and 1475°C.

Temperature (°C) / Type of iron (wt%)	1400	1425	1450	1475
Metallic Fe	~ 0	~ 0	~ 0	~ 0
Ferrous Fe (Fe^{2+})	35.5	35.5	35	35
Ferric Fe (Fe^{3+})	17.25-17.50	17.25-17.50	17.50	17.50

In Figure 4.15, ternary phase diagram of Fe_2O_3, FeO and SiO_2 at T=1400 °C and P=1 atm is constructed using FactSage. Note that the axes are in mole fraction. The black star shown on the diagram indicates the projected location at which the synthesized slag in this study falls, considering the amount of silica added to the slag powder mixture (30.3 wt% corresponding to mole fraction equal to 0.39) and the amount of FeO (45.7 wt%,

mole fraction equal to 0.49) that is present in the slag. Note that for simplicity, it was assumed that all Fe^{2+} and Fe^{3+} measured by titration had formed FeO and Fe_2O_3, respectively. According to the diagram, the slag is in molten state at the temperatures studied in this research. The same conclusion could be drawn considering FeO-Fe_2O_3-SiO_2 ternary phase diagrams proposed by Schuhmann et al. (Figure 2.12) and Goel et al. (Figure 2.13).

According to the ternary diagram [46,51,53] and as meniscus formation was clear in the fluoroscopy images, no unreacted iron or hematite should be present in the synthetic slags. However, in order to confirm fayalite formation, X-ray diffraction (XRD) analysis was performed on one of the synthetic slags. In XRD pattern presented in Figure 4.16, which is related to the synthetic slag quenched from 1400 °C, diffraction peaks corresponding to fayalite, silica as well as magnetite are dominant. In addition, no hematite or unreacted metallic iron was detected by the XRD.

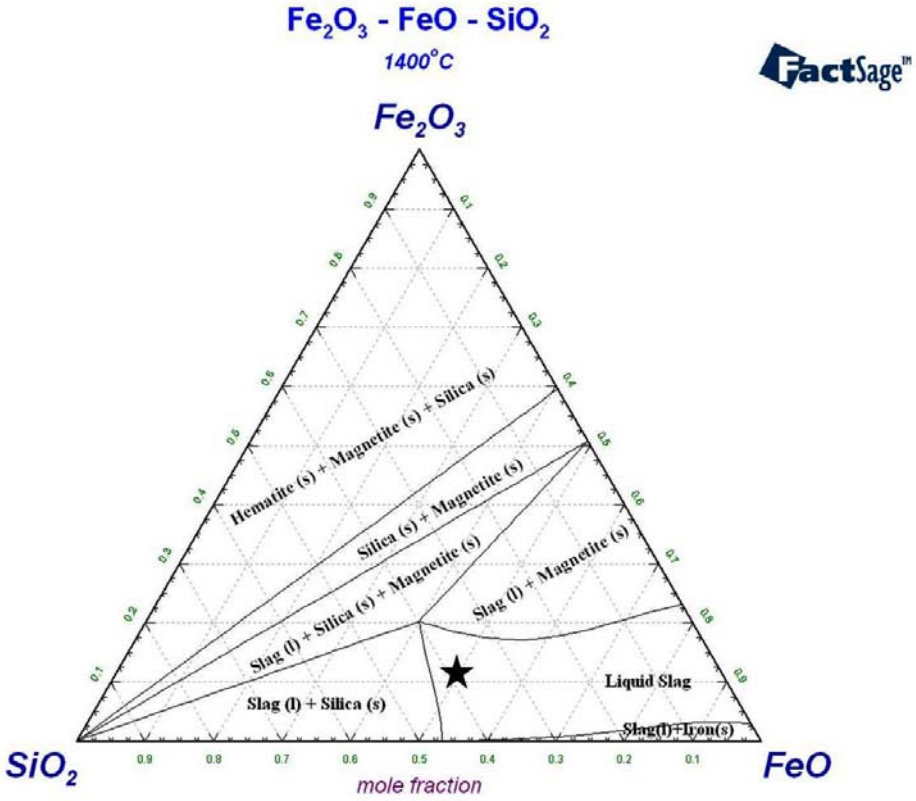

Figure 4.15 – FeO-Fe_2O_3-SiO_2 ternary phase diagram at T=1400 °C and P=1 atm, constructed using FactSage™.

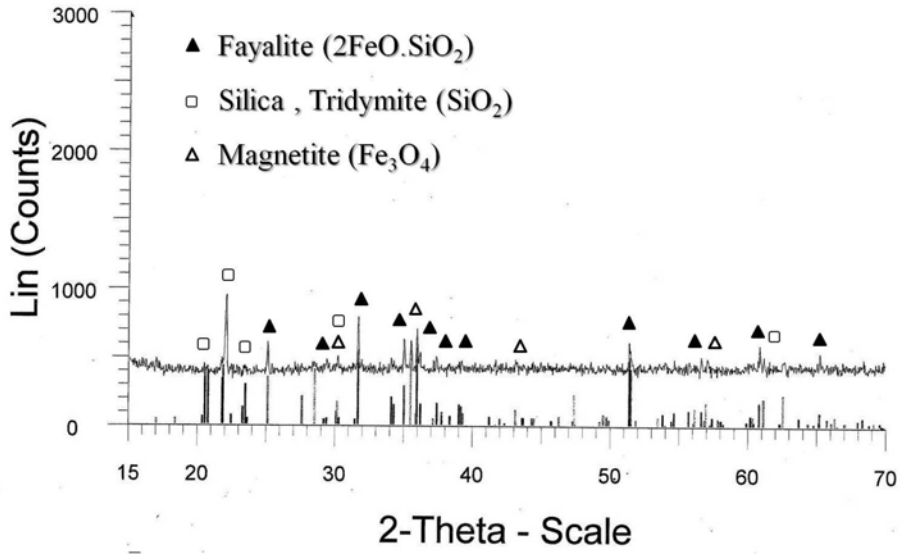

Figure 4.16 – X-ray diffraction patterns of synthesized slag quenched from 1400 °C. Fayalite, silica as well as magnetite phases are detected. No hematite or unreacted iron was detected by the XRD.

4.3.1.b. Optical microscopy analysis

In Figure 4.17, optical microscopy micrographs obtained from the synthetic slag produced at 1350 °C are illustrated. This sample was left at this high temperature for 6 hours and consequently as it is seen, the microstructure is completely transformed from what is seen in Figure 3.3 to a dual phase fayalite structure (Fe_2SiO_4 or $2FeO.SiO_2$) and magnetite. Large elongated agglomerates of fayalite are seen lighter in color and magnetite crystals can be seen darker in this figure.

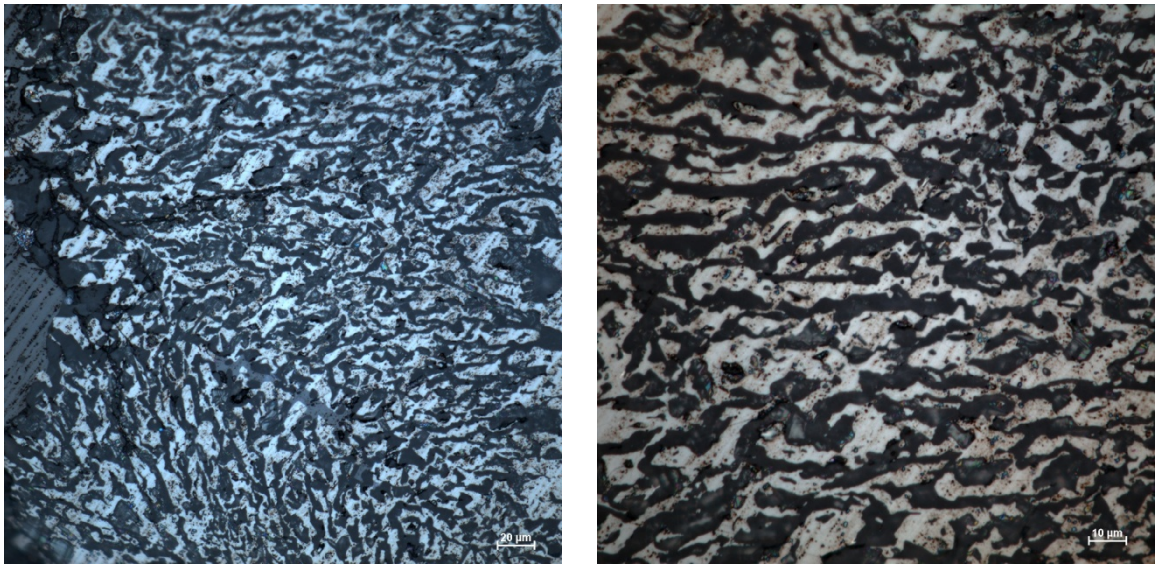

Figure 4.17 – Synthetic oxidizing slag. Micrographs obtained from optical microscopy performed on synthetic slag produced at 1350 °C after 6 hours. Large elongated agglomerates of fayalite and black magnetite crystals can be seen. The sample was cold mounted, polished using water and no etching was applied.

A similar microstructure can be seen in Figure 4.18. The two micrographs in this figure correspond to the slag produced at 1425 °C. Given the higher temperature used in this case, coarsening due to faster diffusion has happened and thus a coarser fayalite and magnetite structure is obvious in Figure 4.18 compared to the microstructure obtained at the same magnification shown in Figure 4.17. It is to be noted that microstructure of the synthesized slags obtained in this study resemble those reported by Mihailova et al [81] for copper slags in flash smelting furnace.

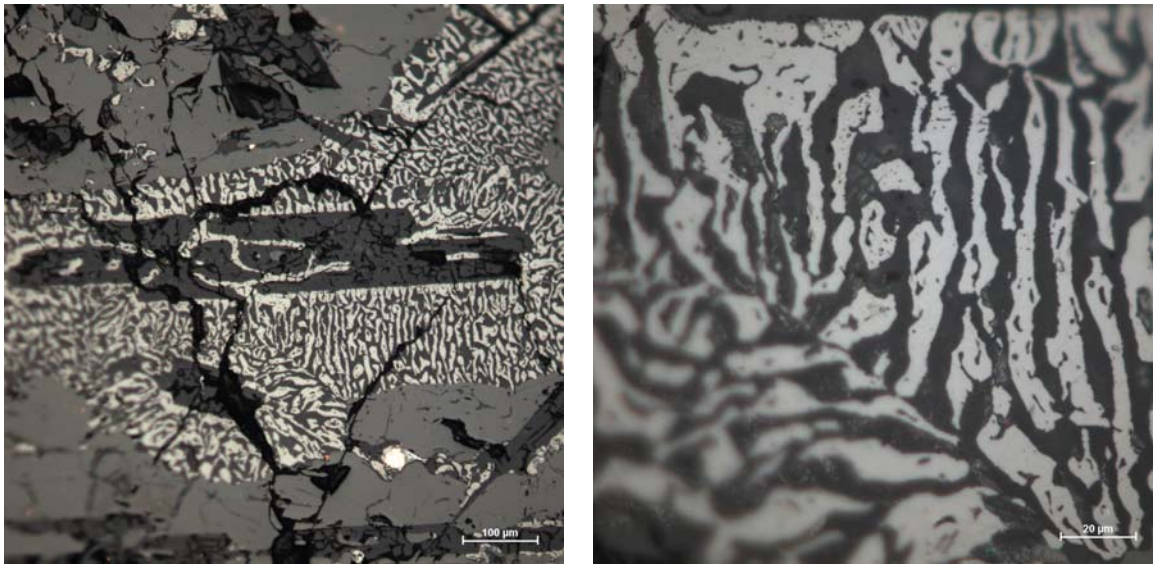

Figure 4.18 – Synthetic oxidizing slag. Micrographs obtained from optical microscopy performed on synthetic slag produced at 1425 °C. Coarsened fayalite crystals alongside the black magnetite crystals can be seen in the photos. The sample was cold mounted, polished using water and no etching was applied.

4.3.2. Slag/matte quenched samples

In order to investigate any possible halo formation around the droplet, occurrence of the desulfurization reaction and any other possible reactions, formation of product phases and generally to better understand and trace any phenomena that might be happening during the high-temperature reaction, an extensive structural analysis was conducted on slag/matte samples quenched from high temperatures. The time at which the samples were quenched was 2 minutes after the time the droplet touched the slag for the first time. An X-ray fluoroscopy device made it possible to carefully follow this specific time during the experiments.

Optical microscopy was done to study the microstructure (presented earlier). Then, extensive EDS microanalysis was performed on various areas of the quenched samples including slag, droplet, reaction zone as well as on the product phases that had appeared because of reaction(s) happening during the high-temperature experiment. EDS was used in order to perform point elemental analysis and to determine what elements were present in different phases in the microstructure.

Optical microscopy images of synthesized slag produced at two different temperatures of 1350 and 1425 °C were presented earlier. Similar slag phases were obtained in different temperatures. So here, first EDS results of the slag area in different quenched samples will be presented and then optical microscopy images and EDS results obtained for samples quenched from different high temperatures will be discussed separately and finally a brief conclusion will be given.

To simplify the explanations, from now on samples quenched from temperatures 1400, 1425, 1450 and 1475 °C will be called as samples A, B, C and D, respectively. As it was mentioned previously, a similar droplet size of 0.75 gram was used for all the quenched samples.

In Figures 4-19 to 4-22, results obtained from EDS analysis performed on slag of the quenched samples A, B, C and D are presented. Each figure consists of one SEM image of the slag area, corresponding EDS spectrum of the specific location, as well as the estimated amounts of different elements detected in the spectrum. It is to be noted that usually a standard sample has to be used for accurate quantitative results by means of

EDS. The compositional data presented as EDS results in this study are more of a semi-quantitative nature, as no standard sample was employed. However to increase the reliability of the results, numerous point elemental analyses were performed on the samples in each specific location on the microstructure whether it be slag, droplet or product phases.

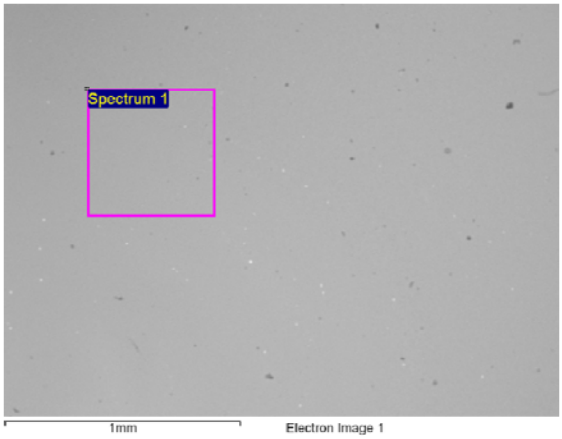

O	44.63	Ca	1.40
Fe	26.90	Mg	0.47
Si	19.60	P	0.33
Al	3.37	K	0.31
Mn	2.98		

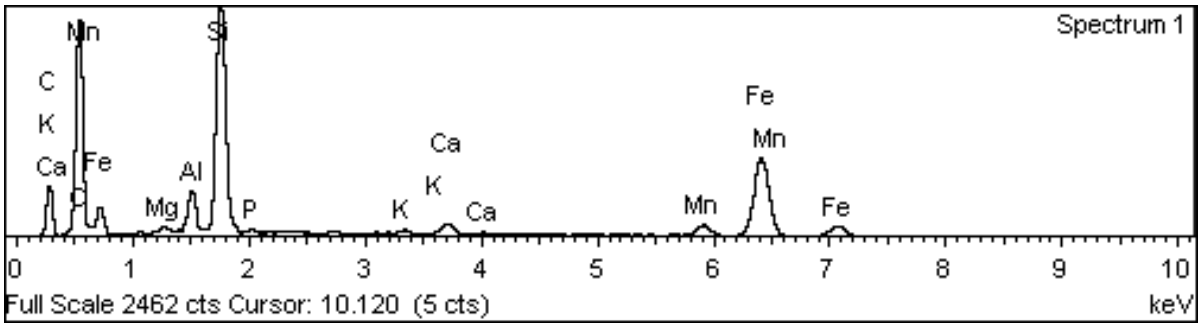

Figure 4.19 – SEM micrograph as well as EDS results obtained from the slag area. Results are for the slag/matte sample quenched from 1400 °C (sample A) and the data presented in the table are in wt%.

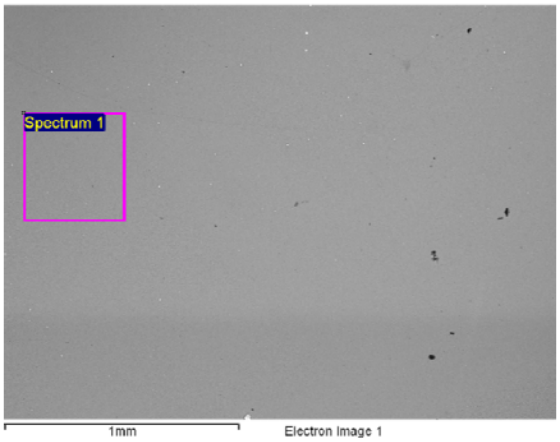

O	45.61	Ca	1.35
Fe	26.06	Mg	0.57
Si	19.71	P	0.28
Al	3.21	K	0.33
Mn	2.89		

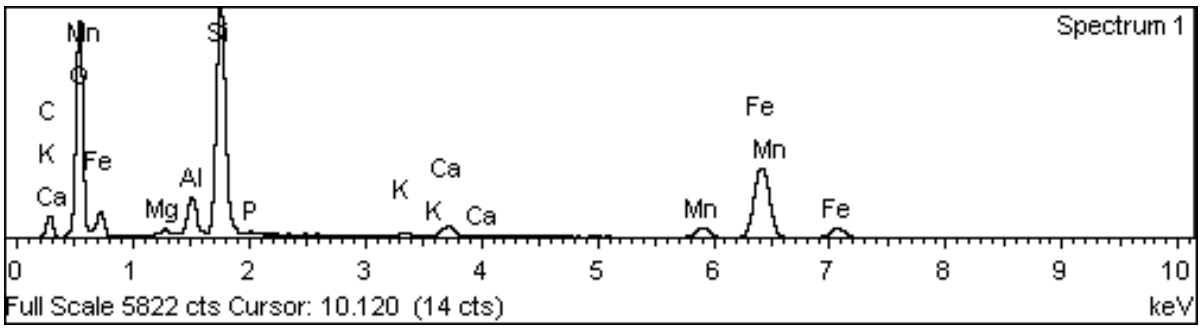

Figure 4.20 – SEM micrograph as well as EDS results obtained from the slag area. Results are for the slag/matte sample quenched from 1425 °C (sample B) and the data presented in the table are in wt%.

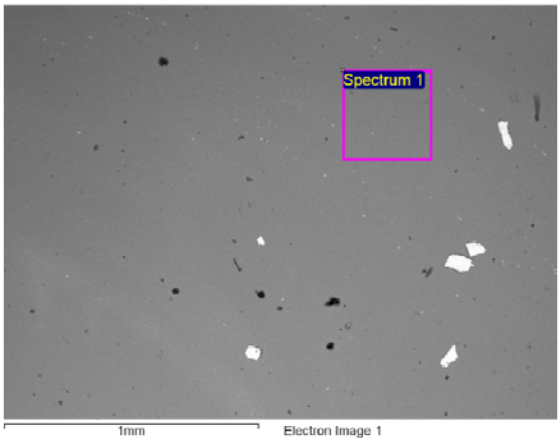

O	45.61	Ca	1.32
Fe	25.24	Mg	0.46
Si	18.03	P	0.27
Al	5.68	K	0.30
Mn	2.44	Cu+S	0.64

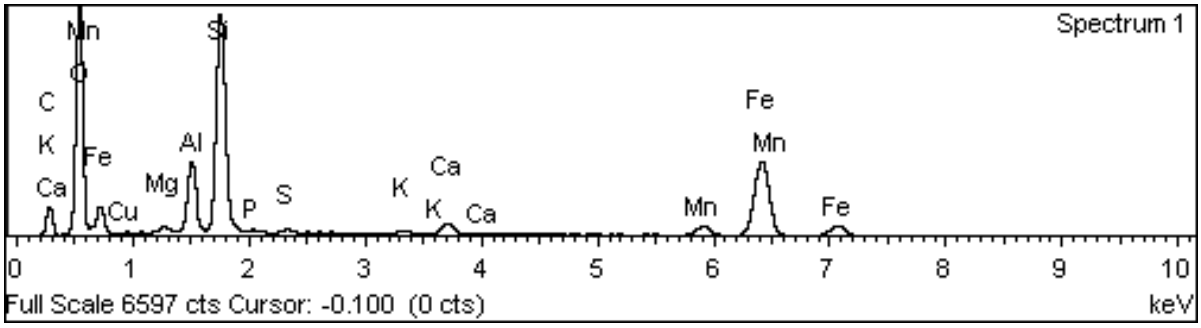

Figure 4.21 – SEM micrograph as well as EDS results obtained from the slag area. Results are for the slag/matte sample quenched from 1450 °C (sample C) and the data presented in the table are in wt%.

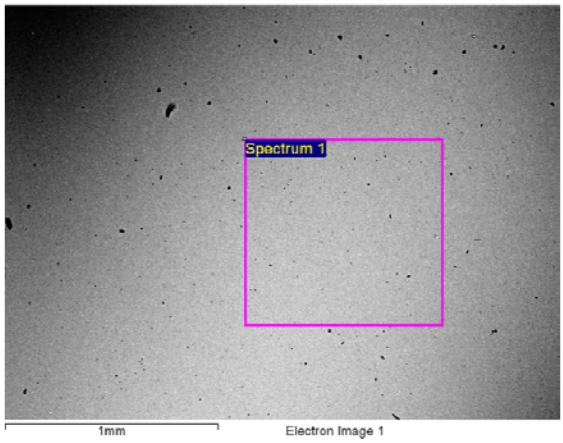

O	44.05	Ca	1.39
Fe	26.98	Mg	0.57
Si	18.53	P	0.28
Al	4.76	K	0.25
Mn	2.86	Cu+S	0.13

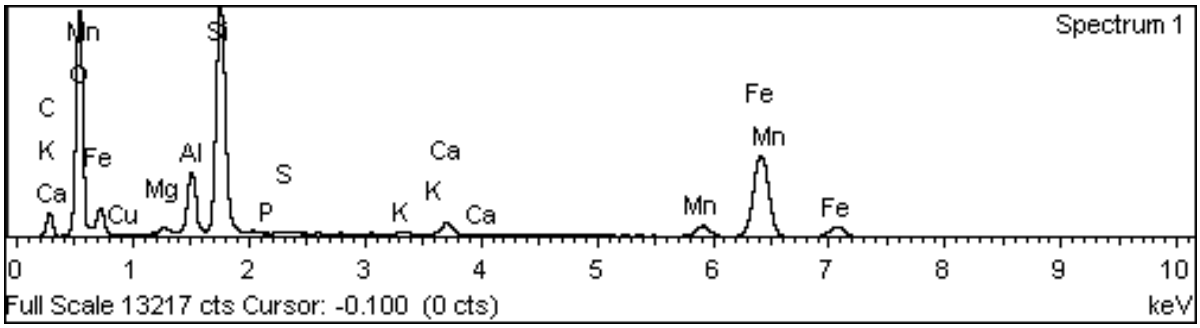

Figure 4.22 – SEM micrograph as well as EDS results obtained from the slag area. Results are for the slag/matte sample quenched from 1475 °C (sample D) and the data presented in the table are in wt%.

As determined from EDS spectra illustrated in Figures 4.19 to 4.22, oxygen (O), iron (Fe) and silicon (Si) are the major elements available in the slag with their characteristic X-ray signals (peak) dominating the spectrums of different samples of A to D. The estimated total amount of these three elements in the slag is roughly about 88-91 wt%, details of which can be seen in the figures. It is to be noted that data presented in this study for the amount of each element was obtained after excluding the effect of carbon coating on the

samples as part of samples' preparation step prior to EDS analysis. To do that, specific software was used, details of which were mentioned earlier in Chapter 3.

Following the three major elements mentioned above, aluminum (Al) and manganese (Mn) with an estimated total weight percent of 6.3-8 wt% are the elements with the next highest content in the slag. While the presence of Si, O and Fe in the slag is well expected given the fact that hematite, silica and iron have been used for synthesizing the slag, the appearance of Mn and Al in the EDS spectrums of the slag area of different quenched samples are totally unexpected in the first glance. In fact, one might question where their origin is. Well, it appears that alumina crucible used for doing the experiments is to blame for the presence of these elements as well Ca and Mg in the slag, although the amount of the latter elements is very low. There are also some very low amounts of copper and sulfur detected by EDS in the slag of samples C and D that presumably came to this area from the droplet and the product phase during the polishing which was done on the samples as part of the preparation steps prior to EDS analysis.

As illustrated in Table 4.5, the results given for O, Fe and Si in the slag are largely consistent and in a similar range in different samples of A to D. This is also true for Mn. However, for Al, it is seen that its content in the slag increases at higher temperatures. Al content of the slag jumps from about 3.4 wt% to about 5.7 wt%, which is remarkable even considering the semi-quantitative nature of the EDS results.

Table 4.5– Summary of the EDS results obtained from the slag areas of quenched samples A-D (1400-1475 °C with 25-degree intervals). Results are shown in wt% for elements O, Fe, Si, Mn and Al.

Element / Sample	O	Fe	Si	Mn	Al
A	44.6	26.9	19.6	3.0	3.4
B	45.6	26.1	19.7	3.0	3.2
C	45.6	25.2	18.0	2.4	5.7
D	44.1	26.9	18.5	2.9	4.8

The synthesized slag appears to be highly corrosive in this study. As mentioned earlier in Chapter 3, it has been reported [73] that FeO and Al_2O_3 tend to form S-type spinel in elevated temperatures. In fact, the effect of slag corrosivity on the crucible could easily be seen after the experiments especially those performed at higher temperatures. Therefore, the higher content of Al in slag can be attributed to increased slag corrosivity and enhanced diffusivity.

Higher oxygen content of the slag in EDS results compared to the theoretical values (33.64 wt% O in the slag powder mixture) can be attributed to the following factors:

- Slag oxygen pick-up from the atmosphere during quenching and preparation of the samples before structural analysis
- Oxygen enters the slag in the form of alumina from the wall of the crucible

Besides slag area, the droplet area changes as well as the product phase(s) formed during high-temperature experiments were carefully studied. The results are presented and discussed separately below for different slag/matte samples of A to D.

4.3.2. a. Slag/matte sample quenched from 1400 °C

An optical microscopy image of the cross-section of the slag/matte sample quenched from 1400 °C is presented in Figure 4.23a. Slag area, copper sulphide droplet (gray area), copper phase produced (yellow area) as well as the gas halo formed around the droplet are illustrated in this photo. The sample was quenched at 2 minutes after the time at which the droplet first touched the slag after free-fall from the tip of the alumina delivery tube. At that time as it was also shown earlier in the section related to X-ray fluoroscopy images, the droplet was at the bottom of the alumina crucible, which is also marked in the photo.

The droplet looks elliptical and a gas halo can clearly be seen around the droplet. The thickness of the halo is very low around the lower part of the droplet and it gradually becomes thicker as we further move upward to the top of the droplet. This is explainable and is due to the lower density of the gas phase and thus its tendency to go higher, as well as probably because of the limited slag/matte droplet contact area near the crucible and thus slower kinetics of the desulphurization reaction.

The thickness of the gas halo was variable in different locations but it was measured to be 45 to 55 μm at the upper half of the droplet in different samples. An example of the gas halo thickness measurements for sample B (quenched from 1425°C) is illustrated in Figure 4.27c.

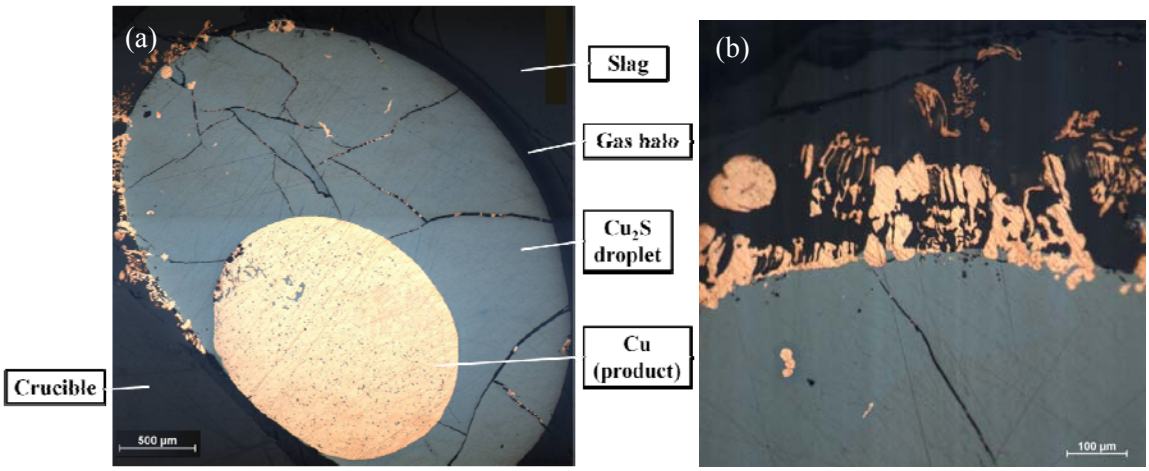

Figure 4.23 – Optical microscopy images of the cross-section of the slag/matte sample quenched from 1400 °C. Different areas are illustrated in the image. Sample was polished using water and no etching was applied.

In Figure 4.23a, a large yellow product phase as well as some small areas with similar colour (especially in the left-hand side of the photo adjacent to the slag/matte droplet boundary) [more clear in Figure 4.23b] can be seen that have been formed because of desulphurization reaction happening. EDS results confirmed that these yellow areas are in fact largely composed of copper (95-96 wt%) [Figure 4.25]. There are some small gray

areas in the yellowish copper area that was proved by EDS analysis to be some unreacted copper sulphide remained from the droplet.

Optical microscopy, SEM images as well as EDS results obtained from slag/matte sample A (quenched from 1400 °C) are shown below in Figures 4.24 to 4.26.

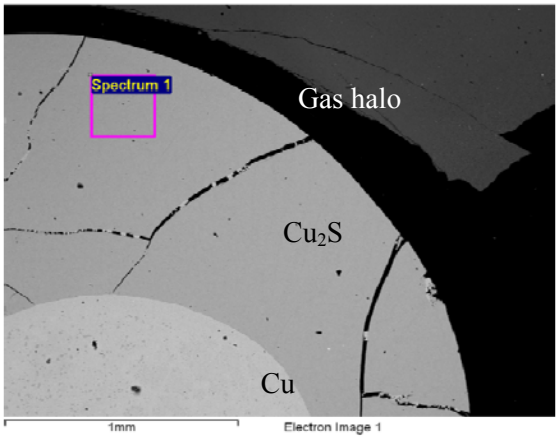

O	2.6
S	25.4
Fe	9.5
Cu	62.6

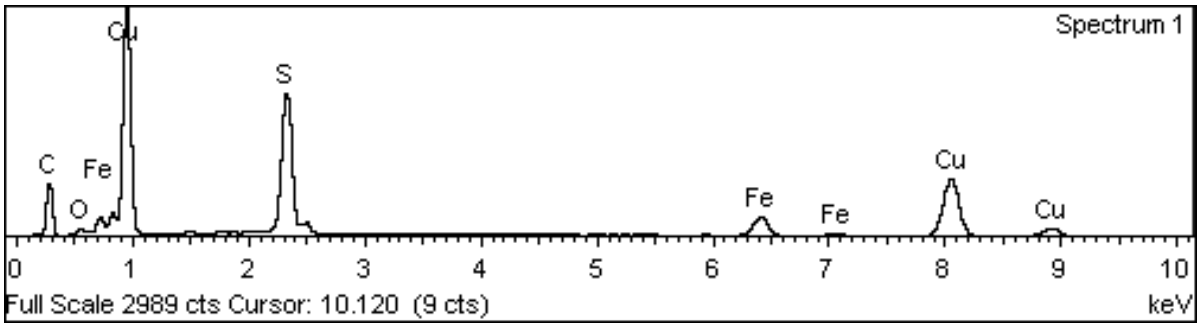

Figure 4.24 – SEM micrograph as well as EDS results obtained from the copper sulphide droplet area. Results are for the slag/matte sample quenched from 1400 °C (sample A) and the data presented in the small table are in wt%.

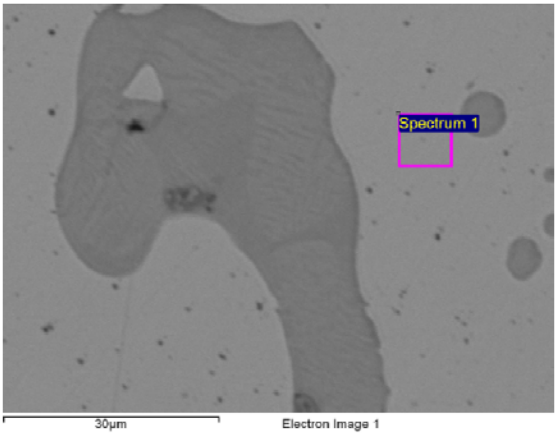

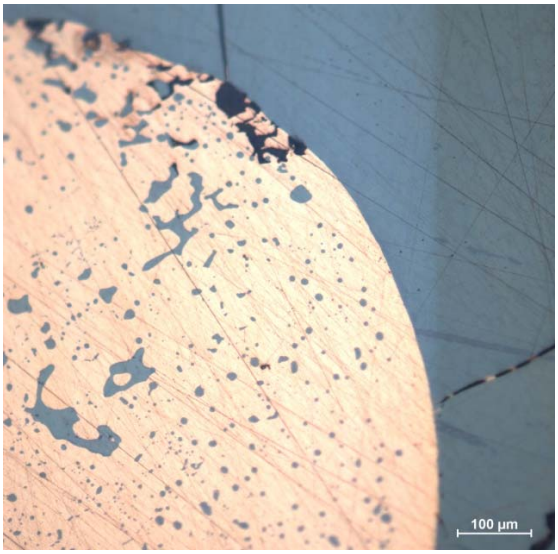

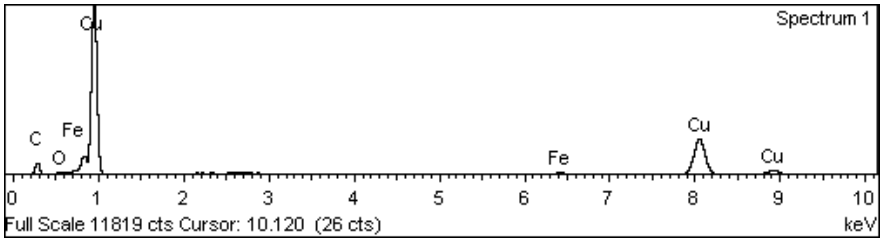

O	1.8
Fe	1.6
Cu	96.6

Figure 4.25 – Optical microscopy and SEM images of the yellowish area of copper produced as well as EDS results obtained from the smaller dark areas inside the copper phase are presented. Small dark areas are remaining unreacted copper sulphide. Results are for the slag/matte sample quenched from 1400 °C (sample A) and the data presented in the small table are in wt%.

In Figure 4.24 related to EDS results obtained from copper sulphide droplet area of sample A, it is seen that characteristic X-ray peaks corresponding to copper (62.6 wt%) and sulfur (25.4 wt%) are dominant. In addition, low amounts of Fe (9.5 wt%) and O (2.6 wt%) are detected in this area. Given the semi-quantitative nature of EDS, the results obtained are in good agreement with the theoretical content of copper in Cu_2S (80 wt%).

The presence of Fe and O in this area is due to the diffusion of Fe^{2+} and O^{2-} from the slag to the reaction zone.

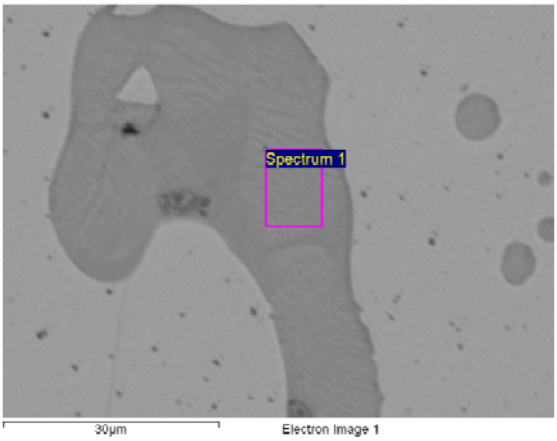

O	1.2
S	27.1
Fe	10.4
Cu	61.4

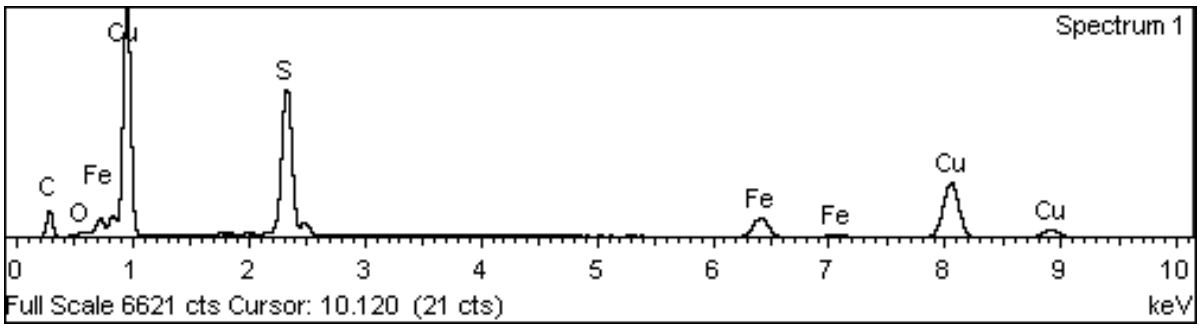

Figure 4.26 – SEM micrograph and EDS results obtained from the smaller dark areas inside the copper phase produced indicating the presence of some small remaining unreacted copper sulphide. Results are for slag/matte sample quenched from 1400 °C (sample A) and the data presented in the small table are in wt%.

EDS analysis results obtained from the copper yellowish area as well as a magnified optical microscopy image of this area showing the copper product with the presence of some dark areas inside are presented in Figure 4.25. EDS results showed that this

yellowish area is indeed mainly composed of copper with very low amounts of iron (1.6 wt%) and oxygen (1.8 wt%) present. No sulfur was detected in this area.

There are some dark areas present in the copper area in this sample that have been analyzed by means of EDS and the results are shown in Figure 4.26. Since copper and sulfur are the dominant elements, it is obvious that these areas are in fact Cu_2S remaining from the copper sulphide droplet and that they have not reacted to produce copper through the desulfurization reaction yet.

4.3.2. b. Slag/matte sample quenched from 1425 °C

Similar to the sample A, sample B (quenched from 1425 °C) was also analyzed by employing optical and scanning electron microscopy, the latter equipped with an energy-dispersive X-ray spectrometer (EDS). In Figure 4.27, optical microscopy images of the cross-section of the slag/matte sample B, are presented. In image (a), different areas of slag, copper sulphide droplet, copper product as well as the gas halo formed around the droplet in contact with slag are illustrated. Similar to what was seen in the optical images obtained for sample A, in this sample a clear gas halo could be seen in the photos and again similarly its thickness also here is seen to increase as we move upward toward the top of the droplet.

In image (d), a dome-like bubble is observed which is formed on top of the droplet as a result of reaction. This dome-like area was also previously seen clearly in X-ray

fluoroscopy images obtained from experiments performed using droplets with sizes equal to 0.75 or larger. It can be seen in Figure 4.1 (g) as well as Figure 4.2. The formation of this area is due to the accumulation of the product gas on the droplet surface as the desulphurization reaction occurs and goes forward once the copper sulphide droplet has entered the oxidizing slag. Since gas density is much lower than the molten slag or matte (copper sulphide droplet), the accumulated gas molecules produced on the surface of the droplet start to move upward, creating that dome-like bubble. The bubble eventually leaves the droplet and moves upward until it joins the furnace atmosphere. Subsequently, a new dome starts to form and replace the previous one and it was recorded in the fluoroscopy videos captured during performing the high-temperature experiments.

As shown in image (c), the thickness of the gas halo close to the upper half of the droplet was measured and it was approximately equal to 50 micron. The gas halo thickness varies in different locations and it gets thinner as we go further down from the top of the droplet and get closer to the crucible bottom. The reason for this phenomenon was explained before.

A magnified picture of the copper sulphide droplet and the copper yellowish area produced because of the reaction is presented in Figure 4.27.b. Some very small spots could be detected in the copper area in this photo. Some of these small spots were proven by EDS to be in fact remaining unreacted copper sulphide and the rest are holes that might have been formed either due to polishing during the sample preparation prior to structural analysis, or possibly because of gas produced as a result of desulphurization reaction happening.

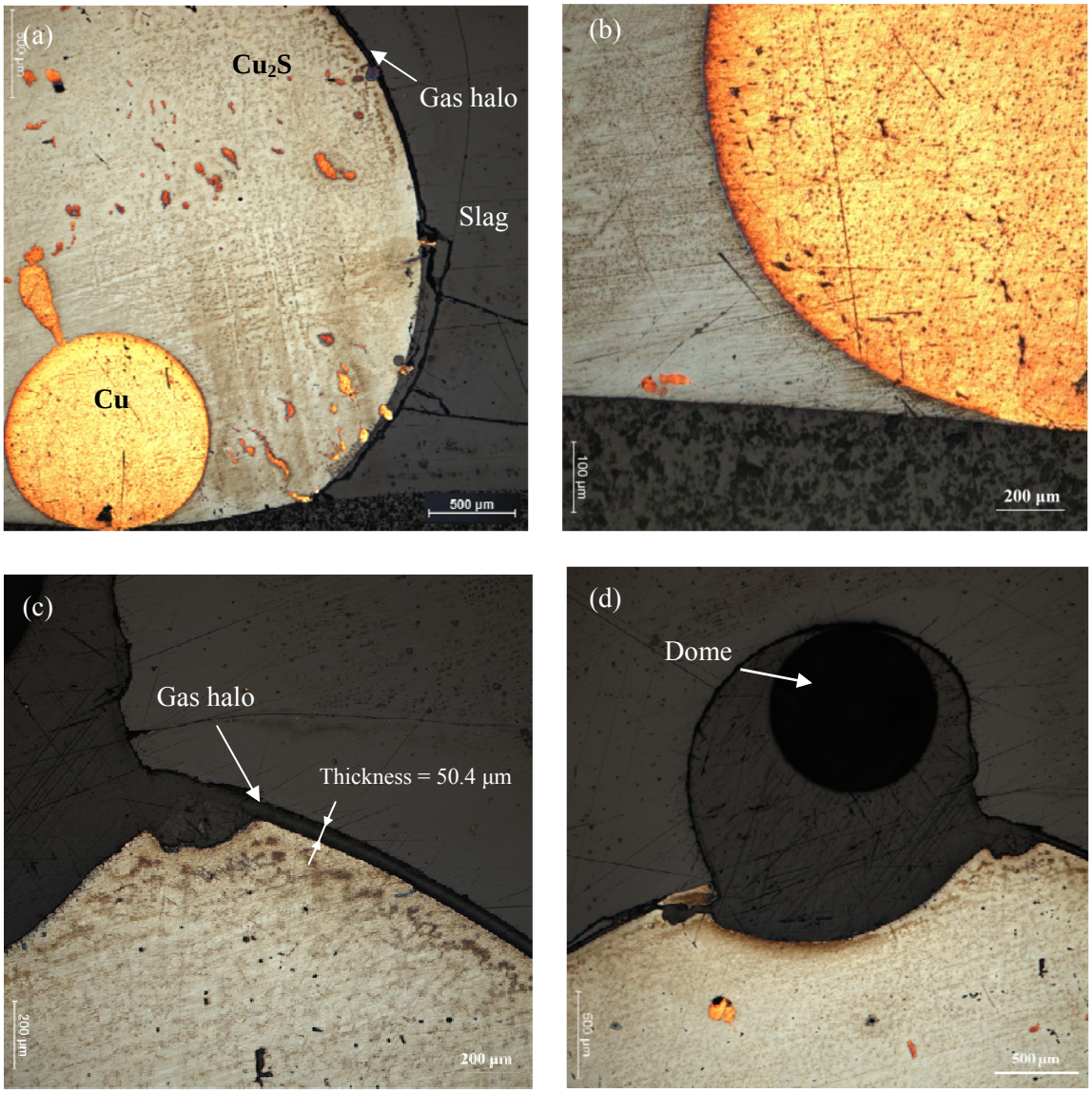

Figure 4.27 – Optical microscopy images of the cross-section of the slag/matte sample quenched from 1425 °C. Different areas of slag, copper sulphide droplet, copper product as well as the gas halo formed are illustrated in the images. In image d, a dome-like gaseous area (bubble) on top of the droplet is formed. Sample was polished using water and no etching was applied.

In Figure 4.28, X-ray fluoroscopy photos taken 2 minutes after the droplet entered the slag are presented. The experiment was conducted at 1425 °C and using a 0.75 g droplet. This means that exactly the same experimental parameters that was followed to prepare the quench sample and then to take slag/matte photos presented in Figure 4.27, was also used here and the photos are presented for comparison.

In Figure 4.28, droplet is much darker than slag and similar to what was observed before in optical microscopy image of the quenched slag/matte sample in Figure 4.27 d, a white dome-like area on top of the droplet is also seen here. The bubble on top of the droplet in Figure 4.28, formed on the droplet surface as the reaction proceeded and then moved upward to the upper half and then top of the droplet.

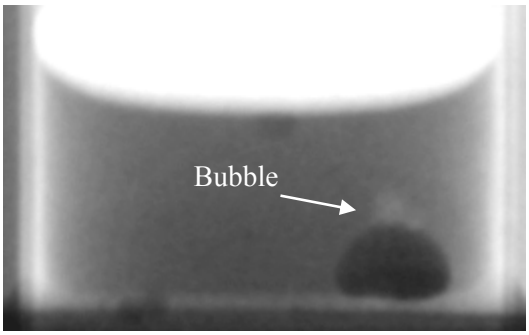

Figure 4.28 – X-ray fluoroscopy photo extracted from the movie recorded during the experiment conducted using a Cu_2S droplet size of 0.75 g at 1425 °C. The photo was taken 2 minutes after the time at which the droplet touched the slag for the first time after the free-fall (t=2 min).

In Figure 4.29, EDS analysis results obtained from two different areas of copper sulphide (top graph and table) as well as the yellowish copper area produced in sample B (quenched from 1425 °C) are presented. EDS results confirmed that the main elements in Cu_2S area were indeed Cu (66.2 wt%) and S (24.0 wt%) and the dominant element in the copper yellowish area as expected was Cu (95.4 wt%).

Low amounts of iron and oxygen were also present in the copper sulphide droplet (Fe=5.2 wt% and O=4.5 wt%) as well as the copper (Fe=0.6 wt% and O=4.1 wt%) areas. No sulfur was detected in the latter area.

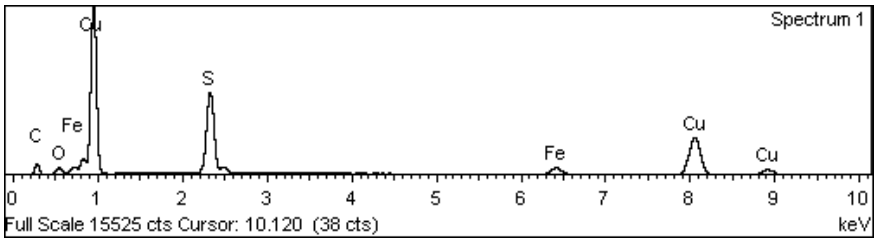

O	4.5
S	24.0
Fe	5.2
Cu	66.2

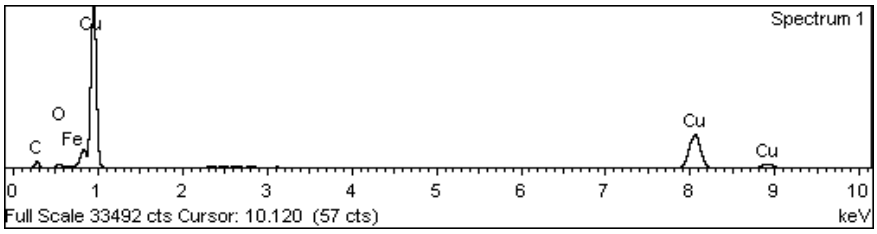

O	4.1
Fe	0.6
Cu	95.4

Figure 4.29 – EDS results obtained from the copper sulphide area (top photo and table) as well as the data obtained for the copper phase produced. Results are for the slag/matte sample quenched from 1425 °C (sample B) and the data presented in the small table are in wt%.

In optical microscopy images of slag/matte samples quenched from 1400 (sample A) and 1425 °C (sample B), the large copper yellowish product could be observed as a close-to-spherical area located in the lower half of the matte droplet and close to the bottom of the crucible. This phenomenon of the copper product sinking to the bottom the crucible might have been due to much higher density of copper (8.96 g/cm^3) compared to copper sulphide (5.6 g/cm^3) and slag (measure to be about 3.7 g/cm^3).

Given the reaction rate results presented earlier in this chapter and given the fact that most of the reaction happened during the first few seconds after the droplet touched the oxidizing slag and the reaction considerably slowed down after the formation of gas halo, it appears that the copper yellowish area observed in quenched samples A and B is a direct result of the reaction happening during the first few seconds starting from the interfacial area of copper sulphide droplet and slag and as explained above, copper sinking to the bottom of crucible due to its higher density.

4.3.2. c. Slag/matte sample quenched from 1450 °C

In Figure 4.30, optical microscopy images of the cross-section of the slag/matte sample quenched from 1450 °C (sample C) at time=2 minutes are presented. The micrographs are shown at different magnifications. Compared to samples A and B, the droplet in this case as well as the sample D, look larger and thus it was not possible to have the whole area of the droplet/slag in the optical microscopy image with the lowest magnification (scale bar 500 micron). A quarter of the whole matte droplet/slag area is shown in image (a) in

Figure 4.30, but the other quarters looked similar under the microscope, as there was a good symmetry present in this sample and in contrast to the two previously analyzed samples, no specific copper product area could be detected in this sample.

However, similar to previous samples, it is clear in the micrographs obtained from this sample that a gas halo with an approximate thickness of about 50 micron was formed around the droplet at the interface of matte droplet and slag.

By taking a detailed look at image (a) as well as image (b) in this figure, it appears that some large gray areas have been formed in the droplet near the matte droplet/slag interface as well as inside the droplet itself. The gray areas near the matte droplet/slag interfacial area looks continuous compared to the gray areas inside the droplet that look more dispersed. EDS results performed on these areas revealed that they are highly rich in Fe with contents as high as 87.5 wt%, and low amounts of copper (5.3 wt%), oxygen (1.7 wt%), sulfur (0.7 wt%) as well as some very low amounts of impurities such as phosphorous, nickel and arsenic are also present. The results from EDS are presented in more detail in Figure 4.31. These results clearly show that iron ions and oxygen (O^{2-}) have dramatically diffused into the droplet with oxygen atoms having an easier time to travel in the copper sulphide crystal structure due to their smaller size compared to Fe atoms.

Since the slag had high amounts of silicon content and as no silicon was detected in the EDS analysis results of different areas in the microstructure including the Fe-rich areas, the assumption that presence of gray Fe-rich areas in the microstructure might have been

due to slag entrainment into the droplet could not be verified and consequently the only justifiable assumption could be intense diffusion of iron along with oxygen from slag to matte droplet. In addition, the origin of impurities (P, Ni, As) in Fe-rich areas is not clear but given the high purity of raw materials used to synthesize fayalite slag, they might have originated from low amounts of alumina that was dissolved in the slag to form spinel. They might have come along with Fe from slag to the droplet. This is in good agreement with EDS analysis results, which showed the presence of impurities wherever Fe content was high in the microstructure (e.g. Figure 4.31).

Furthermore, there were some yellowish areas present in the microstructure and can clearly be seen in image (c) of Figure 4.30. These yellowish areas were proven to be mainly composed of copper. EDS analysis performed on these areas gave different results depending on the size of the area. EDS results showed that tiny yellowish areas in the microstructure had lower content of copper but higher content of iron compared to the larger yellowish areas. Their oxygen content was very close and no sulfur was detected in these areas. The details of EDS analysis results for yellowish areas with different sizes in sample (C) are shown in Table 4.6.

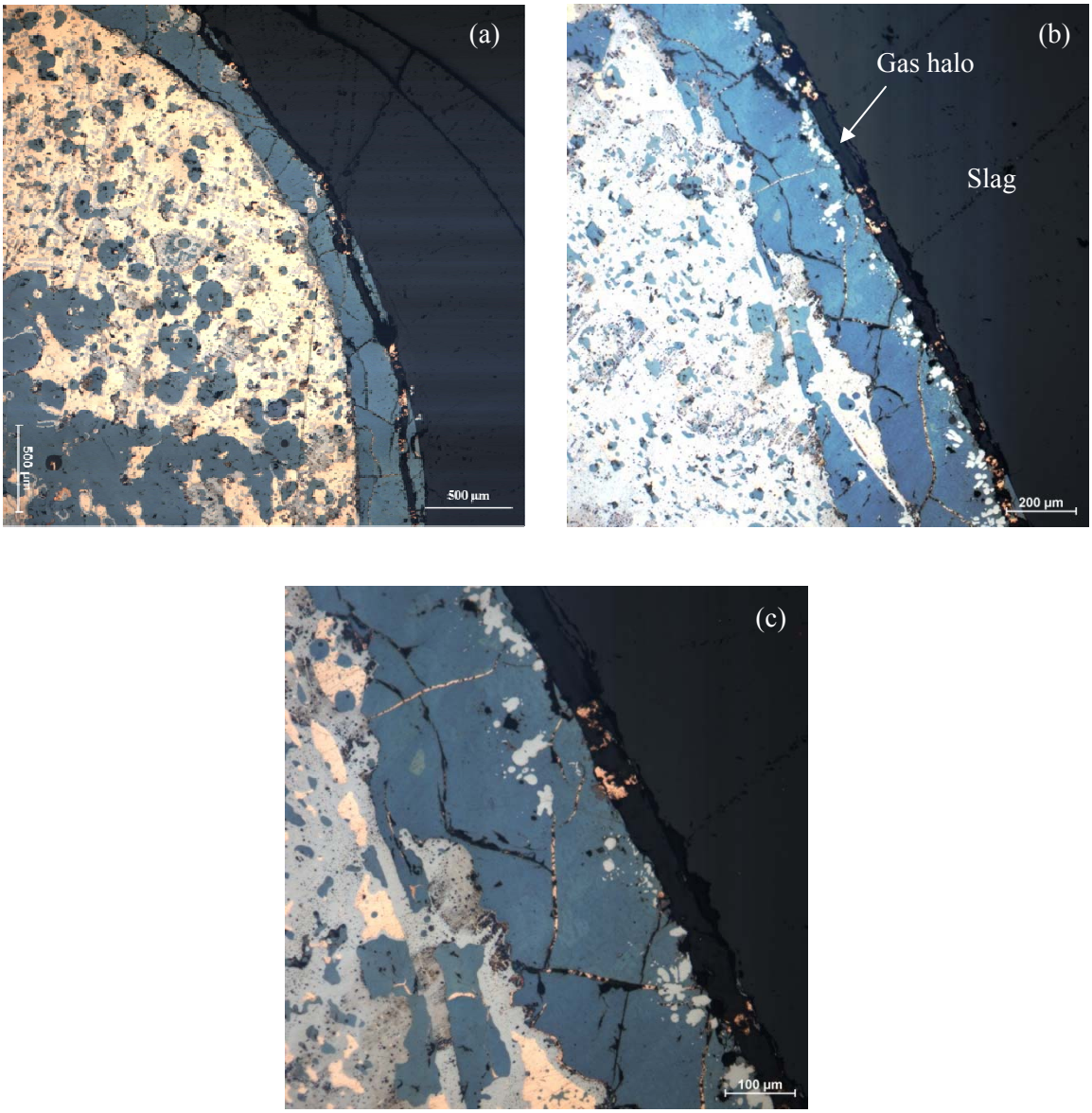

Figure 4.30 – Optical microscopy images of the cross-section of the slag/matte sample quenched from 1450 °C. Three images of the microstructure taken at different magnifications are shown in this figure. Sample was polished using water and no etching was applied

Fe	87.5	P	2.3
Cu	5.3	As	1.8
O	1.7	Ni	0.7
S	0.7		

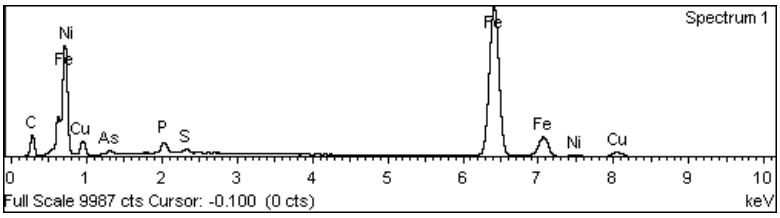

Figure 4.31 – EDS spectra obtained from the Fe-rich areas in the slag/matte sample quenched from 1450 °C (sample C). Data presented in the small table are in wt%.

Table 4.6 – EDS analysis results (wt%) obtained from Cu-rich areas in sample C (quenched from 1450 °C).

Element / Sample	Cu	S	Fe	O	P	Ni	As
C (Cu-rich areas)	84.1(small areas)	0	11.9	2.7	0.8	-	0.7
	93.3 (large areas)	0	3.7	2.4	-	-	0.6

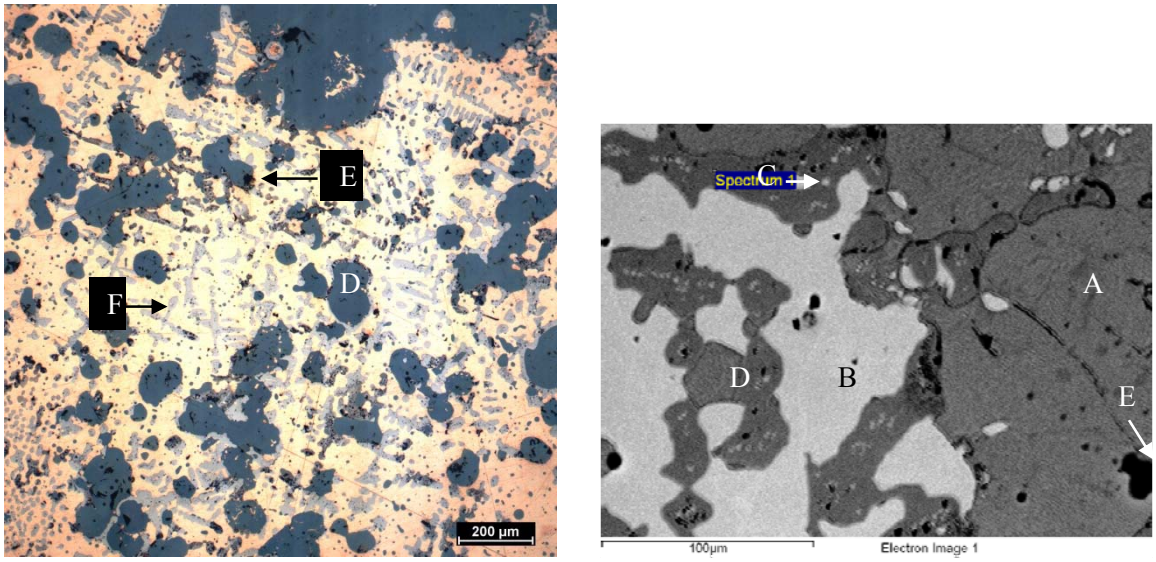

Figure 4.32 – Optical microscopy and SEM images of the cross-section of slag/matte sample quenched from 1450 °C (sample C). Different areas are illustrated in these photos; areas are: (A) copper sulphide droplet area, (B and C) copper-rich areas, (D) Fe-rich areas and (E) example of presence of holes in the microstructure.

In Figure 4.32, optical microscopy as well as scanning electron microscopy images of the middle area of the slag/matte sample quenched from 1450 °C (sample C) at time 2 minutes after the time at which matte droplet size 0.75 gram touched the slag for the first time are presented. In the optical microscopy image in this figure, almost five areas with different color can be identified. In the left and left top portion of the photo, those yellowish areas are mainly made of copper resulting from the desulphurization reaction going forward. Large gray areas marked by letter D are Fe-rich areas.

The background is remaining copper sulphide. The small but darker areas in the background and marked by letter F in the microstructure are also remaining copper sulphide but EDS results showed that they have higher content of Fe (about 11.4 wt%). In addition to copper (59.3 wt%) and sulfur (27.9 wt%), there were also low amounts of oxygen (about 1.4 wt%) present in the remaining copper sulphide areas in this sample. The fifth area that can be identified in these photos are small black and usually circular areas that are shown by letter E. These are holes and are either due to gas formation as a result of desulphurization reaction or are due to polishing. Although the former is more likely especially for those circular black areas present near the copper-rich areas.

Different areas of copper sulphide (areas shown by letter A), copper-rich (areas shown by letters B and C), Fe-rich (area shown by letter D) as well as a hole (shown by letter E) are illustrated in the scanning electron microscopy image presented in Figure 4.32. The reason for showing Cu-rich areas by two different letters B and C, is that EDS results showed that larger copper-rich areas (shown by letter B) had higher content of copper and lower content of iron compared to smaller copper-rich areas (shown by letter C) and the details were presented earlier in Table 4.6.

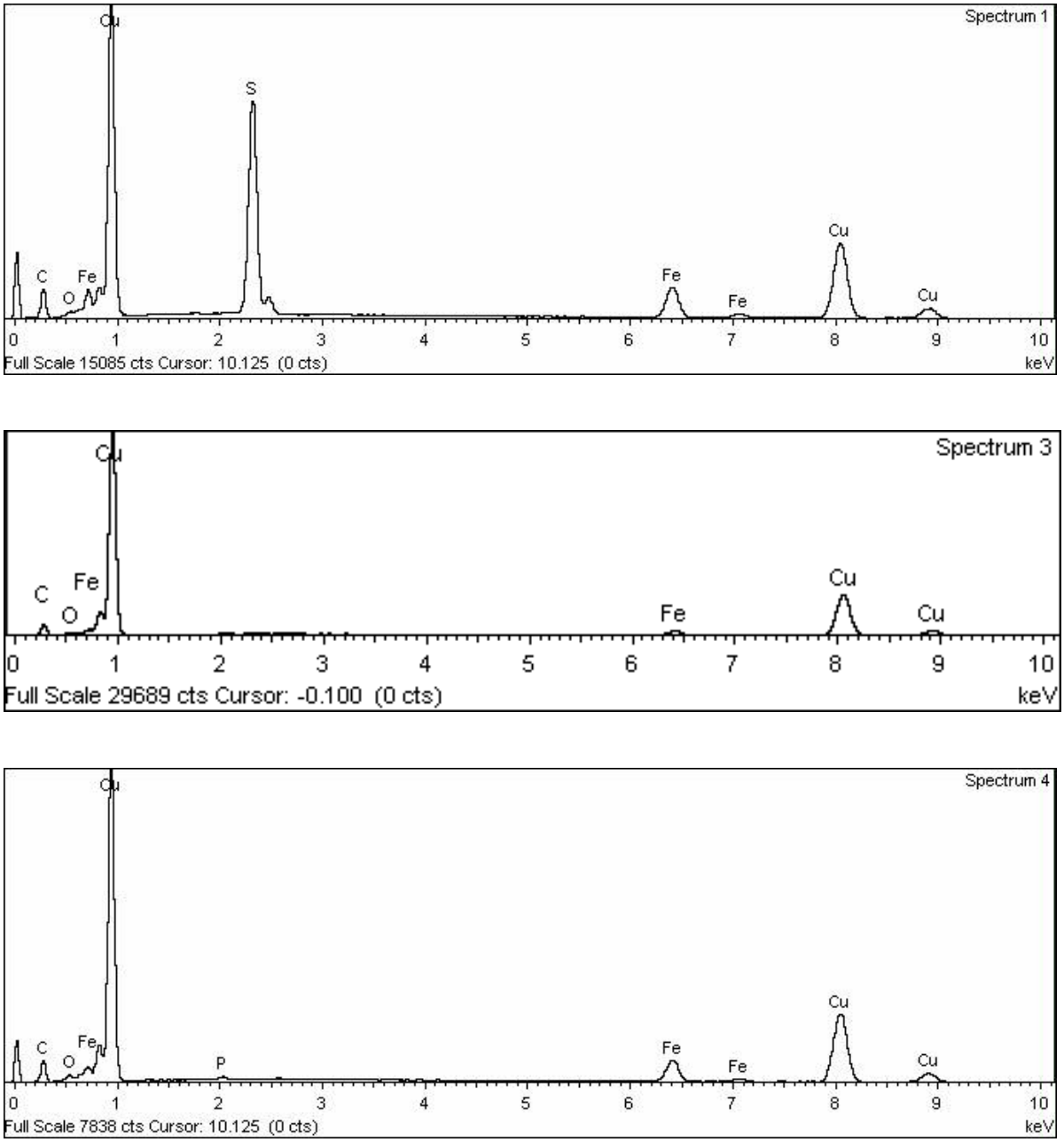

Figure 4.33 – EDS spectra obtained from different areas in the slag/matte sample quenched from 1450 °C (sample C). The spectra from top to bottom are for copper sulphide area, larger Cu-rich areas as well as smaller Cu-rich areas (mainly seen forming inside the Fe-rich areas), respectively.

An example of the EDS spectra obtained from Fe-rich areas (shown by letter D in Figure 4.32) was presented in Figure 4.31. In Figure 4.33, EDS spectra obtained from areas shown by letters A (copper sulphide), B (larger Cu-rich) as well as C (small Cu-rich areas) have been presented. The elemental analysis results were mentioned earlier in Table 4.6).

4.3.2. d. Slag/matte sample quenched from 1475 °C

The last slag/matte sample, which was analysed by means of optical microscopy as well as EDS analysis, was the one quenched from 1475 °C (sample D). Similar to the previous cases, this sample was also quenched at time=2 minutes after the droplet fell inside the oxidizing fayalite slag.

Optical microscopy images with different magnifications taken from this sample after quenching are presented in Figure 4.34. Again, no etching was applied on sample. Similar to the previous samples, a narrow gas halo is seen in the photos; forming around the droplet with a strip of Fe-rich area just neighboring the matte droplet/gas halo/slag interfacial area. Similar to sample (C) and in contrast to samples A and B, no large copper area can be seen in the micrographs, but instead it appears that copper-rich and Fe-rich areas are distributed inside the matte droplet.

In order to better understand the phenomena happening during the high-temperature experiment as well as to identify the phases present in the micrographs, EDS analysis was

applied on the quenched sample. In Figure, 4.35, two SEM images obtained from sample D are presented (images 1 and 2). The second image in this figure is the magnified image taken from the specific area shown in the first image. This specific area is marked by a dotted rectangle and an arrow was used to indicate that the second image is indeed a magnified image of that area. Additionally, there is a third image presented in this figure that is actually the first image but with some adjustments applied on the photo to increase the contrast so that a specific phase (copper sulphide) marked by asterisk in the photo could be observed better and easier.

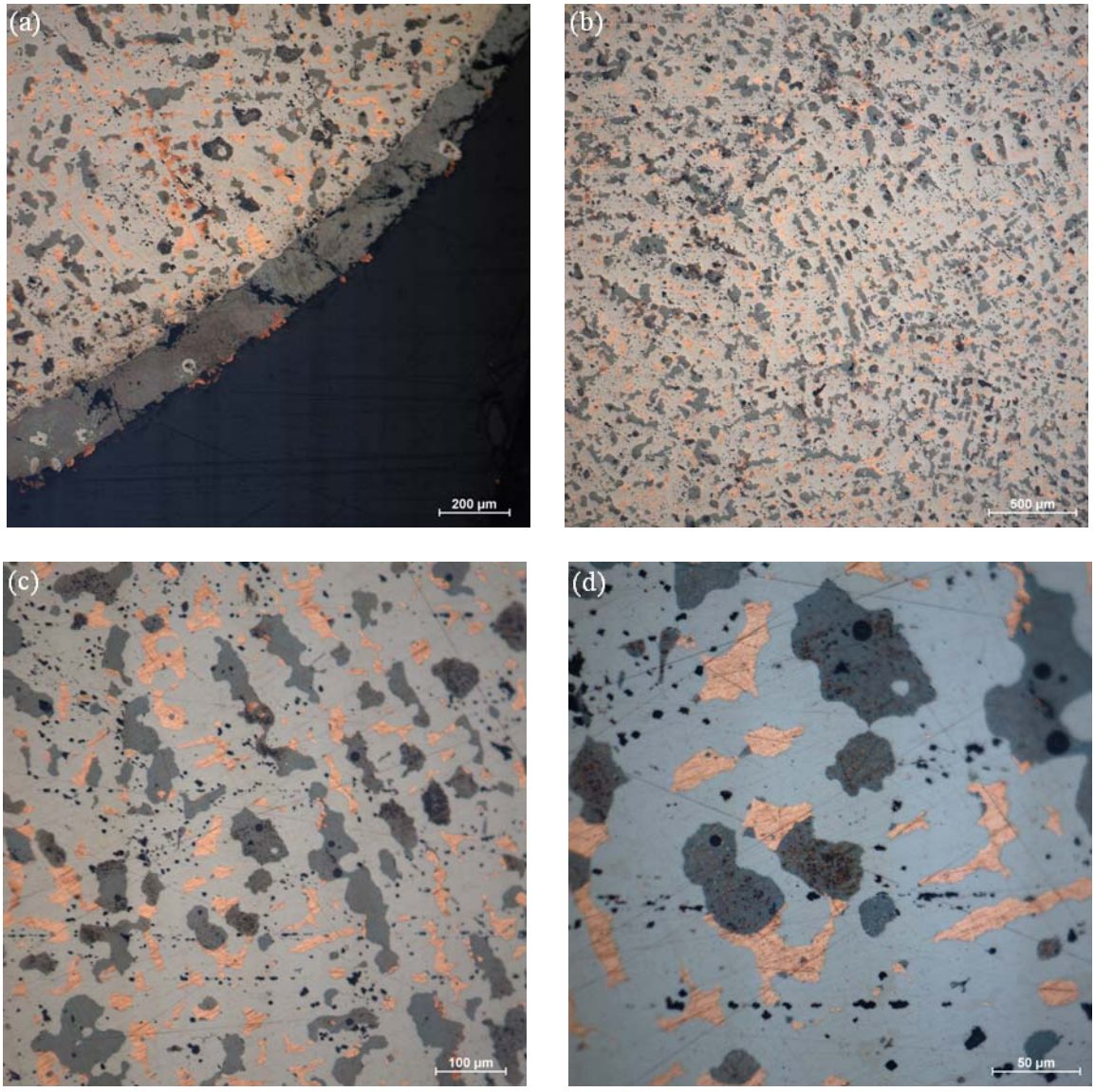

Figure.4.34 – Optical microscopy images of the cross-section of the slag/matte sample quenched from 1475 °C. Four images of the microstructure taken at different magnifications are shown in this figure. Sample was polished using water and no etching was applied.

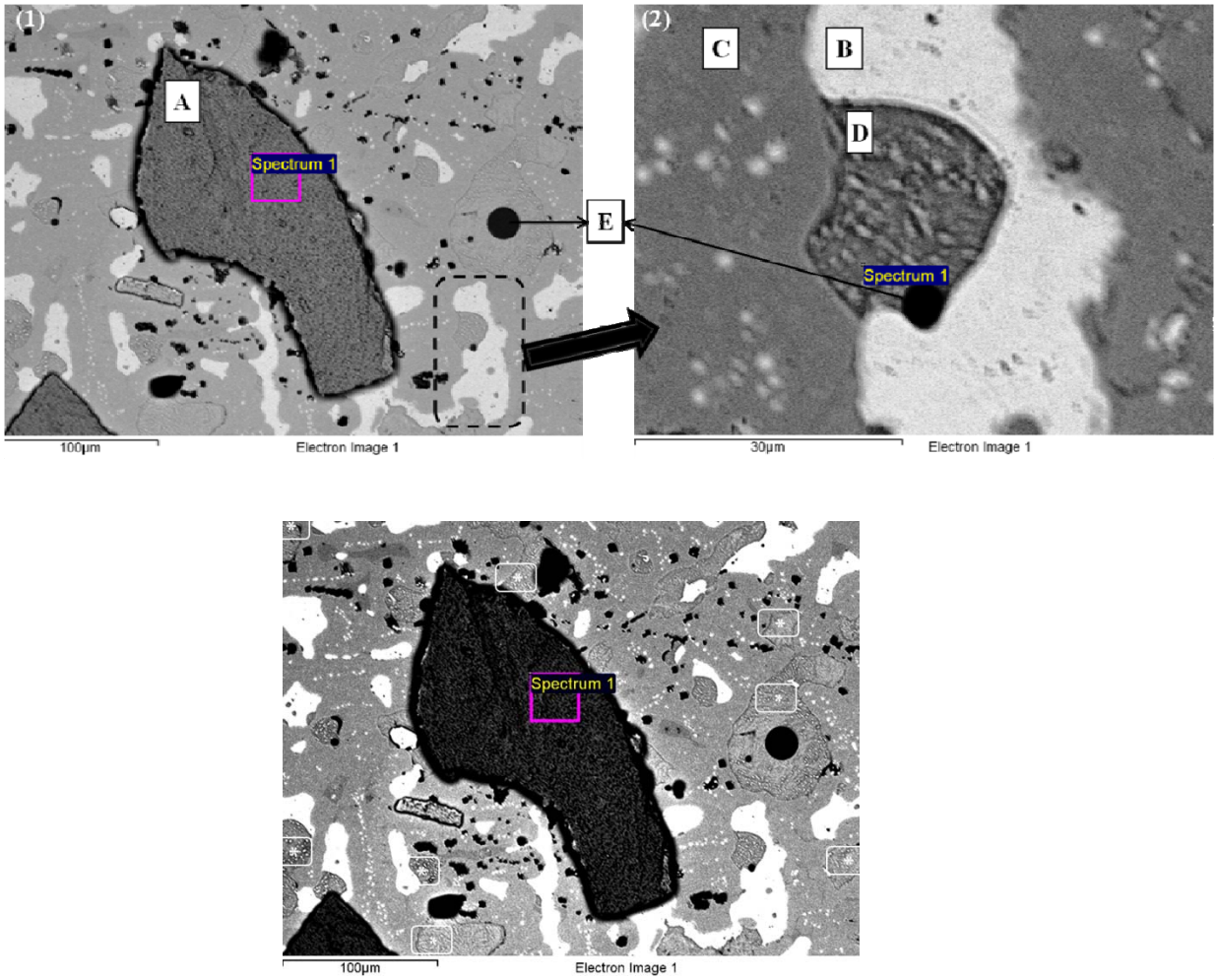

Figure 4.35 – SEM images of the cross-section of slag/matte sample quenched from 1450 °C (sample C). Different areas are illustrated in these photos; areas are: (A) copper-rich area with high oxygen content, (B) copper-rich area, C), Fe-rich area, (D) remaining copper sulphide and (E) example of presence of holes in the microstructure.

In general, optical microscopy observations as well as EDS analysis results revealed that excluding the slag phase and the gas halo area, five major areas (phases) composed the bulk of this quenched sample, marked by letters A to E in Figure 4.35. These areas were:

- A) Copper-rich area with high oxygen content (as high as 20-21 wt%). These observations suggested that copper oxides of mainly CuO have been formed, something that was not seen before.
- B) Copper-rich area with similar Fe and O content to the Cu-rich areas in previous samples but with slightly larger Fe content (4.5 wt%)
- C) Fe-rich area with iron content as high as 91 wt% but with low content of Cu (3 wt%) and some impurities (P, As, Ni), which were also seen to be present in sample C.
- D) Remaining copper sulphide droplet with high amounts of iron content (as high as 12.4 wt%).
- E) Some black areas. Specifically those with circular shape are supposedly formed because of gas formation during the desulphurization reaction.

EDS spectrums obtained from different areas A to D are presented in form of four images in Figure 4.36.

Fe-rich areas along with Cu-rich areas appear to dominate the microstructure in this sample. In addition, some areas of copper sulphide remaining from matte droplet could be seen in the micrographs, which for better observation have been marked by asterisk in the third image in Figure 4.35. Depending on the location where the EDS analysis was performed, different copper and sulfur content was obtained for the remaining copper sulphide areas. Their copper and sulfur content was in the range of 59.1-65.6 wt% and 22.8-26.8 wt%, respectively. Furthermore, Fe content in these areas was much higher

than the content in similar areas of previous samples and it was varied between 9.5-12.4 wt%.

EDS analysis results showed that in general, Fe content of all the areas in this sample was higher than the previous samples. This finding presumably could be due to increased diffusion and dissolution of iron and O^{2-} from the slag into the droplet because of higher experimental temperature employed for this sample. Temperature also reduces the viscosity of the slag. This increased diffusion might also be the reason why we have witnessed increased oxygen content in some areas to such extent that large Cu-rich areas with very high oxygen content could be seen in the microstructure (area A in Figure 4.35). In fact, oxygen content in these larger areas could match the theoretical oxygen content of CuO (20 wt%).

Studying the binary phase diagram of Cu-O revealed that the melting point of copper oxide phases CuO (1230 °C) as well as Cu_2O (1232 °C) was much lower than the experimental temperature in these studies and thus presumption that these Cu-rich areas with high content of oxygen might be solid was rejected.

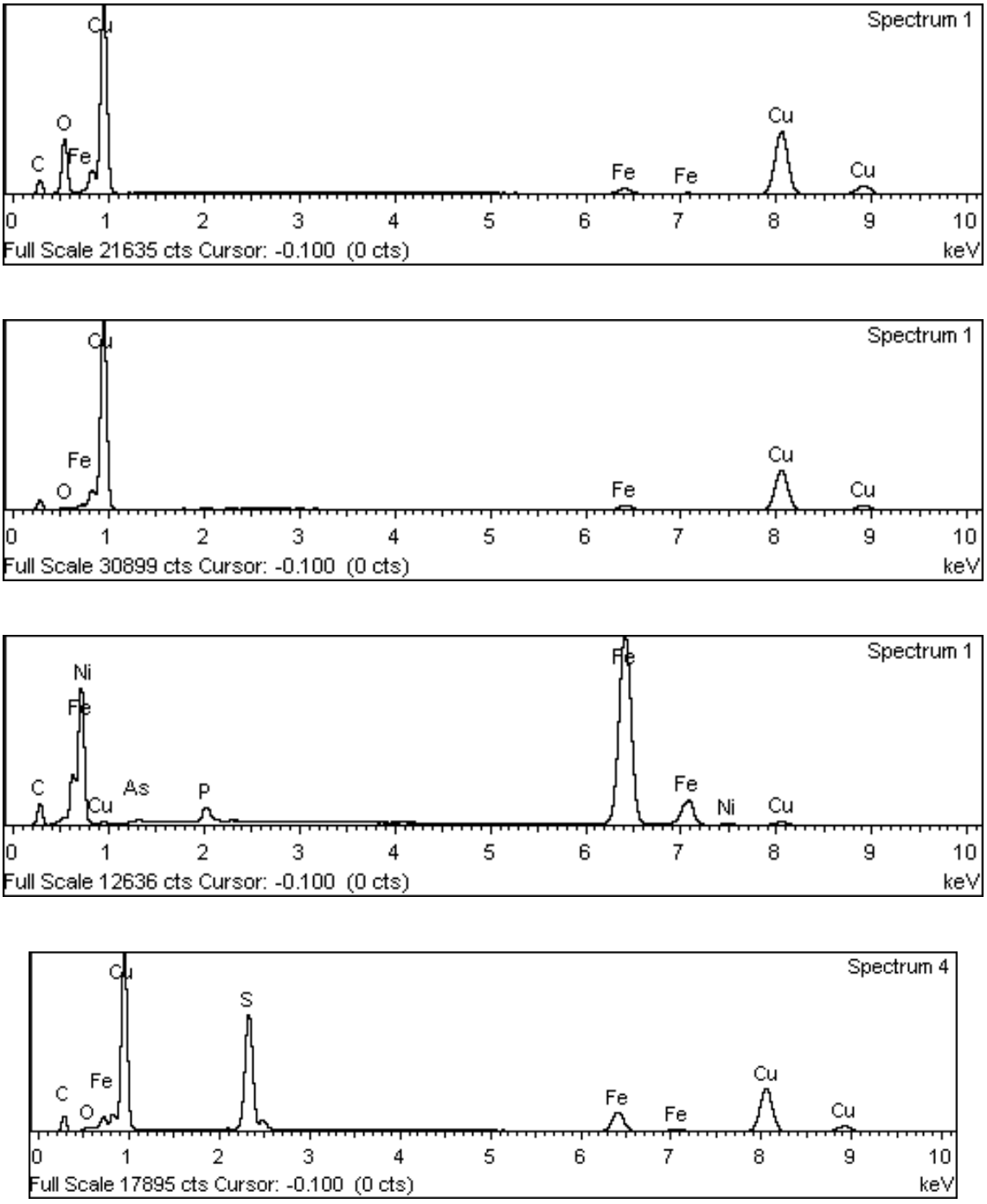

Figure 4.36 – EDS spectra obtained from different areas in the slag/matte sample quenched from 1475 °C (sample D). The spectra from top to bottom are for Copper-rich areas with large oxygen content (21.8 wt%), Copper-rich areas, Fe-rich areas, remaining copper sulphide areas, respectively.

Regarding Fe-rich areas and given their very high content of iron (as high as 90 wt%) as well as its higher melting point (1538 °C) compared to the experimental temperatures here, one might argue that these areas might be solid. This could be a valid point if there were no impurities present in these areas. However, consulting the Fe-P and Fe-As phase diagrams as well as taking into account the presence of P and As in Fe-rich areas with contents as high as 2.7 and 1 wt% respectively, it could be concluded that the melting point of iron dramatically decreases to below the experimental temperature used here. Therefore, Fe-rich areas identified in samples C and D could not be in solid state.

4.3.3. Summary of structural analysis results

Comparing optical microscopy images obtained from slag powder mixture with those obtained for synthesized slag, revealed that the microstructure was completely transformed and magnetite as well as fayalite were the two main phases.

Titration results revealed that no metallic iron was present in the slag and Fe^{2+} and Fe^{3+} in the slag were equal to 35.5 and 17.5 wt%, respectively. XRD performed on the quenched synthesized slag confirmed the previous findings that fayalite, silica as well as magnetite were the major phases available in the slag. No peak corresponding to Fe or hematite was detected by XRD.

Structural analysis by means of optical microscopy as well as scanning electron microscopy coupled with energy dispersive X-ray spectrometry (EDS) was performed on

matte droplet/slag samples quenched from different experimental temperatures (1400-1475 °C). Copper sulphide matte droplet size equal to 0.75 gram was used in all the quenching experiments. EDS analysis results obtained from different areas on the samples are presented in Tables 4.7 to 4.9.

Table 4.7 – EDS analysis results (wt%) obtained from copper sulphide (Cu_2S) droplet areas in samples quenched from different high-temperatures (A, B, C and D correspond to temperatures 1400, 1425, 1450 and 1475 °C, respectively).

Element / Sample	Cu	S	Fe	O
A	62.6	25.4	9.5	2.6
	61.4	27.1	10.4	1.2
B	68.0	23.8	4.9	3.4
	66.2	24.0	5.2	4.5
C	59.3	28.0	11.4	1.4
D	60.0	26.1	12.0	1.9
	59.1	26.8	12.4	1.9
	65.6	22.8	9.5	2.1

Table 4.8 – EDS analysis results (wt%) obtained from Cu-rich areas in samples quenched from different high-temperatures (A, B, C and D correspond to temperatures 1400, 1425, 1450 and 1475 °C, respectively).

Element / Sample	Cu	S	Fe	O	P	Ni	As
A	96.6	0	1.6	1.8	-	-	-
	94.9 (closer to boundary)	0.8	2.0	2.4	-	-	-
B	95.4	0	0.6	4.1	-	-	-
C	84.1(small, in Cu_2S area)	0	11.9	2.7	0.8	-	0.7
	93.3 (large areas)	0	3.7	2.4	-	-	0.6
	77.2 (small in slag)	0	2.9	19.6	-	-	-
D	75.7 (larger areas)	0	2.5	21.8	-	-	-
	93.61 (smaller areas)	0	4.5	1.9	-	-	-

Table 4.9 – EDS analysis results (wt%) obtained from Fe-rich areas in samples quenched from different high-temperatures (A, B, C and D correspond to temperatures 1400, 1425, 1450 and 1475 °C, respectively).

Element / Sample	Cu	S	Fe	O	P	Ni	As
A	-	-	-	-	-	-	-
	-	-	-	-	-	-	-
B	-	-	-	-	-	-	-
C	5.3	0.7	87.5	1.7	2.3	0.7	1.8
	5.5	0.1	86.8	3.1	2.6	0.6	1.4
D	3.7	-	90.8	1.4	2.4	0.7	1.0
	3.0	-	91.0	1.7	2.7	0.6	1.0

The following is a summary of results obtained from structural analysis observations performed on different quenched samples:

1. A gas halo could be seen around the matte droplet in all the samples. Thickness of the gas halo varies and it gradually increases as we move upward and get closer to the top of the droplet. A dome-like bubble on top of the matte droplet could be seen in the micrographs, which was in agreement with X-ray fluoroscopy observations in experiments using matte droplets equal to 0.75 gram and larger.

The thickness of the gas halo in the upper-half of the matte droplet was measured to be roughly 45 to 55 microns.

2. Slag elemental analysis confirmed that O, Si as well as Fe were the main elements existing in the slag and their contents in different samples were consistent and in general agreement with the theoretical values calculated from the mass of material used to synthesize the slag. In addition, some low Al (3.4-5.7 wt%) and Mn (2.4-3 wt%) content was present in slags. The origin of these unexpected elements presumably was from the alumina crucible due to its tendency to react with FeO in slag to form spinel ($FeAl_2O_4$) in high temperatures used in this study.
3. Microscopic observation revealed that there were areas with very high amounts of Cu (up to 94-97 wt%) inside the copper sulphide matte droplet area. These Cu-rich areas formed as the desulphurization reaction happened. In addition, in microscopy images of the samples A and B (quenched from 1400 and 1425 °C, respectively), a large Cu-rich area could be observed. It was found that the copper product sank to the lower half of the matte droplet at the bottom of the crucible apparently due to its much higher density (8.96 g/cm^3) compared to slag (measured to be about 3.7 g/cm^3) or copper sulphide matte droplet (5.6 g/cm^3). In contrast, in sample C and D (quenched from 1450 and 1475 °C, respectively), no one-piece large Cu-rich area could be identified, but rather it appeared that they were distributed everywhere inside the matte droplet. Furthermore, no sulfur was detected in the Cu-rich product areas. Fe as well as O content in Cu-rich areas increased as higher experimental temperatures was applied.

4. Remaining unreacted copper sulphide was detected in all the samples indicating that the desulphurization reaction was incomplete.
5. Although no Fe-rich areas could be detected in samples A and B, there were some areas with very high amounts of Fe (as high as 88-91 wt%) inside the matte droplet of samples C and D. The possibility that these Fe-rich areas were in fact slag entrapped in the matte could not be confirmed as silicon was not detected in the EDS analysis results. These Fe-rich areas not only had formed inside the matte droplet but also had formed a narrow strip neighboring the matte droplet/slag interfacial area, which gave rise to the presumption that they likely were formed due to diffusion and dissolution of iron and oxygen from the slag into the matte droplet. This argument was supported by the fact that some low amounts of impurities (P, As and Ni) were also detected in these areas, while they could not be detected anywhere else on the matte droplet. Almost no sulfur was detected in the Fe-rich areas
6. By comparing EDS analysis results obtained for different areas of copper sulphide and copper product in different samples, it can be concluded that Fe as well as O content in these areas increases with temperature. This increase could be mainly due to temperature dependence of diffusion of iron and oxygen ions from the slag to the matte droplet as well as a decrease in the viscosity of the slag. This increased diffusion could be attributed to formation of Fe-rich areas in samples C and D both inside the matte droplet as well as close to the slag/matte droplet interfacial area and formation of some large Cu-O-rich (O content as high as 22

wt%) areas in sample D (quenched from 1475 °C) [refer to Tables 4.8 and 4.7]. Compared to iron, oxygen atoms diffuse faster in copper sulphide crystal structure due to their smaller size. That is why a narrow strip of Fe-rich area with low content of O was formed close to the slag/matte interfacial area in samples C and D, while oxygen content inside was higher and formation of large Cu-rich areas with high content of O in sample D supported this argument.

7. Small black and usually circular areas could be observed in microscopy images of samples quenched from higher temperatures. These holes are formed either due to gas formation because of desulphurization reaction taking place or due to polishing during the sample preparation steps. The former speculation is more likely especially for those with circular shape, which were present near the copper sulphide as well as Cu-rich areas.

Chapter 5. Conclusions

The reaction kinetics of copper sulphide matte (Cu_2S) droplets with an oxidizing slag was investigated in this study. Silica-saturated fayalite ($2FeO.SiO_2$) slag was synthesized by melting powder mixtures of iron, silica and hematite with respective ratios of 1:2:3.6 at high temperatures. Experiments were performed in an inert atmosphere using a high-temperature furnace equipped with X-ray fluoroscopy and pressure transducer. The effect of temperature (1400 – 1475 °C) and matte droplet size (0.5 – 2 gr) on desulphurization rate was evaluated.

A summary of the conclusions are presented here:

1. No droplet swelling was observed by X-ray fluoroscopy. Instead, bubble rise in the slag as well as gas halo formation around the matte droplet was confirmed in high-temperature experiments.
2. No linear relationship was observed between droplet mass and gas evolution rate. But, a linear relationship was found between rate and the droplet surface area. These two findings suggested that gas nucleation occurred on the surface of the droplet, which was in agreement with gas halo observations by X-ray fluoroscopy.
3. Gas evolution rate measurements revealed that the desulphurization reaction proceeded quickly once the matte droplet touched the oxidizing slag. However, the rate declined substantially after a few seconds.
4. Kinetic investigations revealed that mass transfer in the slag phase as well as counter mass transfer of SO/SO_2 gases in the gas layer (halo) around the matte

droplet were the two competing controlling mechanisms. The second mechanism was activated only when the thickness of the gas halo became large enough.

5. Activation energies for the case of mass transfer control in the slag phase were determined to be in the range of 14.7-64.9 kJ/mole for different droplet sizes.
6. It was confirmed that formation of a gas halo with thickness as low as 50 micron, could prevent the reaction to proceed. In such a condition, mass transfer in the gas halo was the rate-controlling mechanism.
7. Although desulphurization reaction is exothermic, however gas evolution rate exponentially increased with increasing temperature. This is because the slag viscosity is lower at higher temperatures and therefore increasing the temperature will improve the mass transfer in the slag and thus will increase the overall reaction rate.
8. Optical microscopy observations of the quenched matte/slag samples confirmed gas halo formation around the droplet. In addition, a dome-like bubble could be seen on top of the matte droplets in the micrographs. This was in agreement with X-ray fluoroscopy observations.
9. EDS analysis of the quenched matte-slag samples revealed that Cu was formed as a result of the desulphurization reaction. In addition, there were areas of CuO in the micrographs, which were produced as oxygen from the slag dissolved in the Cu product.

Bibliography

1. Stanczak, M. CSA - Discovery Guides. A Brief History of Copper. CSA.com . 2005. 10-7-2013.

Ref Type: Online Source

2. Emsley, J. *Nature's Building Blocks: An A-Z Guide to the Elements;* Oxford University Press: Oxford, 2001.pp. 123.

3. Schlesinger, M. E.; King, M. J.; Sole, K. C.; Davenport, W. G. *Extractive Metallurgy of Copper (Fifth Edition);* Fifth Edition ed.; Elsevier: Oxford, 2011.

4. Sridhar, R.; Toguri, J. M.; Simeonov, S. Copper Losses and Thermodynamic Considerations in Copper Smelting. *Metallurgical and Materials Transactions B* **1997,** *28* (2), 191-200.

5. Sridhar, R.; Toguri, J. M.; Simeonov, S. Thermodynamic Considerations in Copper Pyrometallurgy. *JOM* **1997,** *49* (4), 48-52.

6. Alyaser, A. H.; Brimacombe, J. K. Oxidation Kinetics of Molten Copper Sulfide. *Metallurgical and Materials Transactions B* **1995,** *26* (1), 25-40.

7. Alyaser, A. H. Oxidation Kinetics f Molten Copper Sulphide. M.A.Sc. The University of British Columbia, 1993.

8. Ajersch, F.; Toguri, J. M. Oxidation Rates of Liquid Copper and Liquid Copper Sulfide. *Metallurgical Transactions* **1972,** *3* (8), 2187-2193.

9. Asaki, Z.; Ando, S.; Kondo, Y. Oxidation of Molten Copper Matte. *Metallurgical Transactions B* **1988,** *19* (1), 47-52.

10. Carrillo, F.; Hernández, R.; Martínez, J.; Roselló, A. Kinetics of the Copper Blow in the Peirce-Smith Converter. *Información Tecnológica* **2004,** *15* (5), 33-36.

11. Fukunaka, Y.; Nishikawa, K.; Sohn, H. S.; Asaki, Z. Desulfurization Kinetics of Molten Copper by Gas Bubbling. *Metallurgical Transactions B* **1991,** *22* (1), 5-11.

12. Jalkanen, H. Phenomenology of the Oxidation Kinetics of Molten Cuprous Sulphide and Copper. *Scandinavian Journal of Metallurgy* **1981,** *10*, 257-262.

13. Marin, T.; Utigard, T.; Marin, T. The Kinetics and Mechanism of Molten Copper Oxidation by Top Blowing of Oxygen. *JOM* **2005,** *57* (7), 58-62.

14. Roselló, A.; Martínez, J.; Barrios, P.; Carrillo, F. Desulfurization Rate during the Copper Blow in a Peirce–Smith Converter. *Metallurgical and Materials Transactions B* **2008,** *39* (1), 16-22.

15. Roselló, A.; Martínez, J.; Carrillo, F. A Kinetic Comparison between Laboratory and Industrial Scales in the Copper Blowing Process. *Journal of Metallurgy* **2009,** *2009*.

16. Elliott, J. F.; Mounier, M. Surface and Interfacial Tensions in Copper Matte – Slag Systems, 1200 °C. *Canadian Metallurgical Quarterly* **1982,** *21* (4), 415-428.

17. Fagerlund, K. O.; Jalkanen, H. Some Aspects on Matte Settling in Copper Smelting. Diaz, C., Landolt, C., Utigard, T., Eds.; The Minerals, Metals & Materials Society: 1999; pp 539-551.

18. Ip, S. W.; Toguri, J. M. Entrainment Behavior of Copper and Copper Matte in Copper Smelting Operations. *Metallurgical Transactions B* **1992,** *23* (3), 303-311.

19. Jakobsson, A.; Sichen, D.; Seetharaman, S.; Viswanathan, N. N. Interfacial Phenomena in Some Slag-Metal Reactions. *Metallurgical and Materials Transactions B* **2000,** *31* (5), 973-980.

20. Minto, R.; Davenport, W. G. Entrapment and Flotation of Matte in Molten Slag. *Transactions Institute of Minerals and Metals* **1972,** *81* (3), 36-42.

21. Nakamura, T.; Noguchi, F.; Ueda, Y.; Nakajyo, S. Floating Behavior of Molten Copper and Cu-Matte in Cu-slag – Study on Interfacial Phenomena in Phase Separation of Copper Smelting. *Metallurgical Review of MMIJ* **1989,** *6* (2), 98-111.

22. Sakai, T.; Ip, S. W.; Toguri, J. M. Interfacial Phenomena in the Liquid Copper-Calcium Ferrite Slag System. *Metallurgical and Materials Transactions B* **1997,** *28* (3), 401-407.

23. Rosenqvist, T. *Principles of Extractive Metallurgy;* McGraw-Hill: 1974.

24. Bale, C. W.; Toguri, J. M. Thermodynamics of the Cu-S, Fe-S and Cu-Fe-S systems. *Canadian Metallurgical Quarterly* **1976,** *15* (4), 305-318.

25. Chakrabarti, D. J.; Laughlin, D. E. The Cu-S (Copper-Sulfur) System. *Bulletin of Alloy Phase Diagrams* **1983,** *4* (3), 254-271.

26. Degterov, S. A.; Pelton, A. D. A Thermodynamic Database for Copper Smelting and Converting. *Metallurgical and Materials Transactions B* **1999,** *30* (4), 661-669.

27. Derin, B.; Reddy, R. G. Sulfur And Oxygen Partial Pressure Ratios Prediction In Copper Flash Smelting Plants Using Reddy-Blander Model. TMS: 2003; pp 625-632.

28. Elliott, J. F. Phase Relationships in the Pyrometallurgy of Copper. *Metallurgical Transactions B* **1976,** *7* (1), 17-33.

29. Jalkanen, H.; Tikkanen, M. H. Equilibrium Studies on High-Copper Mattes - 1. A Method for Equilibrating Molten Sulphide-Oxide Systems. *Scandinavian Journal of Metallurgy* **1979,** *8* (1), 34-38.

30. Jalkanen, H.; Tikkanen, M. H. Equilibrium Studies on High-Copper Mattes - 2. Sulphur-Oxygen Equilibria in the System Cu-S-O along the Liquid Immiscibility Field. *Scandinavian Journal of Metallurgy* **1979,** *8* (2), 64-66.

31. Kelley, K. K. Contributions to the Data on Theoretical Metallurgy VII. The Thermodynamic Properties of Sulfur and its Inorganic Compounds. *U. S. Bur. Mines Bull.* **1937,** (406).

32. Kellogg, H. H. Thermochemical Properties of the System Cu-S at Elevated Temperature. *Canadian Metallurgical Quarterly* **1969,** *8* (1), 3-23.

33. Larrain, J. M.; Lee, S. L.; Kellogg, H. H. Thermodynamic Properties of Copper-Sulfur Melts. *Canadian Metallurgical Quarterly* **1979,** *18* (4), 395-400.

34. Li, H.; Rankin, W. J. Thermodynamics and Phase Relations of the Fe-O-S-SiO_2 (sat) System at 1200° C and the Effect of Copper. *Metallurgical and Materials Transactions B* **1994,** *25* (1), 79-89.

35. Nagamori, M.; Rosenqvist, T. The Partial Pressure of Sulfur over Cu-S Melts at 1200°C. *Metallurgical Transactions* **1970,** *1* (1), 329-330.

36. Raghavan, V. Cu-Fe-S (Copper-Iron-Sulfur). *Journal of Phase Equilibria and Diffusion* **2004,** *25* (5), 450-454.

37. Schuhmann, R. J.; Moles, O. W. Sulphur Activities in Liquid Copper Sulphides. *Trans AIME* **1951,** (March), 235-241.

38. Sharma, R. C.; Chang, Y. A. A Thermodynamic Analysis of the Copper-Sulfur System. *Metallurgical and Materials Transactions B* **1980,** *11* (4), 575-583.

39. Shishin, D.; Hidayat, T.; Jak, E.; Decterov, S. A. Critical Assessment and Thermodynamic Modeling of the Cu-O and Cu-S-O Systems. *Calphad* **2013,** *41* (0), 160-179.

40. Ueda, S.; Yamaguchi, K.; Takeda, Y. Phase Equilibrium and Activities of Fe-S-O Melts. *Materials Transactions* **2008,** *49* (3), 572-578.

41. Yazawa, A. Thermodynamic Consideration of Copper Smelting. *Canadian Metallurgical Quarterly* **1974,** *13* (3), 443-453.

42. Krivsky, W. A.; Schuhmann, R. J. Thermodynamics of the Cu-Fe-S System at Matte Smelting Temperatures. *Trans AIME* **1957,** *209*, 981-988.

43. Schmiedl, J. Physical Chemistry of Continuous Copper Smelting. The Institute of Mining and Meallurgy: 1974; pp 127-134.

44. Crook, W. J. The Series Iron Oxides-Silica. *Journal of the American Ceramic Society* **1939,** *22* (1-12), 322-334.

45. Darken, L. S. Melting Points of Iron Oxides on Silica; Phase Equilibria in the System Fe-O-Si as a Function of Gas Composition and Temperature. *American Chemical Society Journal* **1948,** *70*, 2046-2053.

46. Goel, R. P.; Kellogg, H. H.; Rrain, J. L. Mathematical Description of the Thermodynamic Properties of the Systems Fe-O and Fe-O-SiO_2. *Metallurgical and Materials Transactions B* **1980,** *11* (1), 107-117.

47. Jahanshahi, S.; Wright, S. Redox Equilibria in Al_2O_3-CaO-FeO_x-SiO_2 and Al_2O_3-CaO-FeO_x-MgO-SiO_2 Slags. *ISIJ International* **1993,** *33* (1), 195-203.

48. Matousek, J. W. Equilibrium Oxygen Pressures of Iron Silicate Slags. *Metallurgical and Materials Transactions B* **1994,** *25* (3), 463-465.

49. Michal, E. J.; Schuhmann, R. J. Thermodynamics of Iron-Silicate Slags: Slags Saturated with Solid Silica. *Trans AIME* **1952,** *194* (July), 723-726.

50. Mills, K. The Estimation of Slag Properties. 2011.

51. Schuhmann, R. J.; Powell, R. G.; Michal, E. J. Constitution of the FeO-Fe_2O_3-SiO_2 System at Slagmaking Temperatures. *Trans AIME* **1953,** (September), 1097-1104.

52. Schuhmann, R. J.; Ensio, P. J. Thermodynamics of Iron-Silicate Slags: Slag Saturated with Gamma Iron. *Trans AIME* **1951,** (May), 401-411.

53. Timucin, M.; Morris, A. E. Phase Equilibria and Thermodynamic Studies in the System CaO-FeO-Fe_2O_3-SiO_2. *Metallurgical Transactions* **1970,** *1* (11), 3193-3201.

54. Turkdogan, E. T.; Bills, P. M. A Thermodynamic Study of FeO-Fe_2O_3-SiO_2, FeO-Fe_2O_3-P_2O_5 and FeO-Fe_2O_3-SiO_2-P_2O_5 Molten Systems. *J. Iron and Steel Inst* **1957,** *186*, 329-339.

55. Wright, S.; Zhang, L. The Influence of Fe^{3+}/Fe^{2+} Ratio on the Viscosity of Iron Silicate Slags. South African Institute of Mining and Metallurgy, Johannesburg: Cape Town, South Africa, 2004; pp 231-236.

56. Bowen, N. L.; Schairer, J. F. The System FeO-SiO_2. *American Journal of Science* **1932,** *24*, 177-213.

57. Schuhmann, R. J. Application of Gibbs-Duhem Equations to Ternary Systems. *Acta Metallurgica* **1955,** *3* (3), 219-226.

58. Mulholland, E. W.; Hazeldean, G. S. F.; Davies, M. W. Visualization of Slag Metal Reactions by X-ray Fluoroscopy: Decarburization in Basic Oxygen Steelmaking. *Journal of the Iron and Steel Institute* **1973,** (September), 632-639.

59. Fruehan, R. J. The Rate of Reduction of Iron Oxides by Carbon. *Metallurgical Transactions B* **1977,** *8* (1), 279-286.

60. Krishna Murthy, G. G.; Hasham, A.; Pal, U. B. Reduction Rates of FeO Dissolved in CaO-SiO_2-Al_2O_3-X Slags by Fe-C Droplets. *Ironmaking and Steelmaking* **1993,** *20* (3), 191-200.

61. Min, D. J.; Fruehan, R. J. Rate of Reduction of FeO in Slag by Fe-C Drops. *Metallurgical Transactions B* **1992,** *23* (1), 29-37.

62. Molloseau, C. L.; Fruehan, R. J. The Reaction Behavior of Fe-C-S Droplets in CaO-SiO_2-MgO-FeO Slags. *Metallurgical and Materials Transactions B* **2002,** *33* (3), 335-344.

63. Chen, E.; Coley, K. S. Kinetic Study of Droplet Swelling in BOF Steelmaking. *Ironmaking & Steelmaking* **2010,** *37* (7), 541-545.

64. Krishna Murthy, G. G.; Sawada, Y.; Elliott, J. F. Reduction of FeO Dissolved in CaO-SiO_2-Al_2O_3 Slags by Fe-C Droplets. *Ironmaking and Steelmaking* **1993,** *20* (3), 179-190.

65. Chen, E. Kinetic Study of Droplet. PhD McMaster University, Hamilton, 2012.

66. Gore, T.; Hazeldean, G. S. F. Basic Oxygen Steelmaking: Decarburization of Binary Fe-C Droplets and Ternary Fe-C-X Droplets in Ferruginous Slags. *Ironmaking and Steelmaking* **2013,** *8* (4), 167-181.

67. Gaye, H.; Riboud, P. V. Oxidation Kinetics of Iron Alloy Drops in Oxidizing Slags. *Metallurgical Transactions B* **1977,** *8* (2), 409-415.

68. Kozakevitch, P.; Urbain, G.; Sage, M. Stresses on The Interface Iron Slag and The Mechanism of Desulfurization. *Rev. Met.* **1955,** *52*, 61-71.

69. Baker, L. A.; Warner, N. A.; Jenkins, A. E. Kinetics of Decarburization of Liquid Iron in an Oxidizing Atmosphere Using the Levitation Technique. *Trans. AIME* **1964,** *230*, 1228-1235.

70. Patnaik, p. *Handbook of Inorganic Chemicals;* McGraw-Hill: 2002.

71. Greenwood, N. N.; Earnshaw, A. *Chemistry of the Elements;* Pergamon Press: Oxford, 1984.

72. Pomeroy, M. D. Decarburization Kinetics of Fe-C-S Droplets in Oxygen Steelmaking Slags. Masters McMaster University, Hamilton, 2011.

73. Bohlen, S. R.; Dollase, W. A.; Victor, J. W. Calibration and applications of spinel equilibria in the system FeO-Al_2O_3-SiO_2. *Journal of Petrology* **1986,** *27* (5), 1143-1156.

74. Stull, D. R.; Prophet, H. *JANAF Thermochemical Tables;* U.S Department of Commerce: Washington, DC., 1971.

75. *JANAF Thermochemical Tables, P. 13 168370 (1964) and P13 168370-1 (1965);* U.S Department of Commerce: 1964.

76. Hultgren, R. R.; Desai, P. D.; Hawkins, D. T.; Gleiser, M.; Kelley, K. K.; wagman, D. D. *Selected Values of the Thermodynamic Properties of the Elements;* American Society for Metals: Metals Park, Ohio, 1973.

77. Deo, B.; Boom, R. *Fundamentals of Steelmaking Metallurgy;* Prentice-Hall International: New York, 1993.

78. Moore, J. J. *Chemical Metallurgy;* 2nd ed.; Butterworth and Co: London, 1990.pp. 119.

79. Fuller, E. N.; Schettler, P. D.; Giddings, J. C. New Method for Prediction of Binary Gas-Phase Diffusion Coefficients. *Ind. Eng. Chem.* **1966,** *58* (5), 18-27.

80. Kaiura, G. H.; Toguri, J. M.; Marchant, G. Viscosity of Fayalite-Based Slags. *Canadian Metallurgical Quarterly* **1977,** *16* (1), 156-160.

81. Mihailova, I.; Mehandjiev, D. Characterization of Fayalite from Copper Slags. *Journal of the University of Chemical Technology and Metallurgy* **2010,** *45* (3), 317-326.

82. Graham, S. M.; Mellis, G. The Determination of Species in Slags and Other Materials. Randburg, South Africa, 2006.

83. Barnebey, O. L. The Determination of Ferrous Iron in Silicates by Titration with Dichromate. *Journal of the American Chemical Society* **1915,** *37* (8), 1829-1835.

84. Sims, C. E.; Larson, B. M. Determination of Ferrous Iron in Materials Containing Metallic Iron. *Industrial and Engineering Chemistry* **1925,** *17* (1), 86-88.

Appendix 1. Details of chemical titration analysis

The amount of iron in oxide ores, slags, sponge iron, etc. can be determined either by precipitation of hydrous ferric oxide and ignition to Fe_2O_3 or by reduction of dissolved ferric iron (Fe^{+3}) to ferrous iron (Fe^{+2}) followed by titration with a standard oxidizing agent such as dichromate ion, $Cr_2O_7^{2-}$ [82].

In this study, percentages of ferrous and ferric iron in slag samples quenched from different experimental high-temperatures were determined by chemical titration technique and adopting the primary method of standard potassium dichromate as the titrant. According to the literature [82-84], chemical titration when potassium dichromate is used as the oxidizing titrant for determination of iron is considered highly accurate and some have estimated that error of measurement in this procedure is less than 2% [82]. High accuracy of measurements in this procedure is especially reported for the case of direct reduced iron and iron-containing slags.

There is a basic philosophy in chemical titration to determine the amount of ferrous and ferric iron available in an ore or slag and that is:

Total iron = metallic iron + ferrous iron (Fe^{+2}) + ferric iron (Fe^{+3}) (1)

For the determination of total iron, stannous chloride ($SnCl_2$) solution containing some mossy tin metal and HCl is used. However, in this study, total iron is known and can be easily calculated from the amount of iron, which is charged as hematite plus pure iron in

the slag preparation step. So by knowing only two of the terms in the right-hand side of the Equation (1), the other term and then the Fe^{+2}/Fe^{+3} ratio would be known.

For simplicity and to reduce the risk associated with using hazardous materials, it was decided to measure the amount of metallic iron and ferrous iron in the slag samples. The procedures followed were different and will be explained briefly in this section. Three main solutions needed to use for titration test in order to measure the metallic and ferrous iron are potassium dichromate solution, titration mixture and copper sulfate solution.

Materials preparation steps

a) Potassium dichromate ($K_2Cr_2O_7$) solution was produced by dissolving 4.389 grams of fine powders of the salt in water and then diluting the solution to one liter.

b) Titration mixture was prepared as follows: In a liter flask, to about 300 mls. of water, 150 mls. of sulphuric acid (H_2SO_4 **,** cold), 150 mls. of phosphoric acid (H_3PO_4) and 12 mls. of a 0.3% aqueous solution (0.3 gram/100 mls.) of p-Diphenylamine sulfonic acid sodium salt 50% ($C_{12}H_{10}NNaO_3S$) was added respectively and the solution was then diluted to 1 liter.

c) Copper sulfate solution was produced by dissolving 100 mls. of pentahydrate ($CuSO_4 \cdot 5H_2O$) type of copper sulfate in about 300 mls. of water, in a liter boiling flask. Then 3-4 grams of cupric oxide (CuO) was added to the solution and the vessel was

shaken in a warm place for several hours. Then the mixture was filtered and the filtrate was diluted to 1 liter.

Procedure

The procedures followed to determine the amount of iron either in pure, ferrous or ferric form were mainly based on the methods explained in the literature using potassium dichromate as the oxidizing titration agent.

1) Metallic iron measurements

0.25 grams of fine powder obtained from the slag sample was placed in a 250 mls. beaker. 90 mls. of copper sulfate solution was added to the beaker. The beaker was covered with watch glass and was shaken at 200 °C for 2 hours until the sample was dissolved.

The mixture was then filtered through a #40 Whatman paper retaining the filtrate in a 500 mls. Berzelius beaker. The 250 mls. mixture was filtered twice and the beaker, paper as well as the residue was washed several times with distilled water. The paper and residue was reserved for Fe^{+2} measurements.

The filtrate was diluted to 300 mls. with cold distilled water and then 30 mls. of titration mixture was added to the solution. Subsequently the titration was carefully conducted using the potassium dichromate solution. Number of mls. of titrant * 2 = % metallic Fe (based on a 0.25 gram sample)

2) Ferrous iron (Fe^{+2}) measurements

The main reaction here is:

$$Cr_2O_7^{-2} + 6\ Fe^{+2} + 14H^{+} = 6Fe^{+3} + 2Cr^{+3} + 7H_2O \qquad (2)$$

The filter paper and the residue obtained from the metallic iron determination step was washed and dissolved in 50 mls. of sulphuric acid (1:4 ; one part acid in 4 part water, cold). The mixture was in a beaker and the beaker was covered with watch glass and was shaken at about 130 °C for about one hour in order to help the residue to dissolve in acid.

The mixture was then filtered through #41 paper, retaining the filtrate in 500 mls. Berzelius beaker. The mouth of the beaker was washed carefully for several times after each pour. The paper was also washed several times to increase the accuracy of the measurements. The filtrate was then diluted to 150 mls. and then 30 mls. of titration mixture was added. Subsequently the titration was carefully performed using the potassium dichromate solution as before. The solution was clear in color, but as the titration mixture was added dropwise and the beaker was smoothly shaken, there was a point at which the color permanently changed to violet. Number of mls. of titrant * 2 = % Fe^{+2} (based on a 0.25 gram sample)

As explained before, now by knowing the total Fe (from slag preparation), metallic Fe as well as ferrous Fe, the amount of ferric Fe could be calculated. The advantage of this method was that there was no need to perform the titration test for ferric Fe and total Fe measurements, in which highly hazardous materials such as mercuric chloride ($HgCl_2$)

and hydrofluoric acid (HF) were needed to be dealt with. However, in order to increase the accuracy, each measurement was performed at least three times on each slag and then the average values were considered.

Appendix 2. Error analysis

During performing the experiments and analysis, due care was taken in order to ensure that the experimental errors were minimized. However, given the inherent nature of any experimental work, a certain level of error is inevitable and the aim is to address it here briefly.

In synthesizing the fayalite slag, there might be some negligible levels of error resulted from scale as well as ball mill mixing. Some powders might stick to the vial or the balls, although the aim was to minimize it.

For the high-temperature experiments, there are different potential sources of error. To increase the accuracy of the data, pressure and temperature in the furnace were carefully calibrated (Explained in Chapter 3 in more details). However due to the structure of the furnace and the positions at which the crucible sits and where elements are located, there still might be a difference of maximum ±3 degrees between the real temperature at which the reaction is happening and the temperature that the furnace is showing.

In addition, although the furnace was carefully sealed, nevertheless careful recording of the pressure variation inside the furnace revealed that there was a negligible level of pressure decline over time. This phenomenon could potentially undermine the reliability of the data, especially in later times (periods over half an hour). However, since initial reaction rates were calculated in this study, this is not an important issue here and can be neglected. Nevertheless, no need to say that especial care was taken in all the experiments

to have a leakage-free medium (furnace). In order to ensure that and to minimize this potential error associated with any possible leaks, O-rings were changed every 2-3 experiments to have a completely sealed furnace.

Another potential source of error during performing the experiments was attributed to the matte droplet. It was found that in some experiments, a small fraction of copper sulfide droplet did not fall into the slag and was left at the end of the delivery tube. Although the weight of these fractions was carefully measured and was then deducted from the total droplet mass for the rate calculations, however this phenomenon still might be a potential cause of error.

It is to be noted that in order to test the reliability as well as the reproducibility of the pressure data obtained, at least two thirds of experiments were repeated once (some even more). In addition, an average value of the results obtained from repeated experiments was considered for the initial rate at that specific temperature and matte droplet size (mass). It should be emphasized that the results were largely reproducible and the difference between the results and the average value of the results was not significant in similar experiments.

Reaction between FeO in the slag and alumina crucible could be a potential source of error. As it was mentioned repeatedly earlier, alumina tends to react with FeO to form spinel in high temperatures employed in this study. In fact, as it could be seen in Chapter 4, EDS analysis of the slag samples showed that as high as ~ 4-5 wt% Al was present in the slag. Although EDS is semi-quantitative, however this clearly indicated that some

reaction between slag and the alumina crucible happened and in fact, erosion could be clearly seen just by looking at the slag/crucible contact area at the end of the experiments (especially those performed at 1450 and 1475 °C).

Regarding optical microscopy images of the matte/slag samples, it should be mentioned that these figures were obtained after quenching the samples, cutting the crucible and slag, polishing the matte/slag cross-sectional area and eventually capturing the micrographs using the microscope. The most difficult part in this process was cutting the crucible and reaching to the slag/matte cross-section. Because of the brittle nature of the slag, there were many instances that slag was suddenly crushed in pieces during the cutting process and consequently the whole experiment needed to be repeated. If the slag could survive the cutting process, polishing was next. Polishing was performed until cross section of the slag/matte droplet could be clearly seen. However, one source of potential visual error in optical microscopy images could be the fact that not all photos were taken from where the matte droplet was at its largest cross-sectional area. Thus, there might be some discrepancies between the sizes of the matte droplet in optical microscopy images given. This was largely unpreventable, as the exact location of the matte droplet inside the slag was not known.

Regarding EDS analysis, the most important issue that should be kept in mind is that EDS is a semi-quantities analysis and therefore the results provided in this study are merely for comparison. To obtain final EDS analysis results, first the effect of carbon deposition on the results was eliminated by giving the rough estimate of the thickness of the carbon layer to a special software. Then in order to enhance the accuracy of the results and to

make sure that the results were reproducible, point and areal elemental analysis was performed at least 3 times on each location (slag, matte droplet, product phases).

EDS values obtained for O in the quenched slag samples were higher than the theoretical values of oxygen in the slag powder mixture. As it was explained in more details in the corresponding section, this phenomenon might be attributed to some oxygen pick-up by slag during quenching process, which was not performed in inert atmosphere, as well as potential oxygen pick-up during sample preparation steps prior to EDS analysis (i. e. cutting, polishing).

Chemical titration was performed on the quenched slag samples using potassium dichromate as the titrant. The test involved repeated addition of solutions, repeated filtering as well as a titration stage. In the crucial titration stage, titration mixture was added to the clear solution dropwise, and then the solution was shaken and the process was repeated until a change in color of the solution appeared. All these steps could potentially be associated with human error. Especially the last step could become erroneous, as it required judgment and strong ability to distinguish between light colors. In order to minimize these errors and to increase the accuracy, great care was taken during all steps and the test was performed at least two times (sometimes 3 times) and an average value of the results was considered (although the results were close to one another).